An Experimental Proposal on a New Measurement of the Muon Anomalous Magnetic Moment $g-2$ and Electric Dipole Moment at J-PARC

M. Aoki,[9] P. Bakule,[11] B. Bassalleck,[8] G. Beer,[22] A. Deshpande,[17] S. Eidelman,[3]
D. E. Fields,[8] M. Finger,[5] M. Finger Jr.,[5] Y. Fujirawa,[19, 14] S. Hirota,[19, 6]
H. Iinuma,[6] M. Ikegami,[6] K. Ishida,[14] M. Iwasaki,[14, ∗] T. Kamitani,[6] Y. Kamiya,[6]
S. Komamiya,[19] K. Koseki,[6] Y. Kuno,[9] O. Luchev,[13] G. Marshall,[21] Y. Matsuda,[20]
T. Matsuzaki,[14] T. Mibe,[6] K. Midorikawa,[13] S. Mihara,[6] J. Murata,[16, 14]
W.M. Morse,[2] R. Muto,[6] K. Nagamine,[4, 12, 6] T. Naito,[6] H. Nakayama,[6] M. Naruki,[6]
H. Nishiguchi,[6] M. Nio,[15] D. Nomura,[6] H. Noumi,[10] T. Ogawa,[13] T. Ogitsu,[6]
K. Ohishi,[14] K. Oide,[6] A. Olin,[21, 22] N. Saito,[6, 19, †] N.F. Saito,[13] Y. Sakemi,[18]
K. Sasaki,[6] O. Sasaki,[6] A. Sato,[9] Y. Semeritzidis,[2] B. Shwartz,[3] K. Tanaka,[6]
N. Terunuma,[6] D. Tomono,[14] T.Toshito,[7] V. Vrba,[1] S. Wada,[13] A. Yamamoto,[6]
K. Yokoya,[6] K. Yokoyama,[14] Ma. Yoshida,[9] M. H. Yoshida,[6] and K. Yoshimura[6]

[1]*Academy of Science of Czech Republic, Institute of Physics, Na Slovance 2, CZ-18221 Prague 8, Czech Republic*
[2]*Brookhaven National Laboratory, Upton, NY 11973, USA*
[3]*Budker Institute of Nuclear Physics, 630090 Novosibirsk, Russia*
[4]*University of California, Department of Physics and Astronomy,Riverside, CA 92521-0413, USA*
[5]*Charles University, Faculty of Mathematics and Physics, V Holesovickach 2, CZ-18000 Prague 8, Czech Republic*
[6]*KEK, High Energy Accelerator Research Organization, 1-1, Oho, Tsukuba, Ibaraki, 305-0801, Japan*
[7]*National Institute of Radiological Sciences, 4-9-1,Anagawa,Inage-ku,Chiba,263-8555, Japan*
[8]*University of New Mexico, Albuquerque, New Mexico 87131, USA*
[9]*Graduate School / School of Science, Osaka University, 1-1 Machikaneyama-cho, Toyonaka, Osaka 560-0043, Japan*
[10]*Research Center for Nuclear Physics, Osaka University, 10-1 Mihogaoka, Ibaraki, Osaka 567-0047, Japan*

[11]*STFC, Rutherford Appleton Laboratory, ISIS Muon group & RIKEN-RAL Muon Facility, Building R3, UG16, Chilton,OX11 0QX,Oxfordshire,United Kingdom*
[12]*RIKEN, 2-1 Hirosawa, Wako, Saitama, 351-0198, Japan*
[13]*Advanced Research Institute, RIKEN, 2-1 Hirosawa, Wako, Saitama, 351-0198, Japan*
[14]*RIKEN Nishina Center for Accelerator Based Science,2-1 Hirosawa, Wako, Saitama, 351-0198, Japan*
[15]*Theoretical Physics Laboratory, Nishina Center, RIKEN, Wako, Japan 351-0198*
[16]*Physics Department, Rikkyo University, 3-34-1 Nishi-Ikebukuro, Toshima, Tokyo 171-8501, Japan*
[17]*State University of New York, Department of Physics and Astronomy,Stony Brook, NY 11794-3800,USA*
[18]*Cyclotron and Radioisotope Center, Tohoku University, Sendai, Miyagi 980-8578, Japan*
[19]*Physics Department, University of Tokyo, 7-3-1 Hongo, Bunkyo-ku, Tokyo, 113-0033, Japan*
[20]*Graduate School of Arts and Sciences, the University of Tokyo, 3-8-1 Komaba, Meguro-ku, Tokyo 153-8902, Japan*
[21]*TRIUMF, Vancouver, BC, V6T 2A3, Canada*
[22]*University of Victoria, Finnerty Rd., Victoria, Canada*

(Dated: December 22, 2009)

Abstract

We propose to measure the anomalous magnetic moment of the positive muon a_μ down to the level of 0.1 ppm with a novel technique utilizing an *ultra-cold muon beam* accelerated to 300 MeV/c and a 66 cm diameter precision magnetic storage ring without focusing field. The beam will be also useful in measuring the electric dipole moment with the improved sensitivity better than two orders of magnitude. The proposed measurement will provide a rigorous test of the Standard Model of particle physics as demonstrated by previous experiments. Our measurement will be complimentary to the previous measurement that achieved 0.54 ppm accuracy with the "magic" energy of 3.1 GeV in a 14 m diameter storage ring. This proposed experiment will have very different systematics from the previous experiment as well as the Fermilab proposal.

---

[*] Co-contactperson : Masahiko Iwasaki (`masa@riken.jp`)

[†] Contactperson : Naohito Saito (`naohito.saito@kek.jp`)

Contents

I. OVERVIEW

1. Muon $g - 2$ and fundamental physics

The anomalous magnetic moment of the muon is directly sensitive to the electromagnetic, strong, and weak forces and has been calculated to a precision of 0.41 parts per million from known physics, referred to as the Standard Model. Suggested extensions of the Standard Model (SM) would modify the muon $g - 2$ prediction. These include models with supersymmetry and extra gauge and Higgs interactions. In effect, the SM prediction of the muon anomalous magnetic moment represents a sum of all known physics, and a definitive disagreement between experiment and theory signals the presence of new physics beyond the SM. Likewise, the agreement between experiment and theory would strongly constrain or eliminate many possible extensions of our present theoretical understanding of the basic forces of nature.

TABLE I: Current theoretical evaluation of the muon $g - 2$ and its experimental result.

QED contribution	11 658 471.810 (0.016) $\times 10^{-10}$	Kinoshita&Nio [1]
Electro-Weak contribution	15.4 (0.2) $\times 10^{-10}$	Czarnecki et al. [3]
Hadronic contribution		
LO hadronic	689.4 (4.0) $\times 10^{-10}$	HLMNT prelim.[2]
NLO hadronic	-9.8 (0.1) $\times 10^{-10}$	HLMNT prelim. [2]
light-by-light	10.5 (2.6) $\times 10^{-10}$	Prades, de Rafael & Vainshtein [4]
Theory TOTAL	11 659 177.3 (4.8) $\times 10^{-10}$	
Experiment	11 659 208.9 (6.3) $\times 10^{-10}$	world average [5]
Exp. $-$ Theory	31.6 (7.9) $\times 10^{-10}$	4.0σ discrepancy

2. Current Status of Muon $g - 2$

The advance of the spin direction vs. momentum for the muon in the magnetic field of a storage ring is directly proportional to the anomalous magnetic moment, $a_\mu = (g-2)/2$. The present experimental value for muon $g-2$ is from the E821 experiment at BNL, which achieved a sensitivity of 0.54 parts per million [5]. This measured value, a_μ = 0.001165 92080 (54) (33), and the calculated theoretical value, a_μ = 0.00116591773

(48), disagree by more than 3 standard deviations[1]: a_μ(expt.) - a_μ(theory) = 31.6 (7.9) $\times 10^{-10}$. The E821 experiment used a 3.1 GeV muon beam stored in a 1.5 T storage ring of 14 m diameter. The muons were confined in the ring using electrostatic focusing, employing the "invention" from the previous CERN experiment of selecting the muon energy so that the focusing field does not contribute at first order to the muon spin precession in the storage ring, referred to as the "magic" energy. The measurement of $g-2$ requires two separate measurements to great precision: the muon spin precession frequency, and the magnetic field. We note that although the present significant disagreement with the Standard Model from the muon $g-2$ is from the measurement of a single experiment, E821 carried out the measurement using a "double blind" approach, keeping the measurement of the precession frequency and that of the field separate until the completion of each analysis. It is worth noting that the series of measurements from E821, for each running year, each determined using the double blind approach, agree.

3. Spin Precession Measurement

The muon produced from pion decay is naturally polarized along the momentum direction as a result of the $V-A$ weak interaction. The spin orientation, or the magnetic moment will follow its momentum direction, when it is stored in the presence of static field, $\vec{B}$ and $\vec{E}$. The anomalous magnetic moment a_μ will provide an additional precession whose precession vector $\vec{\omega}_a$ is expressed as

$$\vec{\omega}_a = -\frac{e}{m_\mu}\left[a_\mu \vec{B} - \left(a_\mu - \frac{1}{\gamma^2-1}\right)\frac{\vec{\beta}\times\vec{E}}{c}\right]. \tag{1}$$

Since $a_\mu \sim \alpha/(2\pi) \sim 0.00116$, a choice of “magic” energy, $\gamma = 29.4$ would reduce the above formula to an extremely simple form, $\vec{\omega}_a = -e/m_\mu \cdot a_\mu \vec{B}$. Therefore, precision measurement of $\vec{\omega}_a$ in the precision field $\vec{B}$ will provide precision determination of a_μ. It should be noted that the same simple formula will be obtained also by eliminating the $\vec{E}$-field in the above formula.

4. A New Experiment

We believe that it is valuable to launch a new experiment to measure this fundamental

---

[1] We present a recent evaluation by K. Hagiwara, R.Liao, A.D. Martin, D. Nomura, and T. Teubner, presented at Phipsi09 [2].

quantity with a completely new experimental technique, thus providing a completely independent measurement. Figure 1 displays the expected sensitivity of this experiment. The goal for this new experiment is to reach 0.1 parts per million sensitivity. We will discuss the value of this measurement, whether or not new physics is discovered at the newly started LHC. The discovery of supersymmetry at the LHC, for example, coupled with the muon $g-2$ measurement, provides a sensitive measurement of tanβ, the ratio of the vacuum expectation values of two Higgs doublets. We emphasize, however, that the precision measurement of a fundamental quantity like the magnetic moment of a fundamental particle has its own intrinsic value.

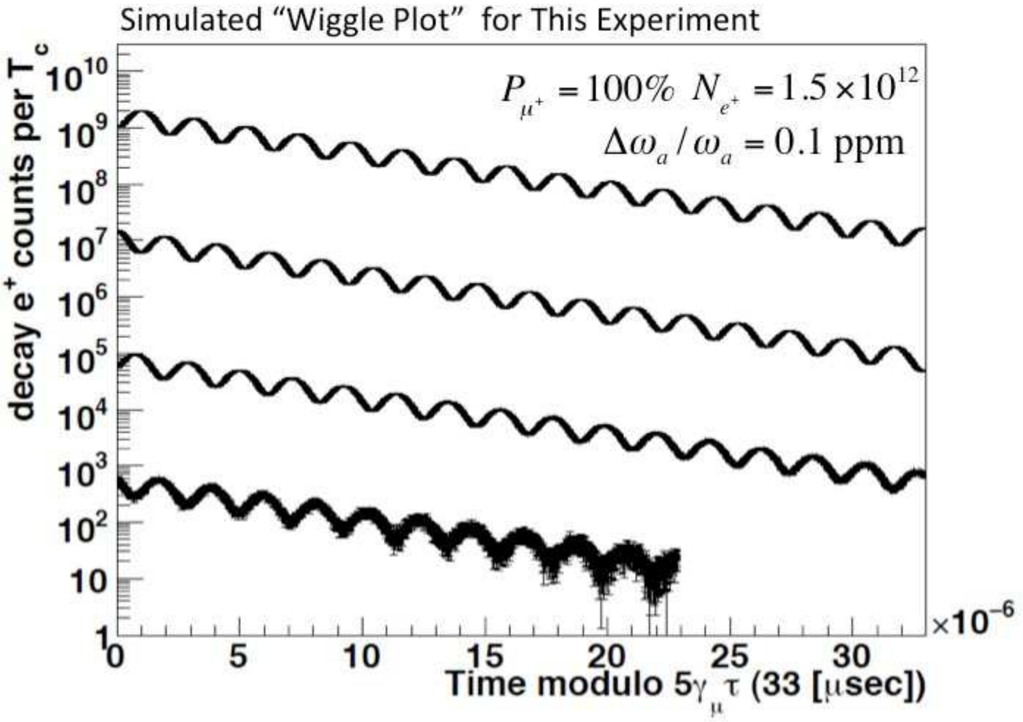

FIG. 1: Newly expected "wiggle plot" from this proposed experiment.

5. **Ultra-Cold Muon Beam and Ultra-Precision Magnetic Field**

We propose to use the very high intensity of the new J-PARC accelerator to produce, in a sequence of steps, a very cold highly polarized high intensity muon beam, at 320 MeV energy. By using ultra-cold muons, with almost no transverse dispersion, the muons can be stored for the duration of their lifetime without requiring a focusing field. Therefore, one is not forced to use the 3.1 GeV "magic" energy used by E821 at

BNL, and we have chosen an energy a factor of ten smaller. Using a 3 T magnet, the storage ring will be 66 cm in diameter, rather than the 14 m diameter of E821. There are significant advantages to use a much smaller ring, and significant disadvantages to use much lower energy. All of the experimental techniques will be different from E821. The field uniformity of the storage ring should be excellent, following technology developed for MRI magnets. We are planning a solenoid ring with spiral vertical injection of tightly bunched muons, kicked into orbit with a magnetic kicker. The cyclotron period will be 7.4 ns vs. 149 ns for E821. Positrons from muon decays will spiral in the field and be tracked using an array of radial vanes made up of silicon detectors. For E821, the positrons were detected using calorimeters. The systematic uncertainty issues for the two experiments will be very different.

6. Laser Ionization of Muonium

The cold muons will be produced by the following sequence. The J-PARC 3 GeV proton beam, running at 25 Hz, will hit the Muon graphite target in the M2 tunnel at Material and Life Science Facility (MLF), and produce pions which will be stopped in the target. Those π^+ that stop on the surface of the target decay to 4 MeV μ^+, which will be collected using a large aperture "capture" solenoid, and transported using a second solenoid, to a second target. The transported 4 MeV "surface muons" will stop in the second target, and form μ^+-electron atoms, muonium (Mu). The Mu atoms behave like hydrogen atoms and diffuse from the target. It is important that this target be at room temperature (300 K $\sim$ 25 meV) so that the Mu atoms drift slowly. Silica-aerogel is a likely candidate target to maximize the diffusion. A special new pulsed laser will ionize the muonium atoms within a few cm of the target, producing very cold, polarized, muons. A small electric field will begin the acceleration of the cold muons. The polarization of the muons from muonium is naturally 50%.

However, we plan to study the use of a magnetic field to align the Muonium spins and obtain much higher polarization. The muons are then accelerated by two linacs to reach 320 MeV.

The expected transverse dispersion of this beam is 10^{-5}. The expected cold muon intensity is 4 $\times 10^4$/pulse, in a 1 cm diameter spot.

7. R& D for the Ultra-Cold Muon Beam

The production of the very high intensity, highly polarized, ultra cold muon beam is a major challenge. Surface muon signals have already been observed from the M2 Muon target with flux that is equivalent to or better than RAL-ISIS. The room temperature muonium production target must be selected, with well-understood characteristics of the spacial distribution of the muonium atoms drifting downstream of the target. A silica-aerogel target is promising. This system is to be studied and optimized in an experiment at TRIUMF this year (proposed). The required Lyman-α laser, needed to ionize the muonium atoms, is designed and a CLBO ($CsLiB_6O_{10}$) crystal is being grown for this laser at RIKEN. This system is to be tested and optimized in an experiment at Rutherford Laboratory this year (proposed). The laser requires 100 times the power of previous lasers at this energy. The purpose of the measurements at Rutherford is to confirm the anticipated flux of ultra-cold muons, where we expect a linear gain in flux with laser power. This must be experimentally demonstrated.

We propose to use linac designs following existing linacs at J-PARC. The linacs used to accelerate the cold muons are essentially a proton-type linac at lower β using a Drift-Tube Linac (DTL), and an electron-type linac (disk-loaded type with pitch adjusted for β) at higher β.

8. Polarized Muon Source

Obtaining as high a polarization as possible is important, with the sensitivity of the measurement proportional to the square of the muon polarization.

The polarization of the surface muon is nearly 100% as it is naturally polarized from pion decay. The muon picks up an unpolarized electron at muonium protudcion target to form a muonium (hydrogen-like atom which consists of a muon and an electron). The polarization of muon is kept when the muon spin and electron spin are parallel in the muonium, while the polarization is lost when they are anti-parallel. Since the proposed laser beam can not distinguish those muonim states, the net polarization of the ultra-slow muon is 50%.

There is a possibility of further improvement in the polarization by either applying a longitudinal magnetic field of ∼0.3 T or using a narrow band laser to sweep away depolarized muons. Studies on such a possibility are necessary, and are in progress.

9. **Muon Storage**

A study of the muon trajectory for the storage solenoid and the vertical spiral injection is shown in Figure 2. An actual coil configuration is being studied in collaboration with a private company as displayed in Figure 3. An anti-Helmholz type kicker with 150 ns pulse full width (half-sine) and 1.3 Gauss is being studied to store the muons. The beam of muons will be in a 2 ns long (full width) bunch with $\Delta p/p = 10^{-3}$. At the beginning of the $g-2$ measurement, we expect to have 4 $\times 10^4$ muons, 320 MeV, 6.6 μs lifetime, with a transverse dispersion of 10^{-5}. In order to match the early and late muon decay acceptance in the detectors we are considering a very small confining quadrupole field of field index of order 10^{-5}.

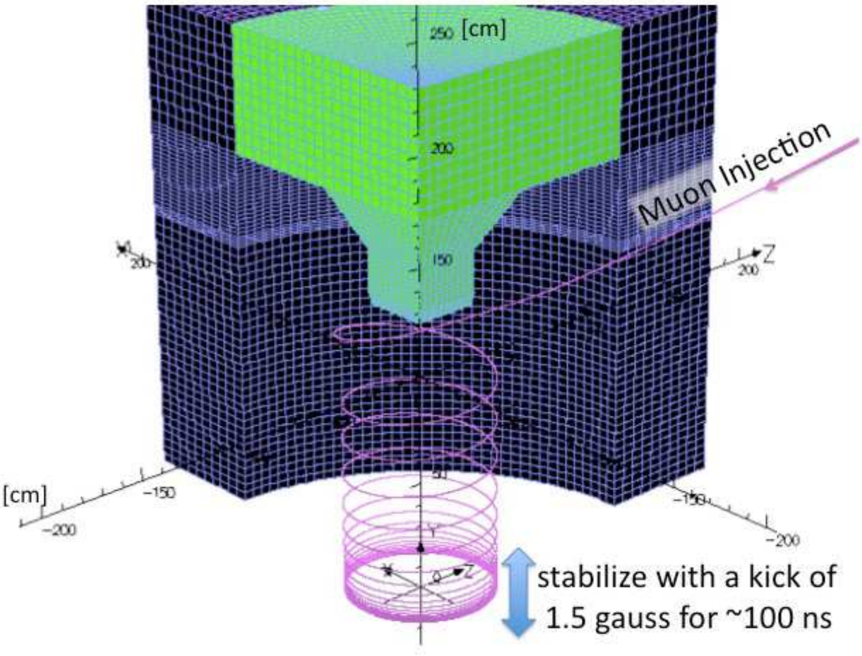

FIG. 2: Preliminary design of the muon injection into the solenoid storage ring. One eighth of the iron yoke (black and green) is displayed without coils and kickers. The injected muon trajectory is also shown.

10. **Detection of Decay Positrons**

Radial vanes of silicon detectors will track the decay positrons. A study for this detector is shown in Figure 4, which includes a positron track. Positrons will be measured over 5 muon lifetimes, 33 μs. At early time, we will have on average ~7 positron tracks per 7.4 ns turn. If we have a 50 ns detector pulse width, effectively

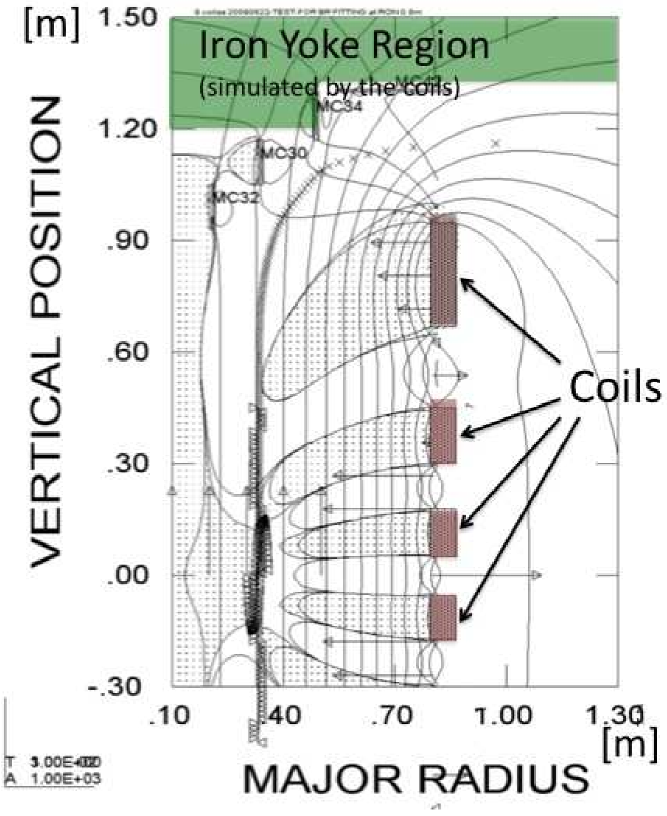

FIG. 3: One of the examples from the current field calculation studies for the muon storage solenoid is displayed. The iron yoke is not implemented in these field studies, but simulated with the coils. Details of the coil configuration for the main field is under study.

there will be ∼50 spiral tracks that should be either reconstructed or rejected as being compromised by pileup. The pileup requirements are determined by the pileup effect on early to late reconstruction differences for the energy and time of the events. The detectors and signal widths are being designed to deal with the very high rates at early times in the measurement. Our present scheme is to use 5 cm × 10 cm silicon strip detectors with 0.2 mm pitch. The 39 ms time gap between fills would be used to select hit windows in the detector data, zero-suppressing the rest. Each vane would consist of two detectors covering an area of 20 cm radially × 40 cm vertically, with two dimensions of readout. We plan 32 vanes. The total number of strips would be 96K.

11. Statistics and Required Beam Time

As mentioned above, we have chosen a lower muon energy for the storage ring for the

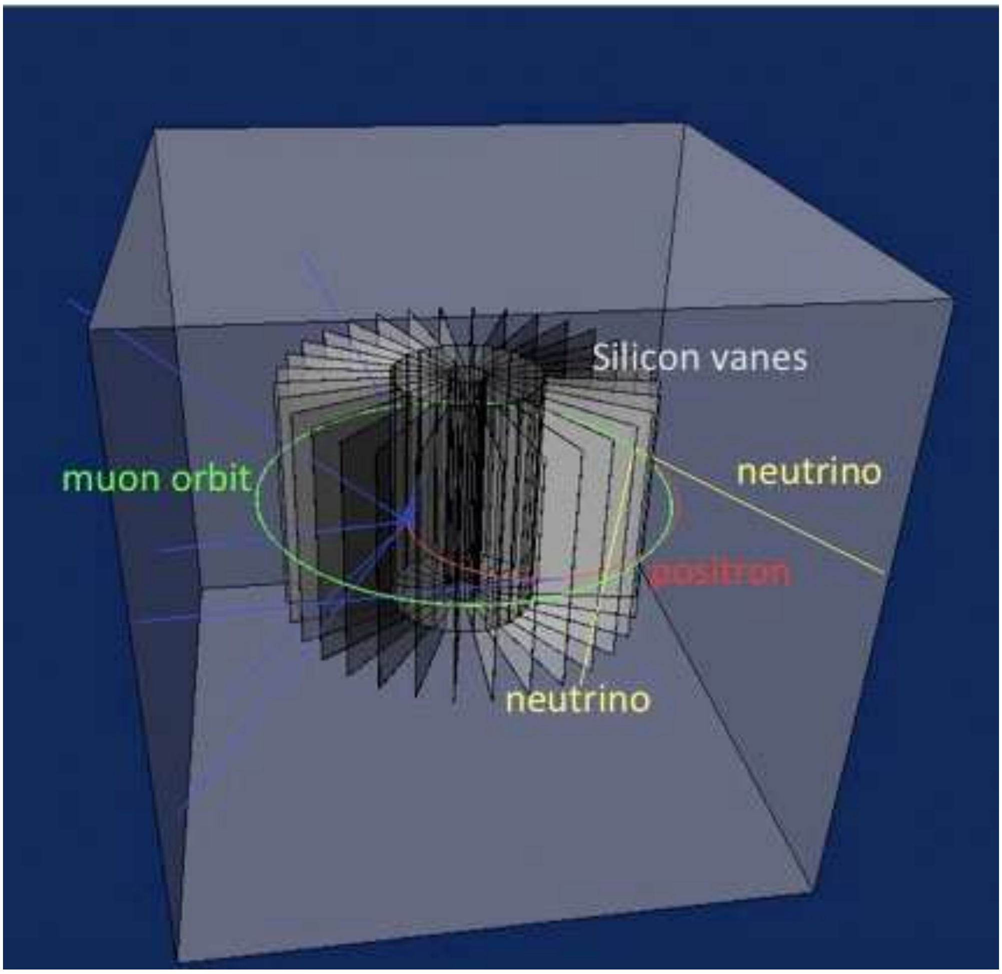

FIG. 4: A muon decay event is displayed together with the preliminary version of the detector design.

precession measurement. The statistical sensitivity of the frequency measurement is estimated as

$$\frac{\delta\omega_a}{\omega_a} \sim \frac{1}{\gamma}\frac{1}{\sqrt{N_{e^+}P_\mu^2A^2}}, \tag{2}$$

where N_{e^+}, P_μ, and A denote the number of detected positrons from muon decays, muon polarization and the analyzing power, respectively. The analyzing power would depend on the energy cut in the analysis. A 0.1 ppm measurement requires a run of $1{\times}10^7$ seconds with a surface muon flux of $4{\times}10^8\mu^+$/sec. This statistical sensitivity assumes reaching a muon polarization, P_μ of 0.9. For the minimum polarization of 0.5, the 0.1 ppm statistical sensitivity requires $4{\times}10^7$ seconds. There is no question that, particularly with completely new production and detector schemes, this measurement will require a significant learning curve. A 0.5 ppm measurement (statistical) will be a very significant initial goal, making a strong impact on the physics, since this statistical sensitivity is identical to the previous measurement, E821. This step requires 1.6×10^6 seconds (< a month) of running, for a muon polarization of 0.5.

12. **Consideration on Systematics**

    The identification, control, and measurement of the systematic uncertainties are the cruxes of the muon $g-2$ measurement. These will be quite different for this experiment, compared with E821. We introduce this discussion by reproducing the E821 systematic uncertainty tables for the spin precession and magnetic field measurements, with remarks and estimates for this experiment at J-PARC. Table II presents the uncertainties and remarks for the spin precession measurement. The estimates and remarks for this experiment are based on the current design of the experiment, which is still in an early stage. We attempt to identify the major issues, and have approaches to control and measure these systematic uncertainties.

TABLE II: Systematic uncertainties for ω_a. Details are discussed in Sec. X.

Source of uncertainty	E821-R01 (ppm)[5]	This experiment (ppm)
Pileup	0.08	<0.05(goal)
AGS background	< 0.1	0.0
Lost muons	0.09	<<0.09
Timing shifts	< 0.1	<<0.1
E-field, pitch	<0.1	<<0.1
Fitting/binning	<0.1	<<0.1
Coherent Betatron Oscillation	0.07	0.00
Gain changes	0.12	<<0.1?
Others	–	–
Total (ω_a)	0.21	0.07 (goal)

13. **Precision Measurement of the Magnetic Field**

    Table III presents the uncertainties from E821 for the magnetic field, and estimates for this experiment and remarks. The main difference for this experiment is that the small storage ring size allows construction of a single magnet structure and local non-uniformity should be at a 1 ppm level, compared a local non-uniformity at a ±50 ppm level for E821 (across the joints of the 36-sector pole structure of the 14 m diameter magnet). Even so, E821 achieved an uncertainty in the integrated field (the field that the muons saw) of 0.17 ppm. The uncertainty for J-PARC should improve on this.

TABLE III: Systematic uncertainties for B.

Source of errors	E821-R01 (ppm)[5]	This experiment (ppm)
Absolute calibration of standard probe	0.05	0.05
Calibration of trolley probes (field measurement on the muon trajectory)	0.09	<0.09
Trolley measurement B_0	0.05	<0.05
Interpolation using fixed probes	0.07	<0.07
Uncertainty from muon distribution	0.03	<0.03
Inflector fringe field uncertainty	0.00	0.00
Others	0.10	–
Total syst. error on ω_p	0.17	<0.07(goal)

14. Cost Estimate

Here we give a cost estimate. This is very preliminary without engineering designs, but we will give the basis for each number.

- **Surface muon transport**

  The surface muons produced at the production target will be transported to the experimental hall for muonium production. The first capture solenoid should be made radiation resistive. Therefore, the cost estimate is based on the current conceptual design which requires 960 m of minerally insulated coil (MIC). The super conducting curved solenoid is assumed for further transport line to maximize the transport efficiency. In addition, the area should be shielded very carefully. Detailed cost estimate requires more detailed facility design, which is the next step.

- **Laser Ionization of Mu**

The laser for this experiment is being prepared at RIKEN.

- **Muon LINAC**

  The current design assumes significant overlap in design with the existing J-PARC LINAC. This approach is expected to reduce the cost of the LINAC.

- **Ultra-precision magnet and monitor**

  The current design of the magnet resulted in the stored energy of ∼30 MJ. We are working on the reduction of the energy. A major cost driver for the magnet would be person-power to achieve the required precision. Since the magnet is the heart of the experiment, we will work out the details with the in-house experts. Consequently, the cost would be minimized.

- **Detector**

  We currently assume a silicon detector for the tracking detector for muon decays. It would be followed by the absorber/calorimeter.

TABLE IV: Preliminary estimate of the cost of this experiment.

Item	Cost (Oku-yen)
Surface Muon Transport	Facility
Ultra-Cold Muon Source	
High-power Laser System	3.0
Initial Acceleration System	0.5
Muon LINAC	15
Ultra-precision Magnet	
Solenoid	10
Field Monitor	1
Detector System	
Silicon Tracker	1.5
Readout Electronics	0.5
TOTAL	32 + Facility

15. Schedule

We intend to start the experiment in 2014. There are four major areas of activities: the ultra-cold muon source, the ultra-cold muon beam, the ultra-precision field, and the detector system. Especially the development of the muon source represents a major challenge. We plan to perform a test experiment at TRIUMF to optimize the muonium production target in 2010. In parallel, we plan a test experiment at Rutherford with a newly developed high-power laser system.

The Muon LINAC can be constructed in two years, and be commissioned together with the source.

We have started a conceptual design of the ultra-precision field employing technology developed for MRI. We expect to have an engineering drawing in a year so that construction would start in about one year. The measurement scheme with NMR probes is being developed at this time. A test of this technique at 1.5 T is planned, followed by a test in a 3 T magnet at National Institute of Radiological Science (NIRS). A reasonably long commissioning time is allocated for the magnet, since it would be one of the most time-consuming processes to shim the magnet to sub-ppm level.

The physics production run should be divided into a few phases at least; the first step would be to reach the precision of the E821, and then further improvements would follow.

16. Comparison with BNL-E821, Fermilab Proposal, and This Experiment

There is a proposal submitted to Fermilab PAC [6] to continue the measurement with the $g-2$ ring of BNL-E821. We believe such efforts should continue as well as the new efforts which we are exploring. Expected precisions and experimental parameters are summarized in Table V.

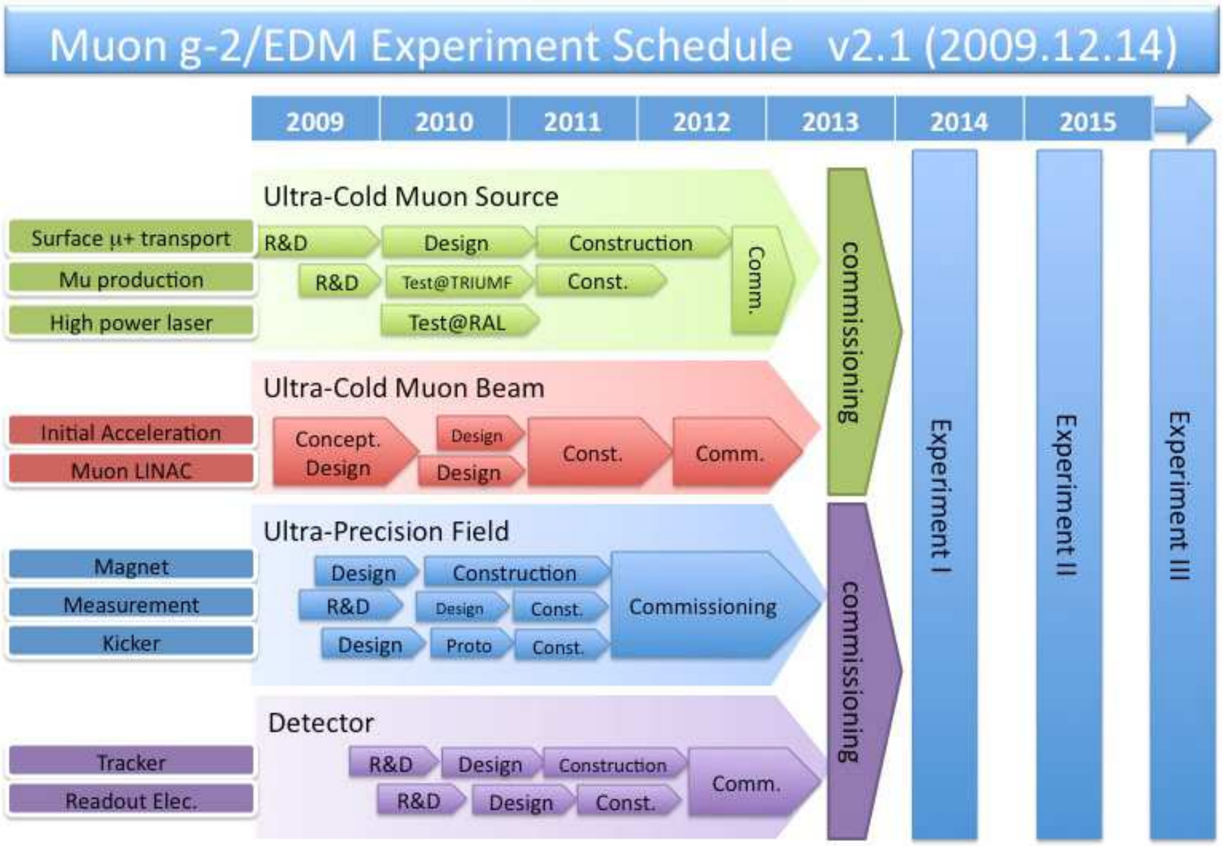

FIG. 5: Preliminary schedule of the efforts towards the experiment.

TABLE V: Comparison of the previous experiment BNL-E821, Fermilab proposal, and this experiment.

	BNL-E821	Fermilab	This Experiment
Muon momentum	3.09 GeV/c		0.3 GeV/c
γ	29.3		3
Storage field	$B = 1.45$ T		$B = 3.0$ T
Focusing field	Electric Quad.		none/very weak
# of detected e^+	5.0×10^{9}	1.8×10^{11}	1.5×10^{12}
# of detected e^-	3.6×10^{9}	–	–
Statistical precision	0.46 ppm	0.1 ppm	0.1 ppm

† † † † †

In the following sections we describe in more detail each of the above points, including some that have not been mentioned above. We are excited about the possibility of measuring such a fundamental physics observable, with a completely new approach that takes full advantage of the new J-PARC accelerator. We believe that this measurement will have lasting impacts.

We request support for the development of this challenging experiment.

II. PHYSICS OF MUON $g-2$

The anomalous magnetic moment of the muon, a_μ has been measured with ever increasing precision for more than a half-century and served as a solid testing ground for the Standard Model of particle physics. a_μ is defined from the magnetic moment $\vec{\mu_\mu}$ and its spin vector $\vec{s}$ as

$$a_\mu = \frac{g-2}{2}, \qquad \text{where} \qquad \vec{\mu_\mu} = g\frac{e\hbar}{2m_\mu}\vec{s}. \tag{3}$$

The magnetic moment is parallel to the spin, since spin is the only directionality that an elementary particle can have. The value of the magnetic moment, equivalently the anomalous part a_μ can be calculated very precisely from the standard model, including electro-weak and QCD corrections. Representative diagrams for these contributions are displayed in Fig. 6. Therefore, a precision measurement of a_μ can test the total sum of all known physics contributions directly. If any significant deviation is found, it would suggest an existence of new physics.

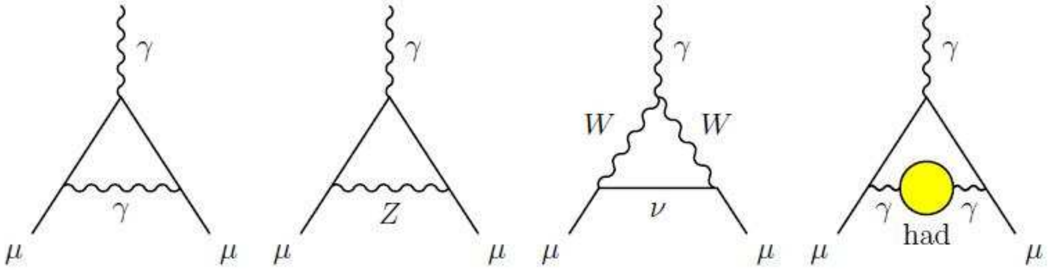

FIG. 6: Representative diagrams contributing to a_μ^{SM}. From the left to right: first order QED (Schwinger term), lowest order weak, lowest order hadronic contributions.

Differently from the electron magnetic moment, which is measured to 0.28 ppt(parts-per-trillion) and is used for the most precise determination of the fine structure constant, α, the muon magnetic moment is more sensitive to new physics thanks to its larger mass by a factor of $\sim$200. In many extensions of the SM, the sensitivity is proportional to m_l^2 so that the muon is more sensitive than an electron by a factor $(m_\mu/m_e)^2 \sim 4\times10^4$. In the case of the tau lepton, possible new physics contributions can be even larger, however, it is difficult to store in a ring to measure its magnet moment due to its short life of $\sim 3\times10^{-13}$ sec. Therefore, the muon is in a unique position to probe possible new physics contributions through precision measurements.

A. Experimental Situation

The most recent experiment to measure a_μ and d_μ, E821[5] at Brookhaven National Laboratory (BNL), has measured a_μ down to 0.54 ppm[2], and constrained d_μ down to $\leq 1.9 \times 10^{-19} \mathrm{e} \cdot \mathrm{cm}$. The obtained value has been compared to the most updated predictions of the Standard Model, and a_μ exhibits significant deviation of $\sim$4 sigma [2], while the d_μ limit is still required to be improved to be comparable to the limit from the electron with the lepton universality. Obviously further clarification is required to conclude the discovery of new physics contribution for a_μ and further improvement is required for d_μ.

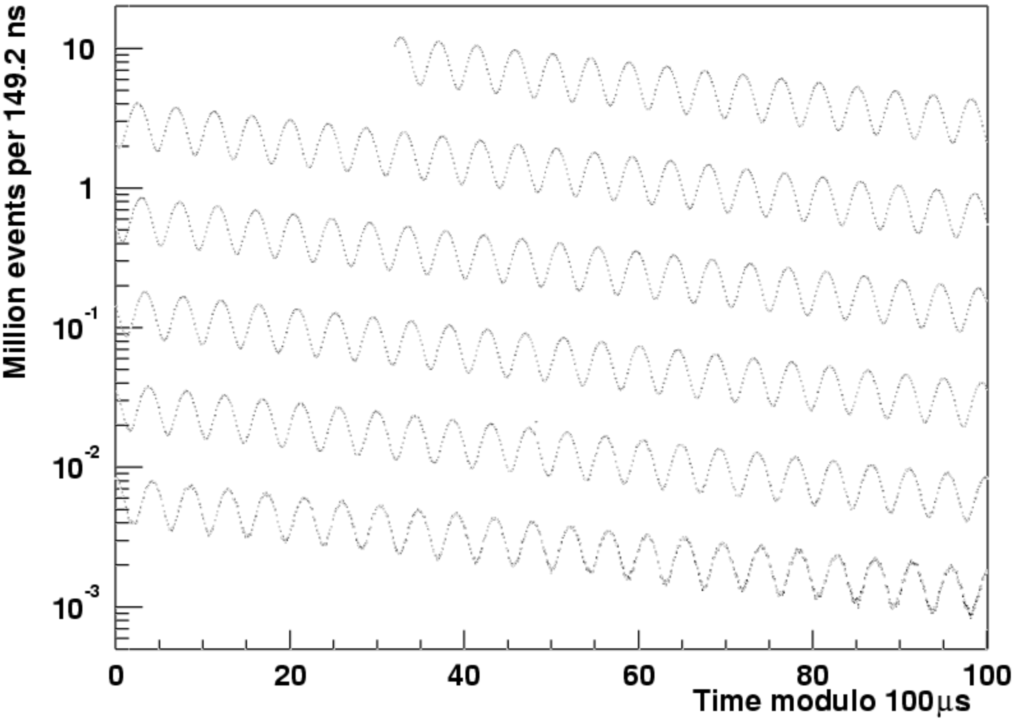

FIG. 7: "*The wiggle plot*" from the previous experiment, E821 at BNL. The figure is adopted from Ref.[5].

---

[2] The experiment measured both positive and negative muons separately to 0.70 ppm. Quoted precision of 0.54 ppm represents the combined results assuming CPT invariance.

B. Theoretical Situation

After the publication from E821, there have been many theoretical activities to investigate the implication of the possible new physics to explain the deviation. For example, a possible effect on charged lepton flavor violation (cLFV) is discussed in Ref.[10]. Furthermore, implications on the electric dipole moment are also discussed in Ref.[11]. These show that studies of flavor structure in the lepton sector is important, especially in the light of leptogenesis.

C. Principle of the $g-2$ Measurement

The anomalous part a_μ has been determined from the precession frequency $\vec{\omega}_a$ of the anomalous part of the muon magnetic-moment in the ultra-precision magnetic field, $\vec{B}$. Since the decay positron tends to be emitted in the spin polarization direction of the muon, the orientation of the magnetic moment can be determined by selecting higher energy positrons. Figure 7 clearly displays oscillation in the number of such positrons and the oscillation frequency is $|\vec{\omega}_a|$.

The $\vec{\omega}_a$ in the static magnetic field $\vec{B}$ and static electric field $\vec{E}$ is expressed as

$$\vec{\omega}_a = -\frac{e}{m_\mu}\left[a_\mu \vec{B} - \left(a_\mu - \frac{1}{\gamma^2-1}\right)\frac{\vec{\beta}\times\vec{E}}{c}\right], \tag{4}$$

and in the presence of the electric dipole moment, an additional rotation would be obtained as

$$\vec{\omega}_\eta = \frac{e}{m_\mu}\left[\frac{\eta}{2}\left(\vec{\beta}\times\vec{B} + \frac{\vec{E}}{c}\right)\right], \tag{5}$$

where η is related to $\vec{d_\mu}$ as

$$\vec{d_\mu} = \eta\frac{e\hbar}{2m_\mu}\vec{s}. \tag{6}$$

Experiment will see their vector sum, $\vec{\omega}_a + \vec{\omega}_\eta$. The Lorentz factor γ can be chosen to cancel the second term in Eq.(4) to a good precision. Previous precision measurements have been performed based on this concept namely at the magic momentum, p_{magic}.

$$a_\mu - \frac{1}{\gamma^2-1} = 0 \qquad \rightarrow \qquad \begin{cases} \gamma_{\mathrm{magic}} = 29.3 \\ p_{\mathrm{magic}} = 3.09\ \mathrm{GeV}/c \end{cases} \tag{7}$$

This choice was unavoidable in the previous measurements for following the reasons:

1. muon beam is produced from pion decays in flight and widely spread in the phase space.

2. therefore, focusing field is required to keep reasonable fraction of the beam in the storage ring.

3. the focusing has to be provided electrically; if magnetic, the precession due to a_μ would depend on each muon trajectory.

4. precision control of the electric field in addition to the magnetic field would be challenging. With an approximate cancellation of the electric field by choosing magic γ, the level of required precision would becomes accessible.

This basic concept of the experiment is so beautiful that the experiment is often referred to as a textbook measurement.

The muon beam as a tertiary beam, however, provided some complications in the previous experiment. The muon beam was contaminated by residual pions which damage the early time of the precession measurements in each injection by providing "flash" into the detector system. Since the measurement was based on the calorimetry of decay electrons/positrons, pile-ups of signals originated in "flash" was certainly not welcomed. In addition, muons cannot be fully stored in the ring basically due to its large phase space which originates in the decay kinematics and beam line acceptance. The coherent betatron oscillation of the muon beam originating in the focusing field provided additional systematics related to the muon orbits.

The previous experimental group, E821, has done their very best to reduce these systematic uncertainties. As a result, their measurement was statistically limited. There is an effort to continue this beautiful experiment at Fermilab by moving the existing muon storage ring from BNL. We believe that the proposed Fermilab experiment[6] should run to further improve the precision as a continuation of great efforts made on the experiment. However, we think it is necessary to launch a new experiment to measure this fundamental quantity with completely new techniques, and hence with different systematics.

D. New $g-2$ Experiment

We propose to measure the muon $g-2$ **without** the focusing field by employing *ultra-cold muon beam*, where the transverse momentum dispersion, $\sigma(p_T)$ is significantly smaller than its longitudinal momentum, p_L. It is easy to see that such a beam can circulate in the storage ring without the focusing field for the duration of the measurements. Elimination of the electric field would simplify the precession frequency as

$$\vec{\omega_a} + \vec{\omega_\eta} = -\frac{e}{m_\mu}\left[a_\mu \vec{B} - \frac{\eta}{2}\left(\vec{\beta}\times\vec{B}\right)\right]. \tag{8}$$

Since the rotation axes due to a_μ and d_μ are orthogonal, separation of these signals should be possible. As will be described in detail, we aim to measure a_μ down to 0.1 ppm, and search for an EDM with a sensitivity of $5\times10^{-22}\ e\cdot$cm.

Differently from the beam storage for collider experiments, where the beam has to circulate for millions of turns, muon precession measurements requires only several thousands of turns because of its short life. For example, we consider the case with

$$\frac{\sigma(p_T)}{p_L} \sim 10^{-5}, \tag{9}$$

with the $B = 3$ T and $p = 300$ MeV/c, which corresponds to $r = 33.3$ cm. Five times its dilated lifetime corresponds to travel length of 8.3 km, or about 4,000 turns. The beam spread due to the transverse momentum dispersion in Eq.(9) is 83 mm after 4,000 turns, which can be easily accommodated in the storage field.

Such an *ultra-cold* beam can be produced from an ultra-cold muon source, where cold muons are produced from the resonant laser-ionization of muonium (Mu). The kinetic energy of the Mu is $\sim$25 meV (momentum$\sim$ 2.3 keV/c), when produced at room temperature. If we could accelerate them to 300 MeV/c without further increase in the transverse momentum, the condition (9) is satisfied. Since we have no electric field, the $\vec{\beta}\times\vec{E}$ term in Eq. (4) does not exist so that any momentum can be "magic" momentum.

While higher momentum is helpful in prolonging the life of muons, lower momentum is beneficial in reducing the size of the experimental apparatus, and hence the cost of the experiment. However, the most important benefit emerges from the fact that such a small magnet for a muon precession measurement can be made in one piece enabling us to control the field very precisely. Thanks especially to the recent advances in the magneto-resonance imaging (MRI) technology, the precision monitoring and control of the magnetic field of ∼1 m diameter has reached to 1 ppm precision. This precision can be compared to a local magnetic-field precision of the previous measurement, ∼100 ppm while the field precision integrated over full azimuth was better than 1 ppm[5].

As will be described later, the statistical precision of the measurements would depend on the γ factor as

$$\frac{\delta\omega}{\omega} \propto \frac{1}{\gamma}. \tag{10}$$

The lower value of γ has to be compensated by larger statistical samples, which we expect from the high beam power (∼1 MW) envisioned at J-PARC.

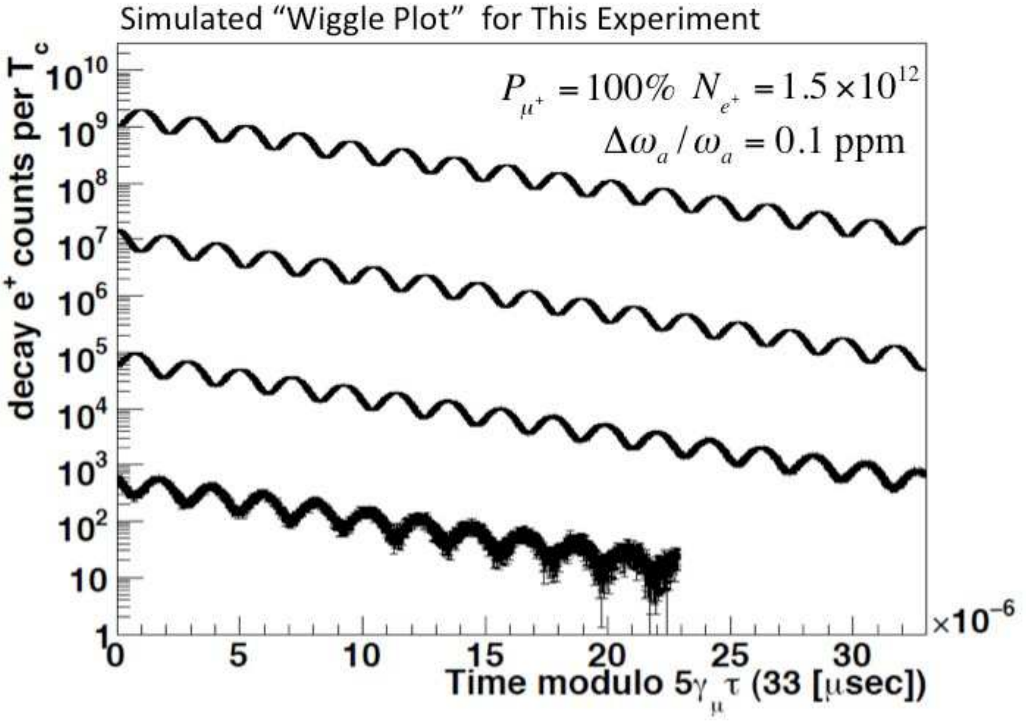

FIG. 8: Newly expected "wiggle plot" from this proposed experiment.

E. The Standard Model Prediction and the hadronic term

We briefly describe the current status of the standard model prediction. Especially we discuss the hadronic term evaluation, which represents the largest uncertainty in the prediction.

One of the largest contributions to $a_\mu^{\rm had,LO}$ comes from the 2π final state (about 73%) making high-precision measurements of the corresponding cross section mandatory. CMD-2 reported their results on the pion form factor F_π from 370 to 1380 MeV [18] with a systematic error of 0.6-0.8% below 1 GeV, while SND measured F_π from 390 to 970 MeV with a systematic error of 1.3% [19]. KLOE studied F_π using the method of radiative return or ISR [20, 21] at $590 < \sqrt{s} < 970$ MeV with a sample of $3 \cdot 10^6$ events and systematic error of 0.9% [22]. The $|F_\pi|$ values from CMD-2 and SND are in good agreement. The KLOE data are basically consistent with them with a somewhat different energy dependence. The contributions to a_μ from all three experiments agree. First results on the 2π from BaBar show a slightly larger cross section [23].

Below 1.4 GeV practically all final states have been measured with consistent results by the CMD-2 and SND groups in Novosibirsk [24]. Above 1 GeV, various final states with more than two hadrons were studied by BaBar [25] using the ISR method. They measure for the first time cross sections of a few new channels and also show that some of the previous results should be reconsidered.

The results of the $a_\mu^{\rm had,LO}$ evaluation based on Ref. [2] are presented in Table II E for different energy ranges.

TABLE VI: Updated $a_\mu^{\rm had,LO}$ according to Ref. [2].

$\sqrt{s}$, GeV	$a_\mu^{\rm had,LO}, 10^{-10}$
$m_\pi - 1.43$	603.8 ± 3.1
$1.43 - 2.0$	34.1 ± 1.5
$2.0 - 11.1$	41.4 ± 0.9
$J/\psi, \psi'$	7.9 ± 0.2
$\Upsilon(1S - 6S)$	0.1 ± 0.0
$11.1 - \infty$	2.1 ± 0.0
Total	$689.4 \pm 3.6_{\rm exp} \pm 1.8_{\rm rad}$

It can be seen that due to a higher accuracy of e^+e^- data the uncertainty of $a_\mu^{\rm had,LO}$ is now much smaller than before [12, 17].

The most recent estimate of the next-to-leading order (NLO) hadronic term in [2] gives $a_\mu^{\rm had,NLO} = (-9.8 \pm 0.1) \cdot 10^{-10}$. The light-by-light hadronic contribution is estimated only theoretically [27]. Various predictions range between 80 and 136 (in units of $\cdot 10^{-11}$) with an uncertainty reaching $40 \cdot 10^{-11}$.

Using for the light-by-light term the result $(10.5 \pm 2.6) \cdot 10^{-10}$ [4] and adding all hadronic contributions, we obtain $a_\mu^{\rm had} = (690.1 \pm 4.8) \cdot 10^{-10}$. This result agrees with other estimations, e.g.,[32] and its accuracy benefits from the new e^+e^-data. Adding all theoretical contributions we obtain $a_\mu^{\rm th} = (11659177.3 \pm 4.8) \cdot 10^{-10}$, i.e. 4.0σ below the experimental value [2]. Similar deviation is reported by Ref. [32].

How real is a very high accuracy of the leading-order hadronic contribution obtained above? To a large extent it depends on our understanding of the radiative corrections due to initial-state radiation and vacuum polarization, and even more important effects of final state radiation. There is also a question of double counting of the hadronic final states in the leading- and higher-order hadronic terms [29], that of the missing states (e.g., final states with neutral particles only).

There is still no explanation for the observed discrepancy between the predictions based on τ lepton and e^+e^-data [17]. The new high-statistics measurement of the two-pion spectral function by Belle [30] leads to about the same $a_\mu^{\rm had,LO}$ as before despite some inconsistencies between Belle and ALEPH. On the other hand, a recent comprehensive analysis of the e^+e^-data below 1 GeV and those on the 2π decay of the τ lepton performed in Ref. [31] shows that the two data sets can be reconciled if mixing between the ρ, ω, ϕ mesons is taken into account in a consistent way. A recent reevaluation of isospin-breaking effects in [32] somewhat decreases the discrepancy, see Fig. 9. According to it, the difference between the τ and e^+e^--based estimates is $(6.8 \pm 3.4_{\tau+IB} \pm 2.9_{ee}) \cdot 10^{-10}$ or 1.5σ only.

Finally, the authors of Ref. [33] performed a reestimation of $a_\mu^{\rm had}$ after BaBar's $\pi\pi$ data and increase of $a_\mu^{\rm exp}$ by $+0.9 \cdot 10^{-10}$ (CODATA changed μ_μ/μ_p). The new difference between the experimental value and the theoretical prediction becomes $(24.6 \pm 8.0) \cdot 10^{-10}$ or 3.1σ, see Fig. 9.

What is the future of this study? It is clear that it will be extremely difficult to improve significantly the existing accuracy of $a_\mu^{\rm had,LO}$ by measuring the cross section of e^+e^-annihilation to better than 0.3% as required by future determinations of a_μ mentioned above. One can optimistically expect substantial progress from new high-statistics ISR

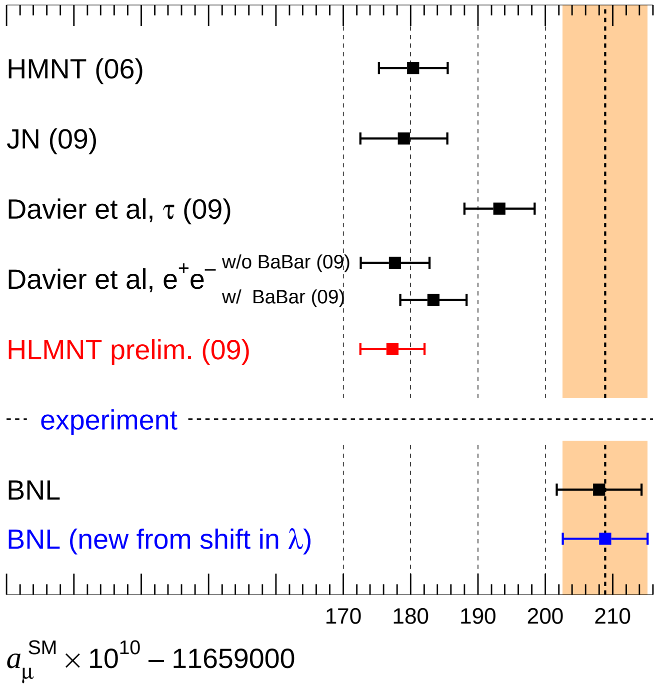

FIG. 9: Comparison of a_μ from theory and experiment [2].

measurements at KLOE, BaBar and Belle together with the more precise determination of R below 4-5 GeV from CLEO-c and BES-III. Experiments will start soon at VEPP-2000 now commissioning, which is a VEPP-2M upgrade up to $\sqrt{s}$=2 GeV with $L_{\max} = 10^{32}$ cm^{-2}s^{-1} [34]. We can estimate that by 2012 the accuracy of $a_\mu^{\mathrm{had,LO}}$ will be improved from $4.0 \cdot 10^{-10}$ by a factor of about 2 and the total error of $3.3 \cdot 10^{-10}$ will be limited by the LBL term $(2.6 \cdot 10^{-10})$.

Let us hope that progress of theory will allow a calculation of a_μ^{had} from first principles (QCD, Lattice). One can mention here a new approach in the QCD instanton model [35] or calculations on the lattice [36].

In conclusion, it should be emphasized once again that BNL success stimulated significant progress of e^+e^- experiments and related theory. Improvement of e^+e^- data led to substantial decrease of the $a_\mu^{\mathrm{had,LO}}$ uncertainty. For the first time the accuracy of the theoretical prediction is better than that of the experimental measurement. Future experiments as well as development of theory should clarify whether the observed difference between a_μ^{exp} and

$a_\mu^{\rm th}$ is real and what consequences for the Standard Model and for possible New Physics [37] it implies.

F. Muon $g-2$ in the LHC Era

In the end of this section, we briefly mention the importance of this experiment in the LHC and post-LHC era. One could argue that most of the new physics scenarios can be studied at LHC. Indeed, the most popular interpretation of the deviation from the Standard Model observed by the previous experiment is supersymmetry, and it can be studied very well at LHC, if the energy scale turns out to be appropriate. However, important parameters in the model such as μ and tanβ cannot be determined very well. The muon anomalous magnetic moment a_μ is sensitive to these parameters through following expression;

$$a_\mu(\mathrm{SUSY}) \approx (\mathrm{sgn}\mu)\ 13 \times 10^{-10} \tan\beta (\frac{100\mathrm{GeV}}{\tilde{\mathrm{m}}})^2. \tag{11}$$

The sensitivity to tanβ is compared to that of LHC experiments in Fig. 10.

However, we emphasize that it represents only one of the possible strengths of this measurement. The precision measurement of the fundamental quantities like magnetic and electric dipole moments of elementary particles has its own value.

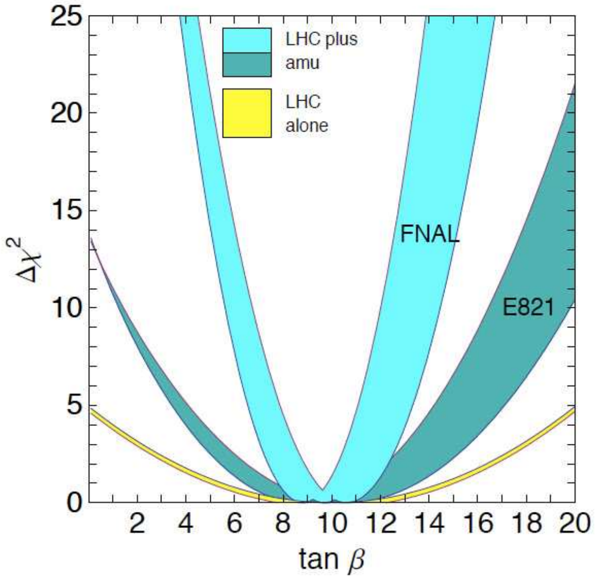

FIG. 10: Possible future tanβ determination from the measurement of a_μ, assuming that the MSSM reference point SPS1a is realized [6, 9]. The yellow band is from LHC alone which gives tan$\beta^{\rm LHC-fit} = 10.0 \pm 4.5$ [7, 8]. The darker blue band labelled E821 assumes $\Delta a_\mu = (295 \pm 81) \times 10^{-11}$, which comes from the present values for a_μ and the Standard-Model contribution, the lighter blue band labelled FNAL corresponds to $\Delta a_\mu = 295(34) \times 10^{-11}$, which has similar sensitivity projection to the proposed experiment at J-PARC.

III. SURFACE MUON PRODUCTION AND TRANSPORT

A. Proton beam from RCS

The J-PARC has been constructed in the south part of the Tokai-JAEA (Japan Atomic Energy Agency) site, and consists of a 181 MeV LINAC (400 MeV in future), as well as 3 GeV and 50 GeV proton synchrotron rings. About 90% of the 3 GeV, 333 μA (1.0 MW) beam is sent to the Materials and Life Science facility (MLF) for the production of intense pulsed neutron and muon beams, while the remaining 10% will be sent to the 50 GeV ring for further acceleration for the kaon and neutrino physics programs [38] The 3 GeV proton beam is transported through the beam transport line (the 3NBT line) over a distance of about 300 m and focused onto the 24 mm diameter muon target with a spot size that is as small as possible. The parameters of the 3 GeV proton beam are:

1. the number of protons will be 8.3×10^{13} / pulse,
2. the average beam power will be 0.6 MW, while the LINAC energy is runing at 181 MeV, and will reach 1 MW in the future when the LINAC energy is increased up to 400 MeV (expected in 2014),
3. the repetition rate is 25 Hz, so that each pulse is separated by 40 ms. One proton pulse consists of two bunches; each with a bunchwidth $\sim$ 100–120 ns, and separated by 600 ns, and
4. the transverse emittance (ϵ) will be 81π mm mrad (beam core) and 324π mm mrad (maximum halo).

B. Muon Target and Surface Muon Production

The MLF consists of the neutron and the muon science facilities which utilizes the 3 GeV, 1 MW, 25 Hz proton beam. In order to reduce the total cost of the project through common use of the utilities, getting rid of the severe beam dump construction associated with high-level tritium water handling, and by sharing the beam with the neutron facility, a tandem-target muon facility was adopted, rather than construct a separate building with our own proton (1 MW) beam dump, as was the case in KEK-MSL.

Through discussion with the neutron science group, the total beam loss induced by inserting the muon production targets is designed to be no more than 10%, which allows MUSE to install 10 mm and 20 mm thick graphite targets on the beamline upstream of the neutron target, corresponding to a beam loss of 3.5% and 6.5%, respectively. Detailed calculations on heat, radiation and duct-streaming in the vicinity of the muon target were performed by NMTC/JAM and MCNP Monte-Carlo codes [40]. In the case of the 20 mm thick graphite target, as much as 3.5 kW is deposited into a 25 mm diameter region of the target through irradiation of the 3 GeV, 1 MW proton beam.

One possible candidate for the muon production target is a rotating carbon target, which has been developed at PSI and has been working well for more than ten years [39]. In the end, an edge-cooled non-rotating graphite target was adopted, because of its ease of handling during maintenance. In this target, graphite is indirectly cooled by the copper frame, which surrounds the graphite. For the graphite material, the isotropic graphite, IG-43 was chosen, which has a thermal conductivity of 139 W/mK, 1.82 g/cm^2 density at 300 K, thermal expansion of 4.8 ppm/K, Young's modulus of 10.8 GPa, and Poisson's ratio of 0.28. In the copper frame, three turns of cooling pipe, a SUS tube with O.D. 12.7 mm and I.D. 10.7 mm, are embedded through HIP (Hot Isostatic Press). In order to reduce stress, a titanium buffer layer of 2 mm is placed between the graphite disk and the copper frame. The copper frame, the 20 mm thick graphite, and the titanium buffer layer are bonded by silver brazing in vacuum.

Calculations of the heat and stress induced by the heat deposit of the 3.5 kW beam through ANSYS demonstrate that the edge-cooled graphite target can be used safely as the 1 MW muon production target. Detailed calculations of the neutron irradiation effect on the thermal conductivity and the thermal stress induced by the proton beam will be reported elsewhere [41].

One graphite target was installed, from which four sets of the secondary lines are extracted and extended into two experimental halls (toward the west wing, one decay-surface muon channel and the super omega channel, and towards the east wing one surface muon channel and possibly one $g-2$ dedicated muon channel).

Muons (μ^+/μ^-), together with neutrinos, are a decay product of pions (π^+/π^-). Through the pp or pn nuclear reactions between the 3 GeV proton beam and the 20 mm thick graphite target, π^+ and π^-) are generated. Experimentally, two kinds of muon beams are produced and delivered to experiments; one is the Decay muon beam, and the other is the Surface Muon beam. Decay muons are obtained from π^+/π^- decaying in-flight in a long superconducting solenoid magnet. Its energy is rather higher at up to $\sim$165 MeV (250 MeV/c). On the other hand, surface muons are obtained when π^+ decay after stopping at the surface of the production target. Therefore they have a lower kinetic energy of around 4 MeV (30 MeV/c), and only positive muons are available.

C. Surface Muon Yield at J-PARC

A surface muon beam is produced when positive pions are stopped near the surface inside the production target and decay to muons. The surface muon intensity can be estimated from the number of pions stopped near the surface. Calculation was done utilizing the measured data of pion production cross section and tracking of pions with GEANT 3.21.

In order to reduce the CPU time, instead of starting from the proton beam, we generated the pions according to an empirical differential cross section equation (generator) which approximates the data taken for the 2.9 GeV proton on a beryllium target [42]. The generator equation was also compared with the recent pion production cross section data taken by HARP collaboration at CERN [43] in Fig. 11 and it was confirmed that the generator reproduces the HARP data reasonably well within 20% for low energy regions below 100 MeV. We are concerned mostly with pions with energy below 50 MeV, since the range of a 50 MeV pion is 10 g/cm^2 (4.5 cm) in graphite. Higher energy pions are less likely to be stopped in the target and would have only a small contribution to surface muon production. Even so, pions up to 500 MeV were handled for completeness.

We assumed that the pion is produced uniformly along the proton beam path in the target, since the proton interaction length is much larger than the target thickness. We also assumed the proton beam distribution is uniform inside the 24 mm diameter in the production target.

By integrating the generator equation for various angles and for pion energy up to 500 MeV, the total cross section for the positive pion production is about 90 mb. It is calculated from this cross section that the total yield of positive pions is about 0.010 per 3 GeV proton passing through the 2 cm (4.5 g/cm^2) thick graphite target. This number is converted to 2.0 x 10^{13} positive pions generated for the 333 μA proton intensity at J-PARC.

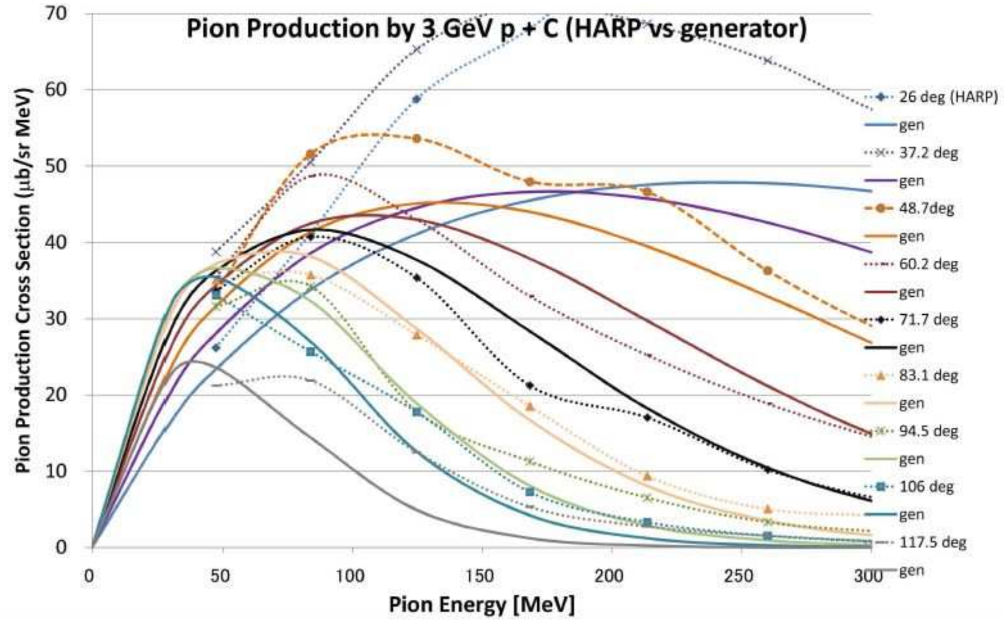

FIG. 11: Comparison of pion production differential cross section used in the pion generator (solid line) and that of HARP data (symbols and dotted lines).

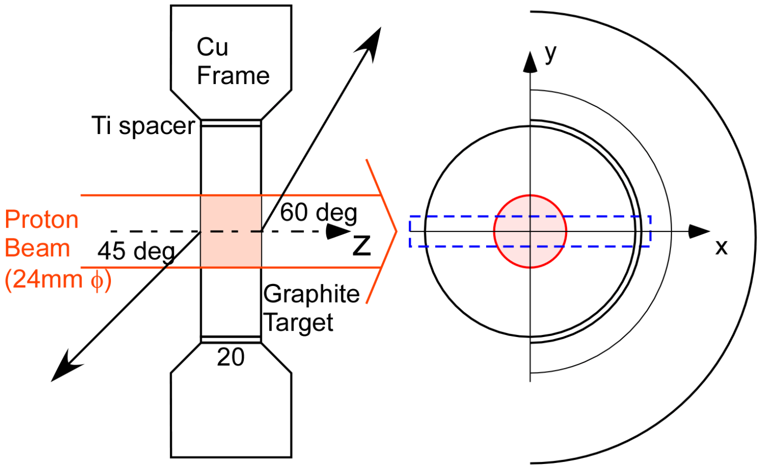

FIG. 12: Target geometry and proton beam size used for the calculation.

About 2 x 10^7pions ($1/10^6$ of the above number) were generated in the simulation to study how many of those pions are stopped near the target surface. The energy and angle of each pion was generated following the distribution of our pion generator as described above. The tracking of the pions, pion interaction in the target, their decay to muons, and the tracking of muons were handled by GEANT 3.21.

Only pions that stopped inside the production target near the surface will contribute to the generation of surface muons, so the number and depth distribution of the stopping pions is the basic information. Figure 13 shows the number of π^+ stopped in each depth region of 0.1 mm steps in units of Million/sec. The area is limited to inside 24 mm radius. For example it can be seen that 11,000 M π^+ are stopped within 0.2 mm (2 bins in the figure) from the backward surface. The number of pions stopping in the forward surface is 9,500 M and is about 15% smaller. The figure also shows that the number of pions stopping near the surface is about half (although not exactly) of those in the middle plane. This is because stops in the middle have contributions from pions produced in closeby forward and backward regions, while those stopping at the forward (backward) end are caused by pions that were produced toward the downstream (upstream) only.

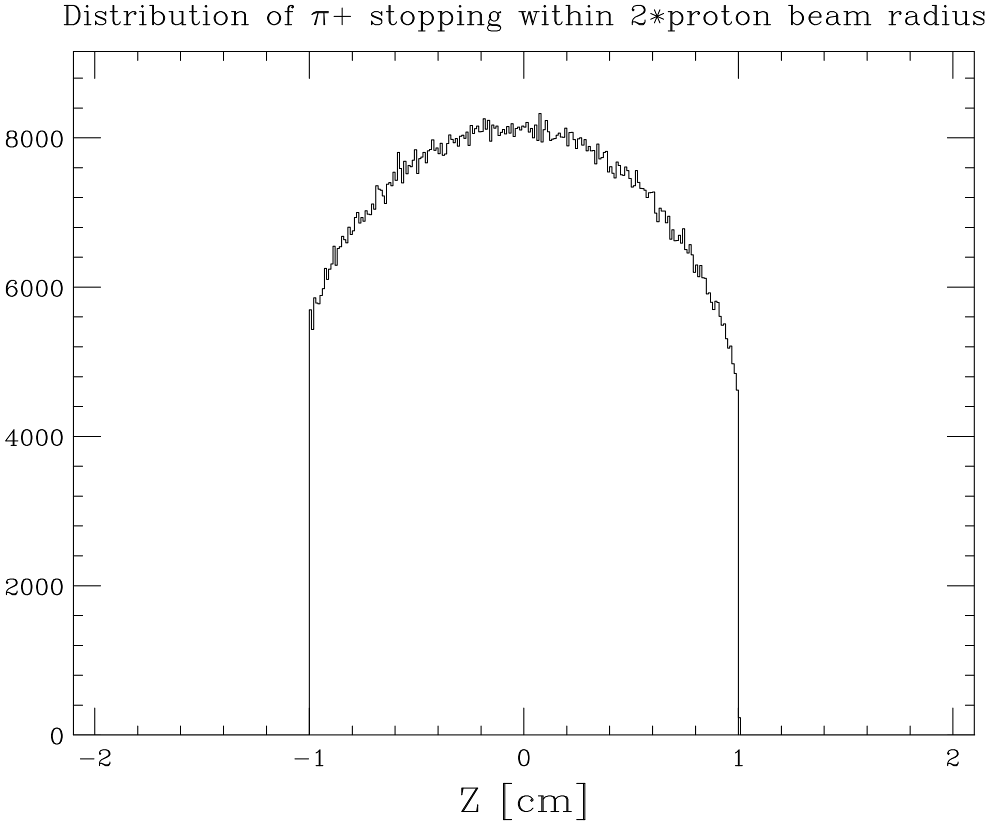

FIG. 13: π^+ stopping distribution in the production target along the beam path. Only pions that are stopping inside 24 mm radius around the center are included. Units for number of π^+ are M/s.

Figure 14 shows the horizontal distribution in the target. It is seen that the main contributions are from inside the 24 mm diameter region which is directly hit by the proton beam. There are also pions stopping outside, which amounts to 40% of those inside.

The stopped pions decay to muons, some of which are emitted into the vacuum region

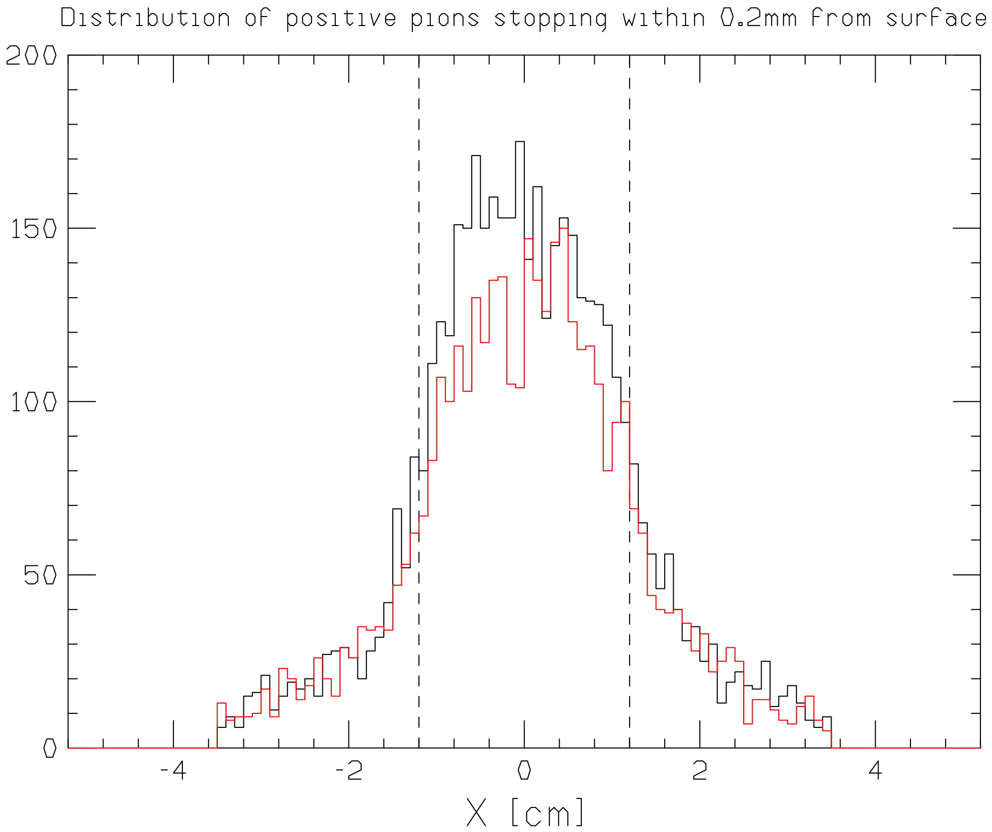

FIG. 14: Horizontal distribution of pions stopping in the production target. Only pions stopped within 0.2 mm from the backward surface (black) or the forward surface (red) and within ±5 mm vertically from the center level are plotted (see the dashed square in Fig. 12). The model is symmetric around the proton beam axis, so a similar distribution is expected for the vertical direction.

if they are within 1 mm of the target surface. The muon energy when it exits the target is lower as the pions decay deeper inside. Concerning the pions that stopped within 0.2 mm from the surface, if the muon is emitted in the direction normal to the target surface, its momentum when it exits the target ranges from 27.3 MeV/c to 29.8 MeV/c. The number of expected surface muons is calculated from the solid angle and momentum acceptance of the beamline. We should take into account that the actual beam line sees the production target surface at an angle. The effective depth contributing to the surface muon production shrinks by the cosine of the emission angle, namely by 0.71 and 0.50 for muon beamlines seeing the target at 45 degrees and at 60 degrees, respectively. The suggested $g-2$ beamline is at 60 degrees backword from the proton beam direction.

TABLE VII: Comparison of the expected muon beam intensity for three surface muon beamlines

Beamline	D-line	SuperOmega	H-2 line
Extraction Angle (degrees)	forward 60	backward 45	forward 60
Pion stops per mm thickness (10^6/s)	47,500	55,000	47,500
Solid Angle (msr)	45	400	130
Momentum Acceptance (MeV/c)	27.5-30	25-30	25-30
Maximum depth for usable pion (mm)	0.2 cos(60 degrees)	0.4 cos(45 degrees)	0.4 cos(60 degrees)
Expected Surface Muon Rate (10^6/s)	17	390	100

Let's compare the estimated production rate with the measured surface muon rate recently measured at the MLF Muon D-line, which sees the production target at 60 degrees backward from the proton beam. The design value of the D-line solid angle is 45 msr and the momentum acceptance is around 10 % FWHM. The momentum acceptance corresponds to covering the surface muons made from pions that are stopped within 0.2 mm from the surface. The fact that the beamline sees the production target at 60 degrees reduces the available thickness to 0.1 mm. Thus we expect from our pion production simulation that the surface muon beam rate will be 9,500 M/s $\times$ (0.1/0.2) $\times$ ($0.045/4\pi$) = 17 M/s, A recent measurement has observed the surface muon rate to be around 15 M/s (the measured rate is normalized to 1 MW proton intensity). Thus it is reasonable to use the above simulation result for estimating the surface muon intensity at a new channel.

The surface muon intensities for other beamlines are estimated from the simulation in a similar way. We compare the expected number of surface muons for three beamlines in Table VII. Here, we note that we expect the surface intensity of 10^8/s at the H-2 beamline.

D. Capture solenoid and muon transport

The strategy of transporting surface muons to the muonium production target through the H-2 beam line is very similar to that of the super omega beam line. Figure 15 shows the schematic picture of the H-2 beam line. Firstly, the produced surface muons are captured by the solenoids called "capture solenoids". Then they are transported along the H-2 tunnel by the super conducting transport solenoids, and finally focused on the muonium production target.

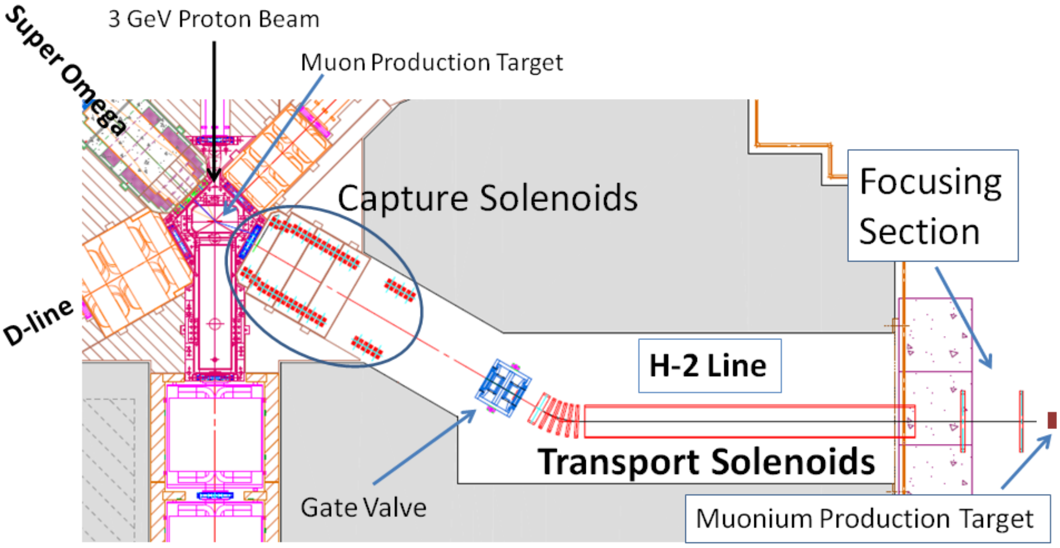

FIG. 15: Schematic picture of the H-2 beam line.

The capture solenoids in the current design consist of three types of normal conducting solenoids. The schematic view of the capture solenoids is shown in Fig. 16. The solid angle acceptance of the capture solenoids is 130 msr, which is determined by the ϕ250 mm pillow seal for the beam port located at 555 mm distance from the production target. The capture solenoids are located very close to the production target and must have high radiation resistance, thus they are made of mineral insulation cables (MIC).

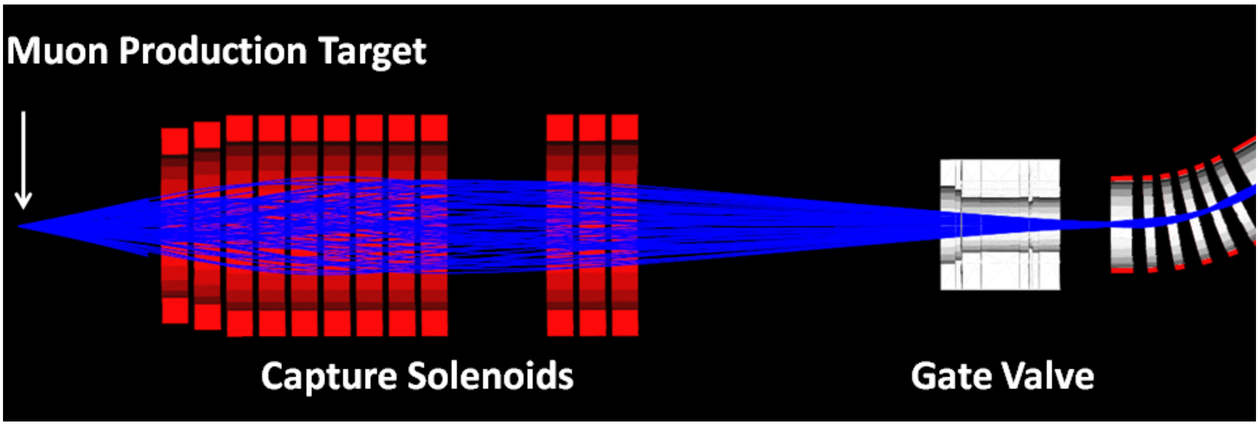

FIG. 16: Schematic picture of the capture solenoids. The blue lines represent trajectories of 30 MeV/c muons.

The transport solenoids consist of a 30° 5-segment curved section and a 4.5-m-long straight section. The diameter of the transport solenoids is 400 mm. The typical strength of the magnetic field is around 1 T at the center of the solenoids. In the middle of the transport solenoids the dipole fields in both horizontal and vertical directions will be implemented to align the beam position on the center of the downstream focusing coils.

Between the capture solenoids and the transport solenoids a gate-valve pillowseal is placed, which enables us to detach the transport solenoid for maintenance without spoiling the vacuum upstream. We propose to use a ϕ250 mm gate valve, and in that case about 10% of the muons will be lost at the gate valve. The total transport rate of the capture and transport solenoids for the 30 MeV/c surface muons is around 80% including the focusing section.

The transported muons have to be focused on the muonium production target. We are considering using two large superconducting coils. The inner diameter of the coils is 740 mm, and the interval between the two coils is 800 mm. Achieved beam size in the current design is $\sigma_x \simeq \sigma_y \simeq 15$ mm as shown in Fig. 17. We are now optimizing the design of the focusing section considering following points.

1. Making the beam size smaller is important to maximize the number of muoniums in a region for the laser ionization.

2. The focus length in the current design is 300 mm. It is too short if we have to place the vacuum disconnecting device between the focus coil and the muonium production target.

3. Some magnetic field is present at the muonium production target. If this creates a problem, we will place a field-canceling coil.

The Super Omega beam line in the muon facility plans to use the similar configuration of the surface-muon transport which consists of capture solenoids and transport curved-solenoids. The capture solenoids have already been constructed and installed in the target area. The tests of the transport solenoids have been in progress. There is a synergy in development of the beam line components and optics design since the beam line configuration is similar to that of the proposed experiment. Therefore, time and cost for the R&D for the beam transport can significantly be saved in collaboration with the muon facility group at the MLF.

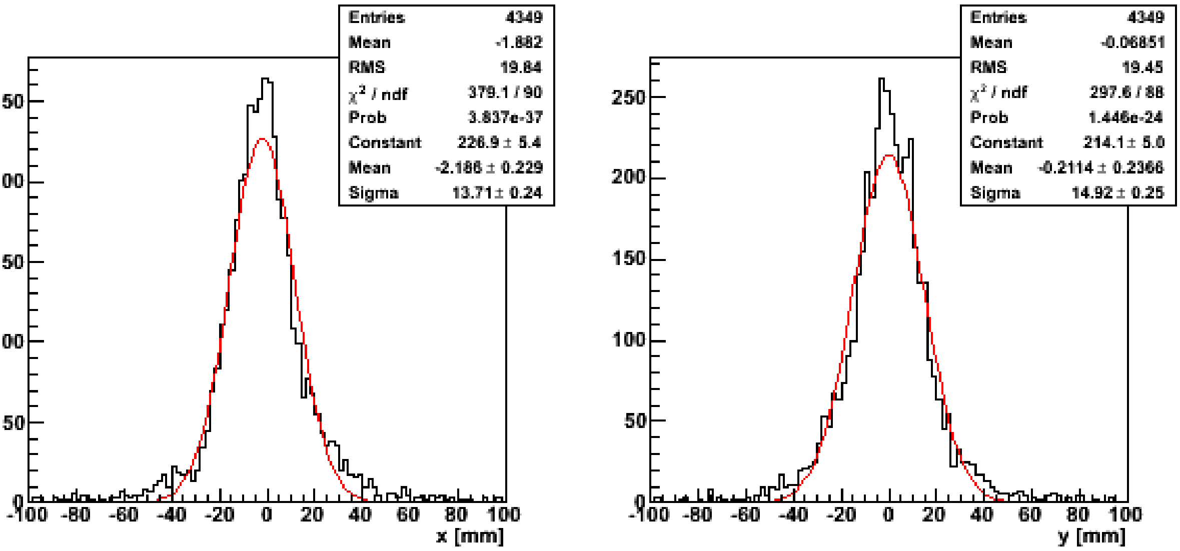

FIG. 17: Horizontal and vertical distributions of the muons at the focus point.

E. Summary

The muon facility has been constructed and operated in the MLF at J-PARC. The proposed experiment utilizes a beam line in the muon facility. The surface-muon intensity from the graphite target is expected to be 10^8/s at the H-2 beam line. The muon transport utilizes capture and transport solenoids to transport the surface muon to the muonium production target.

IV. ULTRA-SLOW MUON PRODUCTION

A. Overview

1. *Development of the Low-emittance Muon Beam*

We plan to create muonium atoms using the 4.1 MeV surface muon beam, in a room temperature muonium production target. The muonium atom will be ionized by a new laser system to provide the intense ultra-cold ionized muon source required for the proposed $g-2$ experiment at J-PARC. This plan is based on work at Rutherford Appleton Laboratory (RAL) and developed jointly by KEK, RIKEN [45, 46]. There, we have utilized the fact that thermal muonium with mean kinetic energy of only 0.2 eV can be produced in vacuum with an efficiency of several per cent by stopping the muon beam in a hot tungsten foil [44] or in SiO_2 powder [47]. Then thermal muonium atoms can be ionized by intense laser radiation, leaving very cold polarized bare muons to be re-accelerated. Recently the conversion from a 4.1 MeV muon beam to a 10 keV muon beam using this laser ionization method was achieved at the RIKEN-RAL muon facility, with an efficiency of about 3×10^{-5} [46]. Although the efficiency achieved is as low as other methods to provide slow muons, and the scheme has an extra complication due to the operation of the laser system, it has huge potential. The ionization efficiency of muonium atoms depends only on the laser intensity and can theoretically be as high as 100%, which would result in a conversion efficiency to slow muons of a few per cent. The energy spread as well as the divergence of the re-accelerated beam is far smaller than other methods of producing cold muons.

In following sections, we describe the slow muon beam line at the RIKEN-RAL muon facility, then describe plans to improve the efficiency of the scheme to match our requirement.

2. *Slow muon beam line at RIKEN-RAL muon facility*

The slow muon setup at RIKEN-RAL muon facility consists of a laser system, an ultra-high vacuum target chamber (for production of muonium atoms), a beam line (slow muon beam optics).

a. Muonium target Figure 18 shows the layout of the target chamber and the slow muon beam line. The initial muon beam with momentum of 28 MeV/c enters the target

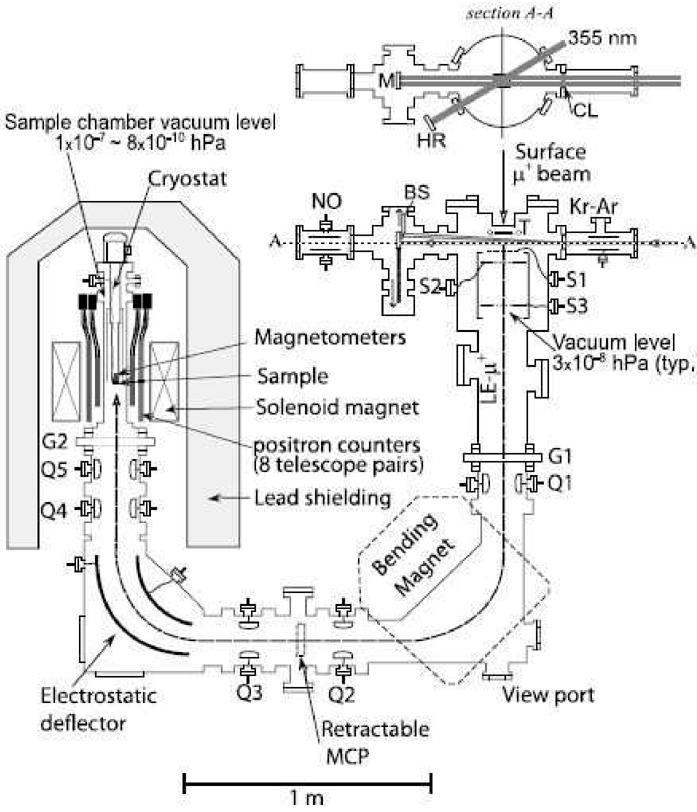

FIG. 18: A experimental layout of the slow muon beam line at RIKEN-RAL muon facility

chamber through a 50 μm thick stainless window and a 20 μm thick tungsten foil, and is stopped inside a 45 μm thick tungsten foil heated by DC current up to 2100 K. The area of the tungsten foil is 40 mm (W) × 35 mm (H). The total thickness of the foils is optimized to stop the largest fraction of the incident muons near the rear surface of the hot tungsten foil, which results in efficient emission of muonium atoms.

b. Laser system and ionization of muonium The binding energy of the electron in muonium is 13.6 eV. The muonium can be efficiently ionized through two-photon resonant ionization via its 2P state. This requires using two laser beams of different wavelengths. Firstly, for the strongly allowed transition from the 1S to 2P state, tunable radiation around 122 nm (Lyman-α) is required. Then for the ionization from the 2P state, a wavelength shorter than 366 nm is required.

Figure 19 shows a schematic diagram for the laser system. The 122 nm radiation is generated through a two-photon resonant sum-difference frequency mixing scheme in a phase-matched krypton gas. This conversion scheme requires two laser beams; one at 212.55 nm

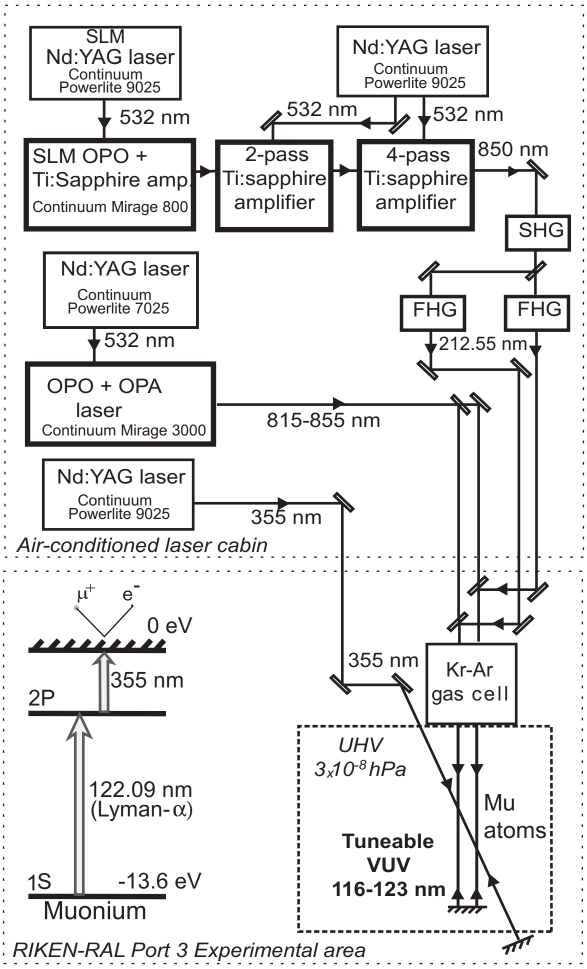

FIG. 19: A schematic diagram for the laser system used at the RIKEN-RAL muon facility

which is matched to a two-photon resonance in Kr, the other at tunable wavelength from 815 nm to 855 nm. This added complication pays off for the following reasons. Firstly it gives a high conversion efficiency ($\sim 10^{-4}$), compared to conventional third harmonic generation in gaseous media. Second, the tunability of the output wavelength allows one to ionize not only muonium, but also residual hydrogen and deuterium atoms in the target chamber. This provides a useful tool for testing the beam line. Lastly, the bandwidth of the output can be customized by using a properly selected infra-red laser. In this setup, the bandwidth of the output was set to be about 180 GHz in order to cover the Doppler width of the thermal muonium from the tungsten foil heated to 2,000 K. For the ionization from the 2P state, the 355 nm laser beam generated as the third harmonic of a Nd:YAG laser is used.

The most crucial part of the laser system is an optical parametric oscillator (OPO) laser

TABLE VIII: Summary of the laser output parameters at RAL

Wavelength	355 nm	212.55 nm	815–855 nm	116–123 nm
Pulse duration	10 ns	4 ns	12 ns	∼4 ns
Pulse energy	380 mJ	10-12 mJ (×2)	12 mJ (×2)	∼0.5 μJ (×2)
Bandwidth	30 GHz	<2 GHz	180 GHz	180 GHz

pumped by frequency-doubling Nd:YAG lasers, which generate single longitudinal mode (SLM) 850 nm wavelength. The output is amplified to high pulse energies in Ti:Sapphire amplifiers, and then converted to 425 nm and then to 212.5 nm by BBO crystals. High quality of the 850 nm laser beam results in high quality and intensity of 212.5 nm, which in turn increases the pulse energy of the Lyman-α wavelength. The current output parameters of the laser system are summarized in Table VIII.

The laser system is operating at a repetition rate of 25 Hz, not the 50 Hz of the muon repetition rate at the RIKEN-RAL muon facility. This limitation is due to strong thermal effects associated with operating high power solid laser systems. Otherwise, the laser system has good long term stability. Stable 24 h/day operation can be sustained for up to 20 days, limited mainly by the lifetime of flashlamps used in Nd:YAG lasers.

The two Lyman-α beams are shaped by focusing optics to have a width of only 1–2 mm in the horizontal plane and about 5–8 mm in the vertical plane, and introduced parallel to the tungsten target at about 5 mm from the target surface. The 355 nm beam is introduced from the top at 30 degrees from the Lyman-α beams and is shaped to have a width of 3 mm by 25 mm. All laser beams are retro-reflected to maximize the ionization yield. Since the retro-reflecting mirrors are placed at a distance of 0.5 m, the width of the ionizing pulse is effectively broadened from 4 ns to 7 ns. The overlap of the Lyman-α and 355 nm beams defines an interaction region where muonium atoms are ionized. The volume of the region is approximately 1 cm^3.

c. Slow muon beam line The slow muons generated by the laser ionization are initially extracted by a low gradient electric field between the tungsten foil held at 9.0 kV and a mesh electrode S1 held at 8.8 kV, separated by 14 mm. S1 is the first of three elements forming an SOA immersion lens, which re-accelerates the slow muons to 9.0 keV as well as focuses the muons to a spot of 2.5 mm (FWHM). The muons are then transported by electrostatic

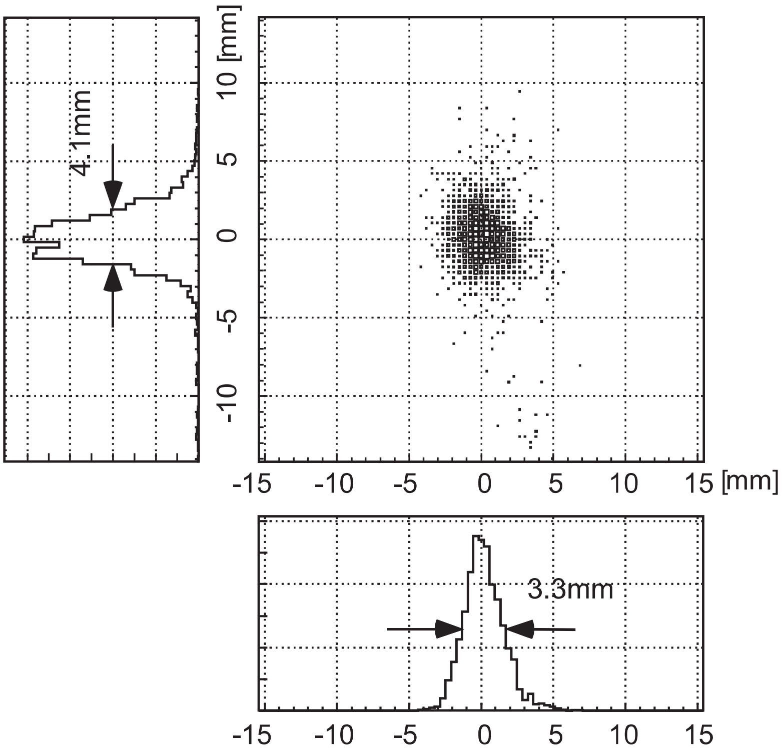

FIG. 20: A beam profile of 9 keV muons at the sample position

quadrupoles, a bending magnet, and an electrostatic deflector, to the sample position at the end. A position-sensitive microchannel plate detector (Roentdek DLD40) can be mounted at the sample position to measure the beam properties.

d. Beam parameters Figure 20 shows the beam spot of the re-accelerated 9 keV muon beam at the sample position. While the FWHM diameter of the incident 4 MeV muon beam is 35 mm, the FWHM diameter of the re-accelerated 9 keV muon beam is about 10 times smaller. The superior quality of the re-accelerated beam can be also seen in its time-of-flight (TOF) spectrum shown in Fig. 21.

While the incident muon beam has a double-pulse structure consisting of 80 ns pulses separated by 320 ns, the Gaussian fit to the TOF spectrum yields FWHM pulse duration of 7.5 ns. Compared to the effective width of ionizing pulse of 7 ns, the energy variation of the re-accelerated beam is very small. The main source of the energy variation is the width of the ionization region, which is of the order of 2 mm (FWHM). The difference in electrostatic potential over the 14 mm gap between the tungsten foil and S1 is kept at 200 V, which means that the 2 mm width of the ionization region contributes to the standard deviation of the muon energy by ~13 eV. Taking into account other factors, such as the uneven distance between the foil and S1 due to bending of the heated tungsten, the standard deviation of the re-accelerated beam is estimated to be approximately 14 eV. This estimation is consistent with the measured μSR asymmetry in a 40 nm thick Al layer on SiO_2 substrate [46].

With the current laser parameters, we observed $\sim 15\mu^+/\mathrm{s}$ at the sample position, which corresponds to an overall conversion efficiency of 3×10^{-5}. The number of available muons is far below that required for the $g-2$ experiment.

There are three main issues to be addressed to use this scheme for the proposed $g-2$ experiment. Firstly, we need to increase the intensity of the incident muon beam. This can be achieved by constructing an all-solenoid muon capture and transport beam line at the MSL facility. Secondly, we need to study the way to produce muonium more efficiently. Lastly, we need to increase the ionizing laser power for muonium. Our measurements show that improvement of the yield can be expected from increases of the pulse energy of the 122 nm and 355 nm beams (Fig. 22). Especially it is worth noting that the power of 122 nm ($\sim$1 μJ/pulse) is still below the saturation intensity of 1S–2P transition. In order to address this challenge, we propose to build a new laser system, based on a newly developed Nd:$GdVO_4$ laser.

In following sections, we first describe a new muonium production scheme under consideration, then describe the new laser system we propose to build. Then the muonium polarization of the re-accelerated muon beam will be discussed, and last, the initial acceleration scheme as a front end to the $g-2$ accelerator/storage complex will be discussed.

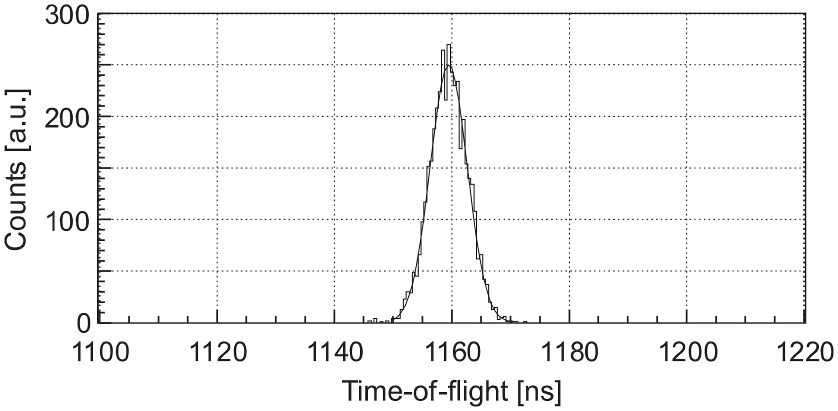

FIG. 21: A time-of-flight spectrum of 9 keV muon beam detected by a MCP at the sample position

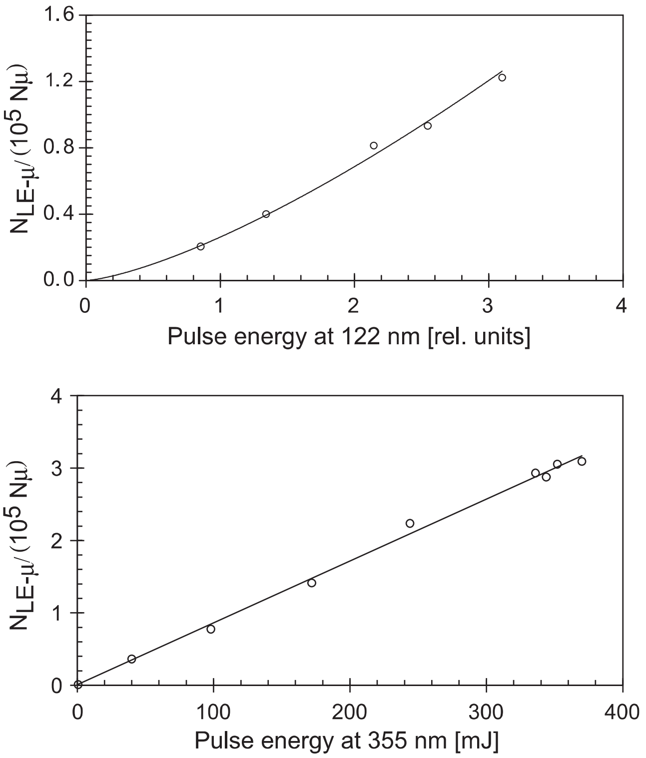

FIG. 22: Dependence of the efficiency of slow muon generation on the laser energies

B. Muonium Production

1. *Muonium Production Target Materials*

Since the transverse momentum is an essential factor in the ultra-cold muon beam for the new muon $g-2$ experiment, we will use a room temperature muonium production target. The average momentum of the muonium at room temperature is 2.5 keV/c. If this is kept in the transverse direction during acceleration to 320 MeV, the ratio of the transverse momentum to the beam momentum is 10^{-5}.

As described above, hot tungsten was used as a muonium production target at RIKEN-RAL. An alternative would be to use silica powder which is known to produce muonium in vacuum with thermal energy at room temperature. There have been several measurements on muonium production from silica powder. The reported efficiency (per incoming muon) for muonium production appers to be about 3% for 27 MeV/c incident muons. Thus, the efficiency of muonium emission is similar for hot tungsten and silica powder.

The production of muonium in vacuum from silica powder was actively studied in the

1980s [47–49]. Muonium is formed with about 60% probability inside silica powder particles [50] and is emitted from the particles with 97% probability [51]. The nominal particle radius is as small as 3.5 nm (Cab-O-Sil EH-5 fumed silica), and can be larger depending on the grade. Diffusion through the voids between particles at thermal speeds allows migration of the polarized muonium atoms over distances of the order of 0.3 mm within the powder in the muon's lifetime. If we form a thin layer target with such powders, the muonium may escape the surface of the layer with significant probability, of order 20% for a layer of thickness 0.3 mm [47–49].

There are other advantages in using a room temperature target such as silica powder rather than high temperature targets. Due to the reduced thermal velocity of muonium, the resonant line for muonium excitation has a smaller Doppler broadening and also the spatial spread of muonium in vacuum is smaller, so we can use the given laser power much more efficiently.

2. Proposed muonium production target search at TRIUMF

Although it is a strong requirement from the muon $g-2$ experiment to use a muonium production target at room temperature, the use of silica powder as the production target has several practical difficulties. Firstly, the powder must be supported by a surface that is not vertical, while most of the beamlines are designed to extract beam horizontally using an electric field. The horizontal spread of muonium in vacuum in the tilted target geometry is larger and the difference in electric potential that each ionized muon feels would widen the beam energy spread. Secondly, we need flatness of the target surface at the mm level so we can fire the laser beam through the vacuum region as close as possible to the target where the muonium density in vacuum is the largest. Since powder targets present challenges in both cases, we hope to find a self-supporting (solid) sample which has a similar or even better yield of muonium.

Silica aerogel is one candidate. Previous measurements on silica aerogel, made 20 years ago, found a very low emission rate (about 1/4) compared with that from silica powder. We expect that more uniform aerogel is now available, for example that used for Cerenkov counters, where the density of the aerogel has been finely controlled to change the refractive index.

We are planning a measurement at TRIUMF for several muonium production targets. The measurement aims at 1) testing several new materials and 2) studying the muonium emission model more precisely. We expect to improve our understanding by systematic measurements on various samples. We propose to image the muonium position with wire chambers. We stop muons in the sample, and detect muonium atoms which emerge from the surface of the sample by tracking positrons from muon decay. Since the ratio of the number of emitted muonium atoms to the number of muons staying in the sample is rather small, we need a position resolution better than the typical separation of the muonium from the sample. Since the thermal velocity is of the order of 5 mm/μs and the time duration is of the order of the muon lifetime (2.2 μs), we need a position resolution of several mm. For this purpose, we plan to use wire chamber tracking.

3. Spatial distribution of muonium in vacuum and overlap with laser

In order to ionize the muonium efficiently with lasers and collect the muons with extraction optics, it is necessary to know the spatial distribution of the muonium and how it develops with time after muon stopping. We are using a diffusion model which was successful in analyzing the previous experiments at TRIUMF. It assumes the motion of the muonium is diffusion like in the silica layer and it freely moves after emission in vacuum with a velocity following a Maxwellian distribution at room temperature. It also assumes an emission angle following a $\cos\theta$ distribution, which results from the maximum depth from which a muonium atom with a given mean free path can exit at a given angle θ from the normal.

Figure 23 shows the result of the diffusion model. The distribution of the muonium position in vacuum (distance from the target surface) is plotted at various timings after the muon stopping. This figure can be used to determine the best timing for the laser shots as well as the region to be covered by the laser beam. Let us assume we shoot the laser at a distance of at least 1 mm from the target surface and that the laser beam is spread for 5 mm in the z direction, giving the best timing of around 400 nsec from the second beam pulse and 1000 ns from the first pulse. In this condition, about 25% of all the emitted muonium will be inside this region.

The two Lyman–α beams used in the RIKEN-RAL experiment had a beam size of 1–

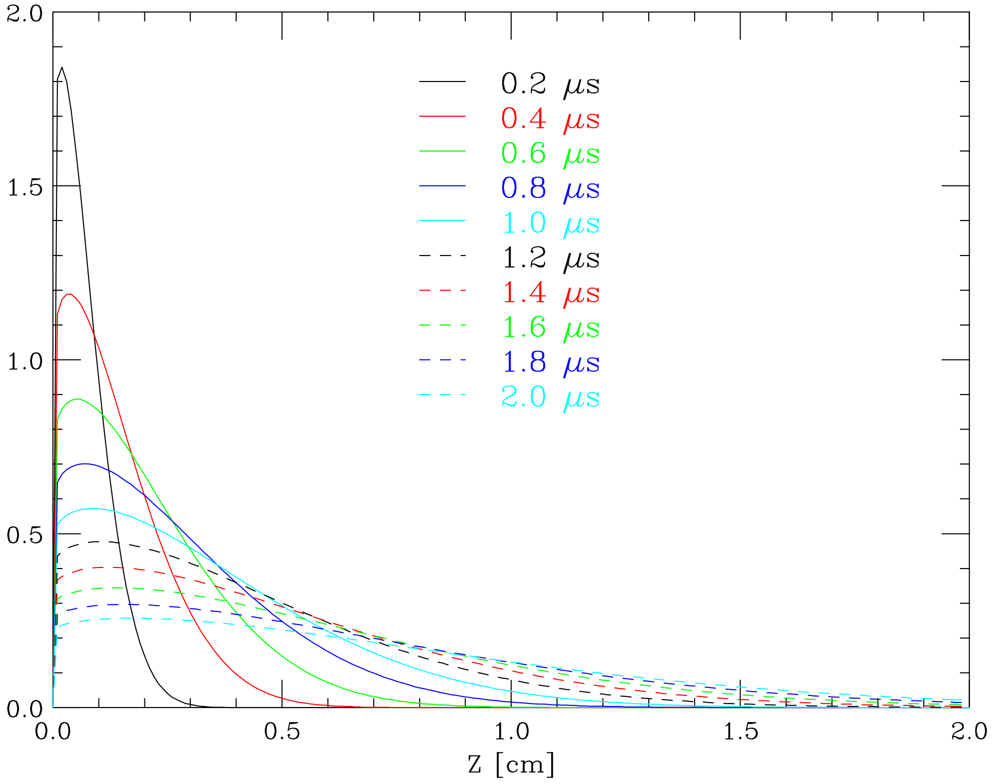

FIG. 23: Simulated result based on the diffusion model. Each profile shows the muonium distribution in vacuum at variuos timings after muon stopping.

2 mm in the horizontal plane and about 5–8 mm in the vertical plane, thus the two beams together covered about 2 mm^2. It would be possible to increase the laser area to 5 mm × 40 mm and still have 10 times more luminosity, because the total power of the new laser is designed to be 100 times larger. So it would be possible to ionize most of the muonium in the irradiated region.

C. Laser System

To ionize the muonium atoms we will apply two photon absorption by muonium in the ground state: vacuum ultraviolet (VUV) laser light centered on the wavelength of the Lyman-alpha (Ly-α) line of the muonium atom photoexcites muonium to the 2p state, then another UV photon (360 nm or shorter) removes the electron. To generate the Ly-α laser light we utilize the two-photon resonant four-wave mixing process in gaseous Kr atoms by pumping in 212.55 nm light (ω_1) to excite it from the bound state to the $4p^5 5p$ state by two-photon absorption, then 820 nm light (ω_2, tunable 815 $\sim$ 850 nm) generates the Ly-α light by difference frequency generation (Fig. 24). In this method the key issue is how to increase the power of the Ly-α laser to be sufficient for the target slow muon production. Generation of high intensity VUV is difficult because of an absence of a non-linear frequency conversion crystal in wavelength shorter than 200 nm. Therefore historically researchers applied the optical conversion processes in gaseous atoms, such as Kr, Xe, and Hg, to generate coherent light in VUV region. However the conversion efficiency has always been an issue in this method. Conversion efficiency was measured to be $\sim 10^{-4}$ to 10^{-5} with power output 10 μJ/laser pulse at most, even though the Ly-α is such an important wavelength. Here we set our goal to be 100 μJ, 1 ns, 80 GHz spectral width, and 25 $\sim$ 50 Hz repetition rate of the pulsed Ly-α output by having high-intensity pump lasers (especially ω_1), and a conversion efficiency of 10^{-3} by performing experiments and simulations to find the best conditions for this wavelength conversion process.

1. ω_1 and ω_2 laser

   The VUV generation in Kr occurs in a range of the so-called small-signal gain where the conversion efficiency is proportional to $P_1^2 P_2$, where P_1 and P_2 are the laser power for ω_1 and ω_2 respectively. To achieve the above-mentioned goals, it is estimated that both P_1 and P_2 need to be approximately 100 mJ/pulse when the pulse duration is 1 ns. A light source of 100 mJ/pulse of 212.55 nm at 50 Hz (when synchronized with the muon source at RIKEN-RAL) already sounds challenging, but it is technically feasible by utilizing the following laser system:

   (a) ω_1 laser system

      i. **fundamental for the ω_1 laser**

         To generate high-intensity 212.55 nm laser light we utilize the 5th order harmonic of 1062.75 nm (fundamental), which is an output of a distributed feedback laser diode (DFB-LD) that enables oscillation at the single longitudinal mode with narrow linewidth ($\sim$2 GHz). The fine tuning on the central wavelength of the DFB-LD by changing the LD temperature is very important in this application because the two-photon resonant absorption in Kr has a well-defined excitation energy. Since the LD has relatively short optical cavity length, it has less jitter and the temporal shape of the input electric current directly appears as the laser output. Therefore it is possible to change the laser repetition rate and pulse duration just by controlling the electric circuit. To obtain sufficient power for the ω_1 laser it is necessary to have enough power of the fundamental, which we estimate to be approximately 1 J/pulse considering the conversion efficiency of the nonlinear crystal. To amplify the seed output from the DFB-LD we consider the multiple amplification stages as shown on Fig. 25.

ii. **Fiber amplifier**

The seed output from the DFB-LD is first amplified by the fiber amplifier to an order of 10 μJ /pulse. For the non-linear wavelength conversion it is important to keep the linear polarization and large extinction ratio, and to avoid the spectral broadening due to the self-phase modulation in the fiber medium. Currently we have completed the DFB-LD and amplification stages up to this point with the expected output energy (10 μJ /pulse).

iii. **Regenerative and Multi-pass amplifier**

The second amplification stage is a regenerative amplifier with Nd:YGAG crystal as a gain medium, which resembles the traditional Nd:YAG crystal but has Ga substituting part of the Al atoms, so that the central wavelength is tuned to the target wavelength (1062.75 nm). Currently this part is under development. If the amplification turns out to be not sufficient with the regenerative amplifier only, we will consider an additional multi-pass amplifier.

iv. **Nd:GdVO$_4$ single pass amplifier**

Finally the pulse train is amplified by a single pass amplifier with a Nd:GdVO$_4$ crystal as the gain medium which our collaborators have recently developed [52]. Its gain spectrum is peaked at 1062.9 nm with 2 nm bandwidth, so it can amplify our fundamental very close to the center of its spectrum. If the amplification turns out to be still not sufficient we will add one more stage for further amplification.

v. **Non-linear wavelength conversion**

The amplified fundamental pulse (1 J, 1 ns pulse duration) is now converted to 1 by the nonlinear frequency conversion system as show in Fig. 25. We utilize an LBO crystal for the second harmonic generation and CLBO crystals for the 4th and 5th order harmonic generation, with a goal of 10% for the conversion efficiency (thus 100 mJ/pulse of 212.55 nm). An important point here is the use of CLBO crystals, which gives high conversion efficiency, although a low damage threshold has prevented it from being practical. We have studied the characteristics of the crystal in detail and found an approach for long-term stable operation.

(b) ω_2 laser system

For the ω_2 laser we use the DFB-LD as an oscillator in a similar way as for the ω_1 laser system, and then amplify the output pulses by the optical parametric amplification (OPA) with an LBO crystal. In this case the pump laser for OPA is a portion of the second harmonic generated during the ω_1 process described above (subsection 1(a)v). Our goal here is 100 mJ, 1ns pulse duration of 815 $\sim$ 850 nm. This output level should not be so difficult because the technology is more established in this wavelength region.

2. Ly-α laser light generation using Kr gas

Both the ω_1 and ω_2 lasers are collimated and incident on a gas cell for the Ly-α laser light generation. The gas cell contains Kr and Ar gas by a constant fraction for the wavelength conversion. Here Ar is necessary to satisfy the phase-matching condition, $\Delta k = 0$, where k indicates a wave vector and $\Delta k = k_{Ly-\alpha}$ - $(2k_{\omega_1} + k_{\omega_2})$. Since Kr has negative dispersion in the wavelength of Ly-α, it is necessary to have Ar to give a positive dispersion so that the system has a solution for $\Delta k = 0$ and to achieve the best conversion efficiency. Unfortunately there was no work so far that systematically studied the conversion efficiency as a function of the relevant parameters, such as the partial pressure ratio, absolute pressure, beam intensity, and so on. We need to start by measuring some fundamental optical parameters such as the third-order susceptibility of Kr at Ly-α wavelength, therefore it requires a serious R&D to achieve 10^{-3} conversion efficiency. We have started doing experiments and simulations at a laser laboratory in RIKEN-Wako. We are planning on finishing the Ly-α laser system during the second half of 2010 and installing it at RIKEN-RAL for the experiment of slow muon production.

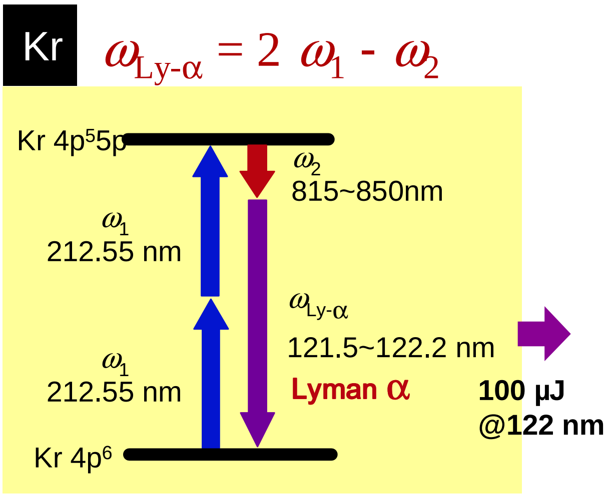

FIG. 24: Schematic diagram of four-wave mixing process in Kr

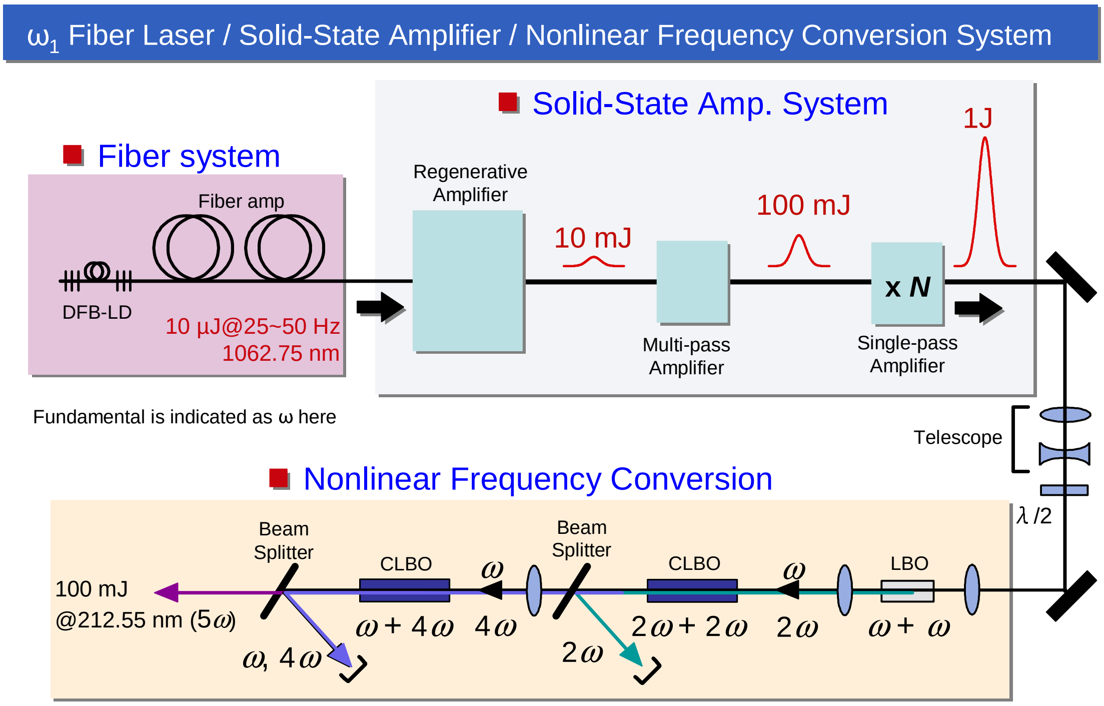

FIG. 25: laser system for generating ω_1, 212.55 nm

D. Spin Polarization

1. Muon spin in muonium

Muonium is a bound state of a muon and an electron. Its hyperfine splitting between the spin singlet state and the triplet state has been measured as $\nu_{\rm HFS}(= 2\pi\omega_{\rm HFS}) = 4.463$ GHz [53].

Suppose the incident surface muon is 100% polarized, and the electron it captures is unpolarized, then half of the muonium ensemble is formed in the state where the spin of the electron is parallel to that of the muon, denoted as $|++\rangle$, and another half of the ensemble is in the state with spin anti-parallel, $|+-\rangle$. Since the $|++\rangle$ state is a spin-triplet energy eigenstate, the total spin of muonium and the muon spin are stationary. Therefore, the muon polarization in the $|++\rangle$ state is kept. On the other hand, the $|+-\rangle$ state is not an energy-eigenstate, but a mixture of a spin singlet and a triplet states. The $|+-\rangle$ state oscillates to the $|-+\rangle$ state in a time scale of 1/(4.463 GHz) = 0.224 ns [54]. The average thermal velocity of the muonium at room temperature is 8 mm/μs. It takes at least a hundred ns for muonium to diffuse/drift to the region of the laser beam (about 1–2 mm from the target surface). Therefore, by the time muonium is ionized, the $|+-\rangle$ state and the $|-+\rangle$ state are equally populated, resulting in zero polarization of the muon. Since the initial ensembles of the $|++\rangle$ and the $|+-\rangle$ states are equal, the polarization of the ultra-slow muon is (100% + 0%)/2 = 50%.

2. *Possible recovery of polarization*

Two possibilities of recovery of muon polarization are being considered.

a. Longitudinal magnetic field If the magnetic field is applied in parallel to the initial muon polarization, total muonium spin is no longer a good quantum number. In the limit of the strong magnetic field, the spin component along the magnetic field becomes a good quantum number. Thus, the muon spin in the $|+-\rangle$ state will also be "locked". The dependence of the muon polarization P_μ with the magnetic field strength B can be written as [54]

$$P_\mu = \frac{1+2x^2}{2(1+x^2)}, \tag{12}$$

with

$$x = \frac{(g_e\mu_e + g_\mu\mu_\mu)}{2\hbar\omega_{\mathrm{HFS}}}B = 13[\mathrm{T}^{-1}]B. \tag{13}$$

Figure 26 shows P_μ as a function of B in the region $0 < B < 0.5$ T. The muon polarization increases from 50% to 96% with a longidudinal magnetic field of 0.3 T in the region of the muoninum target and laser ionization.

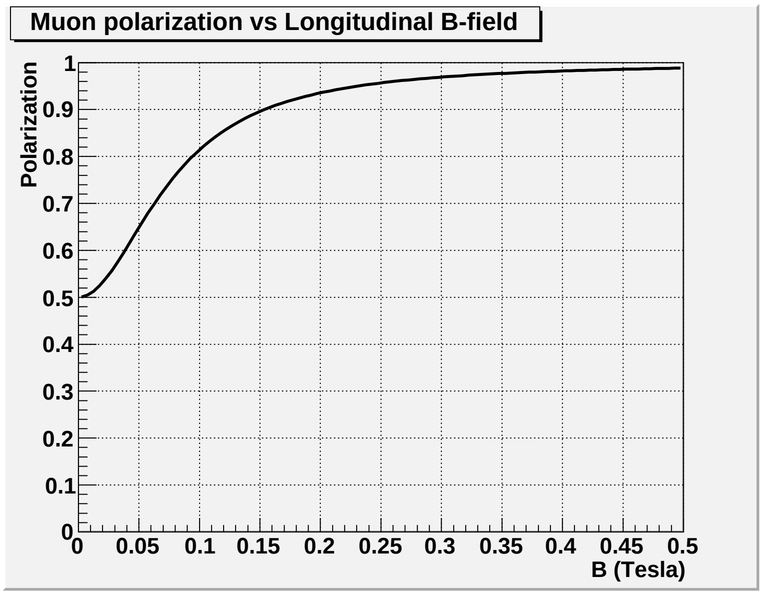

FIG. 26: Muon polarization in muonium as a function of the londitudinal magnetic field

The primary challenge of this method is the muon beam transport after the ionization under the circumstance of the magnetic field. The muon transport in the initial acceleration must be carefully designed so that transverse kick to the muons from the fringing field of the spin holding magnet is sufficiently small to preserve the transverse dispersion. We plan to study feasibility of introducing such magnetic field and beam transport configuration to increase the muon polarization.

b. Narrow band laser The singlet state and triplet states are selectively ionized if the laser band width is narrower than the hyperfine splitting ν_{HFS}=4.463 GHz. The narrow band laser can be used to sweep out the depolarized muons in the unfavorable singlet state in advance to the normal ionization scheme. This way, the polarization increases from P =50% to (100%+0%)/1.5 = 66%, and we lose 1/4th of muons by sweep out. We gain the figure of merit ($\propto NP^2$) by a factor of 1.33.

E. Initial Acceleration

In this section, we describe the muon initial acceleration scheme after the muonium laser ionization, up to the main acceleration using LINACs, as described in section V. A key issue is to minimize / confine the muon bunch time-width. Because we need to inject the muon bunch into an extremely limited space-time of the acceleration RF field of the LINACs, we need both excellent emittance and a sharp time-width at the same time. The time-width must be much narrower than the RF frequency, otherwise one loses the control of the off-phase component.

Another key issue is to avoid introducing additional relative muon motion in a muon bunch at the initial acceleration, because the relative motions viewed by the rest frame of the bunch is the temperature of the muon bunch. This heating-free acceleration is one of the most critical parts to realize the new $g-2$ experiment. We propose to construct the initial acceleration stage keeping cylindrical symmetry to reduce second-order aberration, except for a higher order aberration compensator such as electro-static sextupoles. For the design of the initial acceleration stage, one can apply the technique developed for the electron microscope. Together with a conventional initial acceleration scheme, we also propose to apply a muonium motion-cancellation mechanism using the Doppler shift of $1S$-$2P$ transition energy by the high-intensity chirped Lyman-α laser, for further temperature reduction of the muon bunch.

Thus, we need to control muon beam very precisely both longitudinal and radial motion by pulse extraction field and cylindrical initial acceleration stage, respectively, as it is described in detail as follows.

1. *Cylindrical initial acceleration stage*

The simplest and ideal muon acceleration scheme, up to required muon energy for new muon $g-2$ measurement, is acceleration of parallel and static electric field, namely Cockcroft-Walton type, because there is absolutely no possible heat source during the acceleration. However, it is not realistic at all to accelerate more than few tenth of MeV. Therefore, one need to combine several acceleration method to reach the required muon energy.

In the low energy region, however, one of the good model is parallel and static electric field, but the present muon source is not that simple because of rather large source size. Before the injection to the acceleration field, one need to focus the laser-ionized muon to utilize only homogeneous region of the field, otherwise the system becomes unreasonably huge.

The better model is electron microscope instead of the simple Cockcroft-Walton. If all the initial acceleration components have cylindrical symmetry without magnetic field, the equation of the particle tracks close to the beam axis can be represented as

$$\frac{d^2x}{dz^2} + \frac{1}{2\Phi}\frac{d\Phi}{dz}\frac{dx}{dz} + \frac{1}{4\Phi}\frac{d^2\Phi}{dz^2}x = 0 \tag{14}$$

$$\frac{d^2y}{dz^2} + \frac{1}{2\Phi}\frac{d\Phi}{dz}\frac{dy}{dz} + \frac{1}{4\Phi}\frac{d^2\Phi}{dz^2}y = 0, \tag{15}$$

where Φ is the electric potential on axis, $\Phi = \phi(0, 0, z)$. From the equations, it is clear that the tracks are independent of the charge mass ratio e/m, thus the trajectories should be same for electrons and muons. If there is higher order aberration in the initial acceleration stage, the muon bunch can easily heat-up because uncontrollable relative motions are introduced due to the aberration. The equations have cylindrical symmetry, so the second order aberration cannot be exist, which simplifies the aberration control. Because there exists an MV class electron microscope, it is feasible to apply that technology for the muon initial acceleration.

2. *Primary design of the initial acceleration*

Figure 27 shows the schematic setup for the initial acceleration scheme. The surface muon from the production target is transferred to the muonium generation target by a large solid angle solenoid channel, and accumulated to the central axis by a capillary method [55] using capillary shaped heavy material. The ionization laser will be injected just behind the muonium target to have maximum yield.

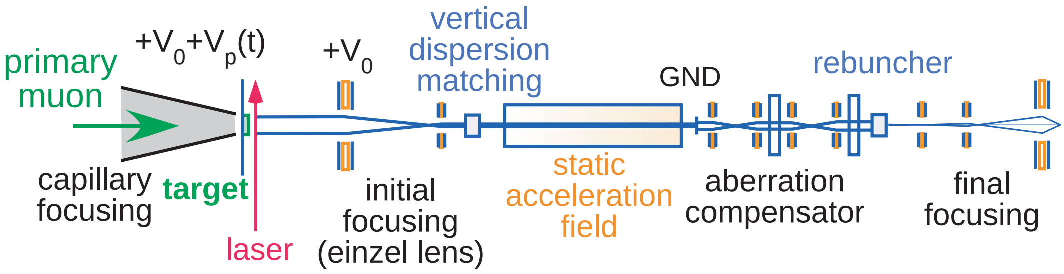

FIG. 27: Schematic setup for the initial acceleration.

The extraction field will be generated by applying slightly higher voltage to the muonium target holder than the bias of the initial focusing element. Double einzel lenses will be used to form a weakly-focused parallel beam to confine the muon beam diameter. After the double einzel lenses, one can place an electrical element to cancel the vertical dispersion in the case where a pulsed extraction field is applied. The weakly-focused parallel beam is further accelerated by the static parallel field, and the higher order aberration is canceled by an aberration compensator composed by four einzel lenses and two sextupole lenses located behind the static parallel field.

To compress the muon beam bunch in time, one needs a re-buncher to rotate the phase of the muon bunch, and then apply final focusing elements before injection into the LINAC. By a static extraction field, longitudinal momentum dispersion depends on the ionization position along the axis, so one can realize very short time-width muon bunch in the order of a few psec at few 100 kV acceleration, assuming primary muon is few cm in size. The pulse width after the re-buncher is dominantly limited by the dispersion of the path length at the initial focus. Obviously, the weaker focusing design results in shorter time spread of the muon bunch. On the other hand, one can produce a linear correlation between the ionization timing and the longitudinal velocity of the cold muons, hence a correlation between the ionization timing and the longitudinal position dispersion, by using a pulsed extraction field. If one applies a chirped-laser pulse whose central energy shifted in time, then we can sweep thermal transverse momentum in time according to the Doppler shift of the muonium, so one can cool the muon below the room temperature. In this case, the time-width after the re-buncher is limited as $\sim \Delta l_{lp}/(\beta_0 c)$, where Δl_{lp} is the longitudinal laser size and $\beta_0 c$ is the central velocity after the initial acceleration, and few 10 psec pulse width can be realized at few 100 kV acceleration, assuming laser size of about 1 mm. One needs more detailed design study to finalize the configuration of the final focusing elements to fulfill the matching condition with LINAC injection.

F. Summary

The proposed experiment utilizes the ultra-cold muon source which can be produced by the laser ionization of muoniums. The laser ionization technique has been developed by KEK and RIKEN, and continuously improved at the RIKEN-RAL muon facility. The efficiency to produce the ultra-cold muon from the surface muon beam is 3×10^{-5} at RAL.

A new laser system is currently under development at RIKEN to increase the laser power by a factor of 100. With the 100 times intense laser, we expect the efficiency to be two orders of magnitude higher, i.e. 3×10^{-3}, which will be confirmed by the test experiments at RAL and J-PARC. The surface muon intensity at the J-PARC H-2 beam line will be 10^8/s (see section IV B). Therefore, a conservative estimate of the intensity of the ultra-slow muon beam would be $3\ \times10^5$/s. Here, we note that one can expect additional factors of improvements in the effficiency from (1) better muonium-production efficiency with new target material, and (2) better ionization efficiency at room temperature (as opposed to 2,000 K for the hot tangsten target). These improvement factors are to be determined in the test experiment proposed at TRIUMF in 2010.

The default polarization of the ultra-cold muon is 50%. R&D to improve the polarization is in progress based on the ideas of introduction of a londitudinal magnetic field, or a narrow band laser. Initial acceleration will use the weak static electric field, follwed by double einzel lenses, the static acceleration field, a re-buncher, and a focusing elements. Cooling of the muon beam even below the room temperature would be possible by utilizing a chirped-laser.

V. RE-ACCELERATION

The ultra-cold muons created in the muonium target regeon must be reaccelerated to around 300 MeV/c in momentum (210 MeV kinetic energy) to then be injected into the muon $g-2$ storage ring. To suppress muon loss in the course of reacceleration, the muons should be accelerated in a sufficiently short period of time compared with the muon life time of 2.2 μs. To realize fast reacceleration, we plan to build a linac dedicated for this purpose. A linac has an overwhelming advantage over circular accelerators in shortening the reacceleration time.

Another essential requirement for the reacceleration is the suppression of transverse emittance growth. The ultra-cold muons will have an extremely small transverse momentum of around 30 keV/c with an tranverse spacial extent of around 10 mm. Assuming an ideal acceleration to 300 MeV/c, the typical transverse divergence angle of muons becomes 10^{-5} rad. These are the requirement for injection into the storage ring. Therefore, the beam at injection should have essentially the same normalized transverse emittance as that at the muon source. Consequently, the transverse emittance growth in the linac should be suppressed as much as possible to meet this requirement.

In the design consideration of this linac, we separate the acceleration into two sections, namely, a low-β section and a high-β section. In the low-β section, we assume the acceleration of muons from around 10 keV to 43 MeV in kinetic energy. This corresponds to accelerationg β from 0.01 to 0.7. The muons accelerated in the low-β section are delivered to the high-β section, where they are further accelerated to 210 MeV.

In the low-β section, the particle β increases rapidly with kinetic energy. Accordingly, it becomes very important to adopt an adequate accelerating structure matching β. To the contrary, the β variation in the high-β section is modest. Then, its design emphasis is naturally shifted to achieving a high accelerating gradient to realize sufficiently fast reacceleration.

In the following two subsections, we review the proposed design for the low-β section and the high-β section of the linac, respectively.

A. Low β linac

As mentioned above, the particle β changes rapidly in the low-β section as its kinetic energy increases. Then, a suitable accelerating structure should be chosen for each β range. This situation is essentially the same as in a usual proton linac. Therefore, we basically follow the conventional configuration for a proton linac in the design of the low-β section. In addition, we put the emphasis on making the best use of J-PARC experience to reduce the R&D burden. It should also be noted here that the space-charge effect is not an issue for the linac even at its lowest energy, because the number of muons assumed per bunch is as small as around 50,000. This is an important difference from a usual proton linac, where the design emphasis is often put on suppressing the space-charge effect.

We here divide the low-β section into three parts, namely, the front-end part ($\beta < 0.08$), the low-β part ($0.08 < \beta < 0.45$), and the medium-β part ($0.45 < \beta < 0.7$). For the low-β part, we plan to adopt a DTL (Drift Tube Linac) of Alvarez type with the operating frequency of 324 MHz. This operation frequency is chosen to be the same as the J-PARC DTL [56]. With this choice, we can use the existing J-PARC klystron for its RF source avoiding an R&D burden.

As for the medium-β section, we plan to adopt an ACS (Annular Coupled Structure linac) [57]. The ACS is a variation of a CCL (Coupled Cavity Linac), and adopted for the energy upgrade of the J-PARC linac. The ACS is advantageous in suppressing the dipole component of the RF field, having an annular symmetry for the coupling cell [57]. The operation frequency for the ACS is chosen to be 972 MHz with a three-fold frequency jump from DTL. This frequency is again the same as J-PARC ACS to utilize 972-MHz klystrons developed for it [56].

It should be noted that both the DTL and the ACS are standing-wave structure, and it is a conventional choice for a proton linac. This is constrasted with the high-β section where a traveling-wave structure is assumed.

In the linac design, it is important to optimize the particle β where the accelerating structure is switched from one to another. We here assume the transition β of around 0.45 between DTL and ACS. While it is a conventional choice for a proton linac, there still remains a room for further optimization. We should note here that the transition β is usually determined to optimize the effective shunt impedance. In other words, we will have wider flexibility by tolerating inefficient use of RF power. As efficient power consumption is not such a pressing requirement for our purpose, the choice of the transition β will be subject to further optimization in the coming design work.

For the front-end part, we plan to adopt a Cockcroft-Walten injector instead of an RFQ (Radio-Frequency Quadrupole linac). In a modern proton linac, an RFQ is usually adopted for the front-end, where a continuous beam injected from an ion source is gradually bunched and RF captured for acceleration. This bunching capability greatly improves the transmission efficiency of a proton linac compared with a classical Cockcroft-Walton injector. However, this bunching capability is not necessarily advantageous for our purpose, because the muons generated at the muon source already has a bunch structure generated by an excitation laser. Meanwhile, an RFQ is known to have a substantial nonlinear component of the RF field due to unavoidable deviation of its vane shape from the ideal one [58]. The nonlinear component can be a source of transverse emittance growth, which should be strictly suppressed for our purpose. While we need further study on the effect of the nonlinear component, we here assume a Cockcroft-Walton injector for the front-end with an RFQ as an alternative option.

To adopt a Cockcroft-Walten injector, it is required to have an additional RF cavity for bunch compression. The bunch length from the muon source is assumed to be around 100 ps. As this bunch length is too long to be accepted by a 324-MHz DTL, we need to perform bunch compression before injecting into the DTL. To this end, we plan to have a buncher cavity between the Cockcroft-Walten injector and the DTL. We here assume a simple single-gap cavity of 324 MHz for this purpose.

Figure 28 shows the proposed configuration of the low-β linac. Plan A shows the present baseline design with a Cockcroft-Walten injector, and Plan B shows an alternative plan with an RFQ as the front-end. In both plans, we can adopt the same design for DTL and ACS. In the baseline design, the low-β linac consists of a 0.34-MeV Cockcroft-Walten injector, a single-gap buncher cavity, a 13.8-MeV DTL, and a 43-MeV ACS. The DTL section consists of one DTL tank driven by a 324-MHz klystron. Meanwhile, the ACS section consists of six ACS tanks. Two neighboring ACS tanks are connected with a bridge coupler, and driven by a 972-MHz klystron. We plan to adopt klystrons of J-PARC type both for 324 MHz and 972 MHz. The saturation power for the klystrons is 3.0 MW for both 324 MHz and 972 MHz. As for the buncher cavity, we plan to adopt a solid state amplifier as its RF source. The required RF power for the buncher cavity is estimated to be kW level or even less, and is easily fed by a solid state amplifier.

Table IX and X show the main parameters for the DTL and ACS, respectively. It is readily seen in these tables that the main parameters are comparable with the J-PARC design except that the muon DTL and ACS cover a little wider β range. This difference arises because we omit the SDTL (Separate-type DTL) [59] section in the low-β linac to reduce the number of transitions. On the other hand, SDTL is adopted in J-PARC to improve the power efficiency in the β range between DTL and ACS [56].

As shown in these tables, we plan to adopt the synchronous phase of -30 degree to attain sufficient acceptance in the longitudinal phase space. With this choice of the synchronous phase, the RF field provides the muon beam with longitudinal focusing, but in turn it defocuses the beam transversely. Accordingly, it is required to provide transverse focusing to compensate the RF defocusing force. In the DTL, we plan to equip each drift tube with a quadrupole magnet as in a conventional DTL. The transverse focusing is provided with these DTQ's (Drift Tube Quadrupole magnets) with a so-called FODO lattice. In the ACS section, a quadrupole doublet is placed at each inter-tank spacing to provide transverse focusing. An additional solenoid magnet is also assumed before the DTL injection to match the beam size by focusing the beam from the Cockcroft-Walten injector.

For this baseline design, proper beam transport through the low-β section is confirmed with the Trace3D code [60] as shown in Fig. 29. In this figure, the calculation is performed from the exit of the Cockcroft-Walten injector to the exit of ACS. We assume a 2.4-m long matching section between the injector and DTL, and a solenoid magnet and a buncher cavity are assumed there for transverse focusing and bunch compression, respectively. The Trace3D code calculates the time-evolution of the phase-space beam ellipses, and hence beam envelopes, along the linac. The top left figures in Fig. 29 show the phase-space beam ellipses assumed at the injector exit, and the top right figures those obtained at the ACS exit. The bottom figure shows the calculated beam envelope along the beam line from the injector exit (at the left end) to the ACS exit (at the right end). It is seen in this figure that the beam can be matched with a rather simple configuration of a solenoid magnet and a buncher cavity. Then, the beam envelope through the low-β linac is sufficiently controlled.

Proper beam acceleration is also confirmed with a preliminary particle simulation. The simulated particle distribution at the ACS exit is shown in Fig. 30. In this simulation,

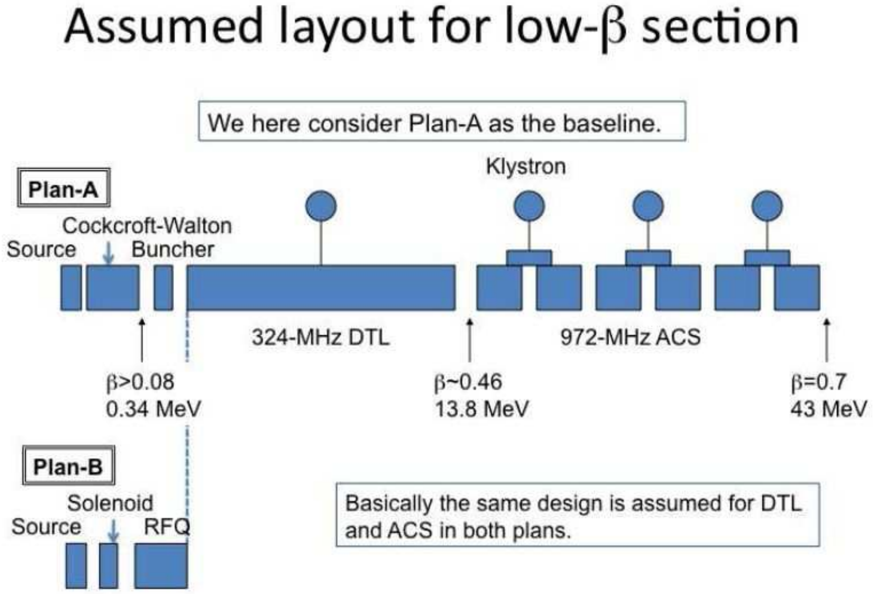

FIG. 28: Schematic layout of low-β linac.

an initial Gaussian distribution is generated at the DTL entrance with 50,000 simulation particles. Then, they are tracked through DTL and ACS assuming a realistic RF field and a hard-edge quadruople magnetic field. For this tracking, the IMPACT code [61] is utilized turning off the space-charge calculation. An RMS emittance growth of around 7% is observed in the simulation. This growth is believed to be induced by the nonlinear nature of the RF defocusing force. While the shape in the transverse phase space also shows some distortion in this figure, it is assumed to be at a tolerable level.

TABLE IX: Main parameters for DTL.

	Muon DTL	J-PARC DTL
Number of cells per tank	33	146
Number of tanks	1	3
Operating frequency	324 MHz	324 MHz
Cavity type	Alvarez-type	Alvarez-type
Averaged accelerating field E_0	2.5 MV/m	2.5 MV/m
Synchronous phase ϕ_s	-30 degree	-30 degree
Kinetic energy at the entrance	0.34 MeV	3.0 MeV
Kinetic energy at the exit	13.8 MeV	50.1 MeV
β at the entrance	0.080	0.080
β at the exit	0.462	0.313
Wall loss per tank	0.83 MW	1.1 MW
Total length	8.82 m	27.1 m
Traversing time	99 ns	

TABLE X: Main parameters for ACS.

	Muon ACS	J-PARC ACS
Number of cells per tank	17	17
Number of tanks	6	42
Operating frequency	972 MHz	972 MHz
Cavity type	ACS	ACS
Averaged accelerating field E_0	4.36 MV/m	4.12 MV/m
Synchronous phase ϕ_s	-30 degree	-30 degree
Kinetic energy at the entrance	13.8 MeV	190 MeV
Kinetic energy at the exit	43 MeV	400 MeV
β at the entrance	0.465	0.555
β at the exit	0.703	0.712
Wall loss per tank	0.82 MW	0.73 MW
Total length	14.76 m	107.1 m
Traversing time	80 ns	

Trace3D simulation: Whole low-β section

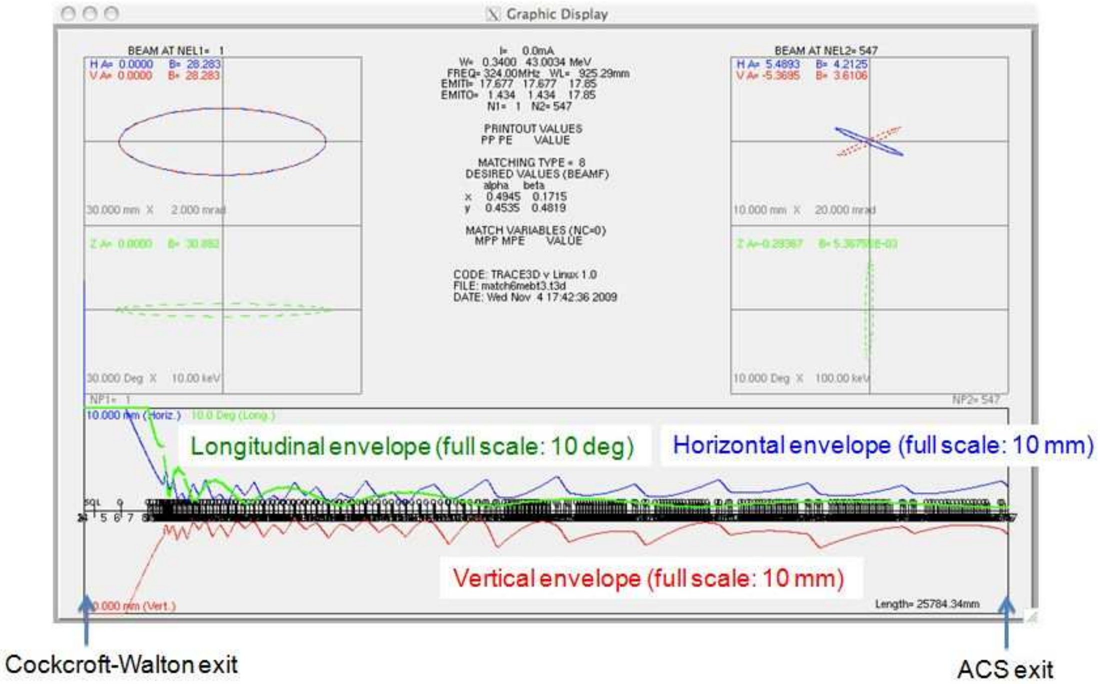

```
I=   0.0mA
W=  0.3400   43.0034 MeV
FREQ= 324.00MHz   WL=   925.29mm
EMITI= 17.677   17.677   17.85
EMITO=  1.434    1.434   17.85
N1=  1   N2= 547

PRINTOUT VALUES
PP PE      VALUE

MATCHING TYPE =  8
DESIRED VALUES (BEAMF)
     alpha    beta
x    0.4945   0.1715
y    0.4535   0.4819

MATCH VARIABLES (NC=0)
MPP MPE      VALUE

CODE: TRACE3D v Linux 1.0
FILE: match6mebt3.t3d
DATE: Wed Nov  4 17:42:36 2009
```

FIG. 29: The beam envelope along the low-β linac calculated with Trace3D.

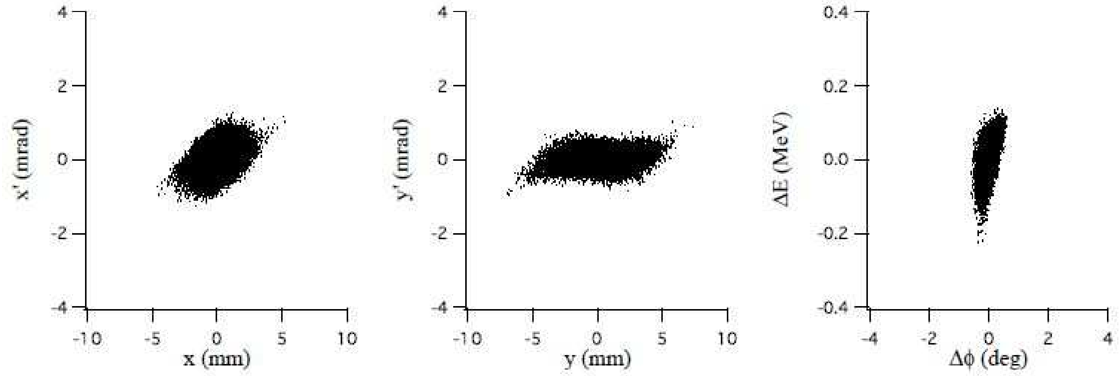

FIG. 30: The particle distribution at the exit of the low-β linac simulated with IMPACT

B. High β section

The high β section of the muon linear accelerator is designed to re-accelerate from 100 MeV/c to 300 MeV/c. As the basic design of the high β section, a disk-loaded traveling wave accelerating structure, which is similar to an electron linear accelerator, was selected. The advantage is its high electric field of around 20 MeV/m to shorten the accelerator length. Figure 31 is the typical accelerating structure of the electron linac. The emittance and bunch length of the muons are small enough to accelerate using such a disk-loaded structure, though the available phase space becomes less due to the higher frequency. However we have to evaluate the phase stability and determine the frequency to minimize the emittance growth.

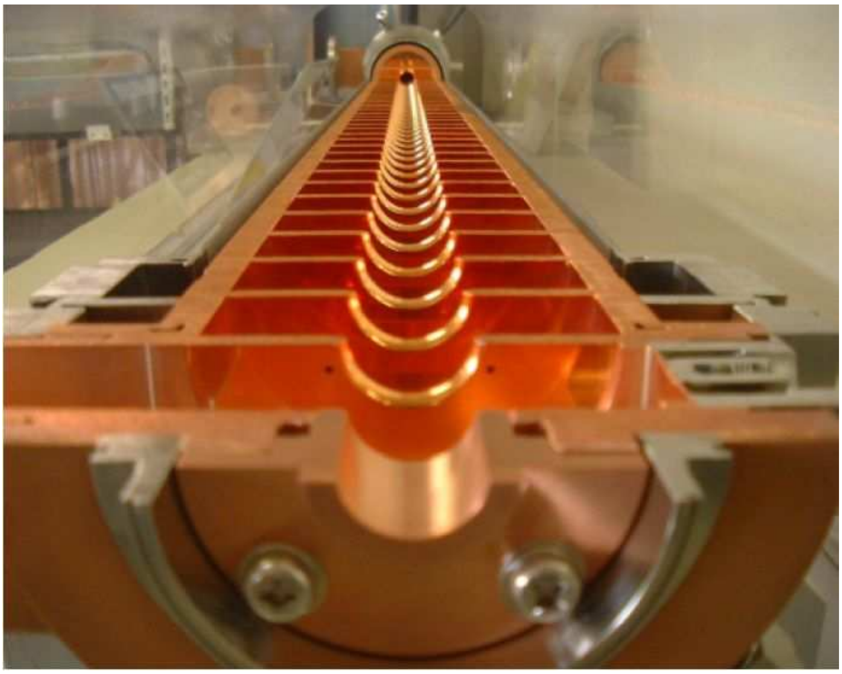

FIG. 31: Disk-loaded accelerating structure.

The particular design item of the disk-loaded structure for the muon acceleration, which is different from the general accelerating structure for the electron accelerator, is the variation of the disk spacing corresponding to the muon velocity.

The design procedure of the phase velocity matched disk-loded structure is as followings,

- The disk spacing is generated in turn to pass the center of each cavity at a given RF phase for a test particle.

- The test particle is tracked through the electromagnetic field of the cavity which is calculated utilizing the series expansions and impedance matching method [62] without mesh.
- The particles at the end of the low β section are tracked in the cavity chain.

As the initial condition for the accelerating structure, we selected the RF frequency of 2856 MHz which is used in many electron accelerators. The optional candidate of the RF frequency is around 1300 MHz for the wider phase space. Further the constant gradient structure was adopted, the input power is 8 MW for each accelerating structure and the ratio of the power attenuation constant usually described as τ is selected to 0.5. Figure 32 shows the disk spacing and the length of the accelerating structure corresponding to the muon momentum. It consists of only four accelerating structures and the total length is around 10 m.

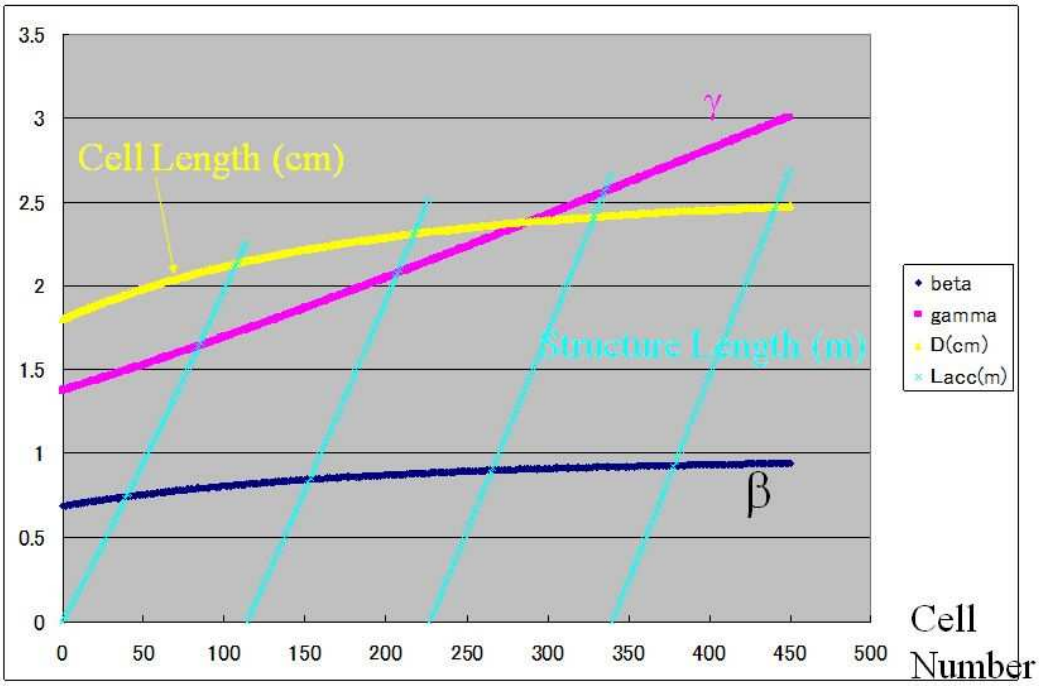

FIG. 32: Cell length corresponding to the muon velocity.

The total system based on this desgin of the high β linac is shown in Fig. 33. One 50 MW class klystron can drive four accelerating structures to accelerate muons from 100 MeV/c to 300 MeV/c.

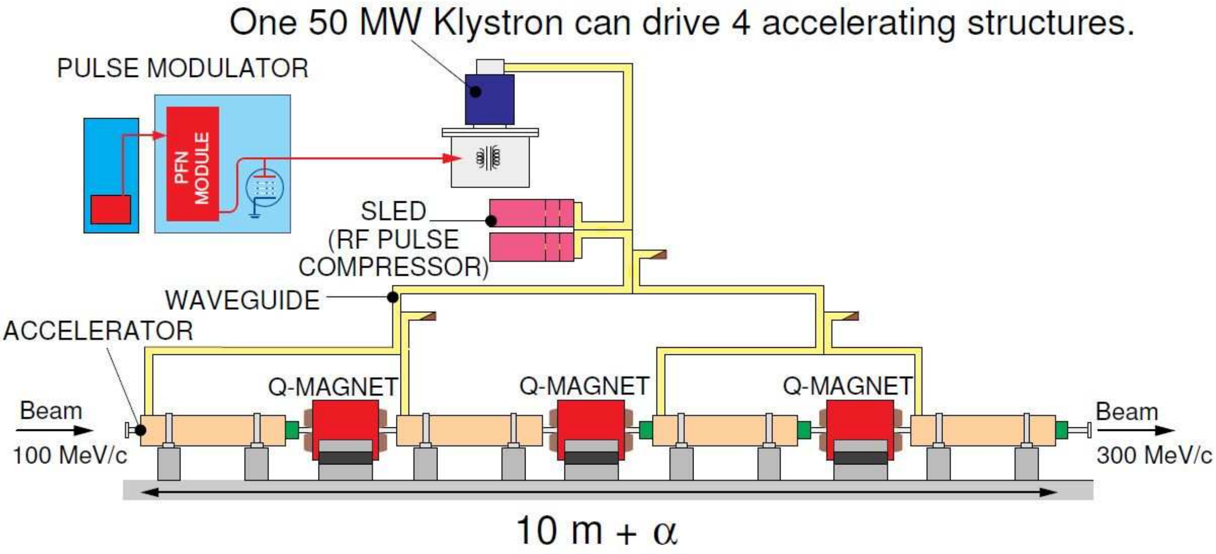

FIG. 33: Schematic diagram of the high β sectino of the muon re-acceleration.

The muons from the end of the low–β section are tracked through these accelerating structures generated for the center RF phase of 80 degree.

Figure 34 is the longitudinal distribution at the end of the high–β section.

As a result, the 98% of muons are passed in the accelerating phase.

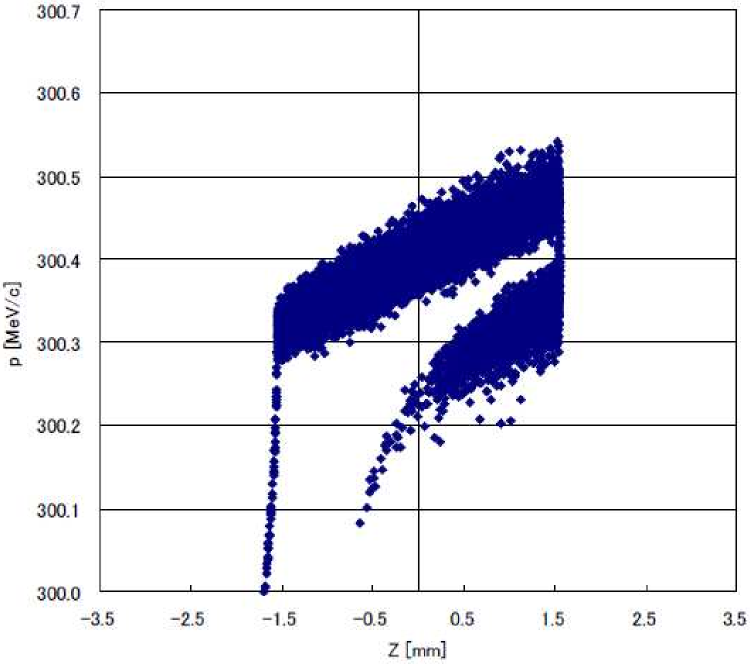

FIG. 34: Longitidinal distribution of the muon at the exit of the high–β Linac.

VI. MUON STORAGE RING MAGNET AND INJECTION

The muon storage ring for this experiment will be a precession field 3 Tesla solenoid with cylindrical iron poles and return yoke. The solenoid is being designed now in collaboration with a private company to a specification of a < 1 ppm variation of the field locally within the storage region. The storage region is defined on the mid-plane, with a radius of 33.3 ± 5.0 cm and height of ±10 cm. An engineering study is shown in Fig. 35. Note that the coils are located at 80 cm radius.

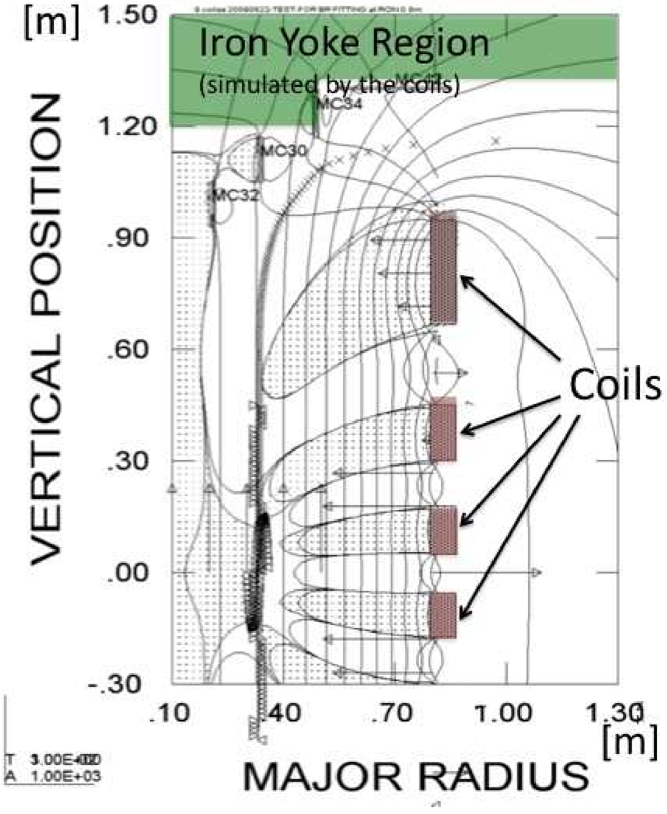

FIG. 35: An example of engineering studies by a private company.

A. Injection

For injection, the muon beam must be injected into the storage ring with minimum interference to the storage field. In the BNL $g-2$ experiment, as displayed in Fig. 37, a device called an inflector was used to inject the muon beam, to avoid deflection by the fringe field. As the beam crossed the storage region, the beam was kicked horizontally by the kicker to move to the central orbit through an angle large enough to prevent the beam from striking the inflector after one turn. This procedure works only if the radius of storage ring is large enough compared to the inflector wall thickness. The limitation comes from the required kick-angle within the first turn in the storage ring (within 149.2 ns) to avoid hitting the inflector itself. In the BNL $g-2$ experiment, the radius of storage ring was 711 cm and the wall thickness was ~ 1 cm. Therefore the kick angle was ~ 1.5 mrad.

In our experiment, the radius of the center beam orbit is 33.3 cm. This corresponds to a required horizontal kick angle of 30 mrad within the first turn in the ring (within 7.4 ns). The kick angle would be an order of magnitude larger than the kick with any existing technology. The horizontal kick does not work for our case.

Therefore, we have chosen a **spiral injection scheme** instead as displayed in Fig. 38. A solenoidal magnet is suitable for this injection scheme. An unique point of this scheme is to build in a radial fringe field to replace the role of the inflector. The beam will enter the solenoid through a hole in the iron return yoke iron. (Note that the BNL E821 used a similar hole in the iron return yoke, which was easily compensated for by adding additional iron beside the hole.) The definition of pitch angle θ here is the angle between the muon momentum and horizontal plane (the $x-z$ plane) perpendicular to the solenoid axis (the y-axis),

$$\theta = \sin^{-1} \frac{V_y}{\sqrt{V_x^2 + V_z^2}}, \tag{16}$$

and shown in Fig. 36.

In this way, the beam will be separated from the injecting point by $\sim$10 cm *vertically*, so there would not be no disturbance for the beam trajectory.

The beam momentum is deflected to vertically by a radial magnetic field, which will be built in the solenoid fringe field, which is shown as B_R in Fig. 38. The magnetic field should be carefully shimmed not only for the vertical field for the muon storage but also for the radial field so that only small vertical momentum remains when the spiraling beam reaches the beginning of the storage region.

The injected beam will then spiral through the good field (B_R) storage region and a magnetic kicker will be used to deflect the beam into a stable orbit at the center of the storage region. The duration of the kick can be for a number of cyclotron (or revolution) periods, since a longer kicker pulse allows a low kicker voltage and more stability. Multi-

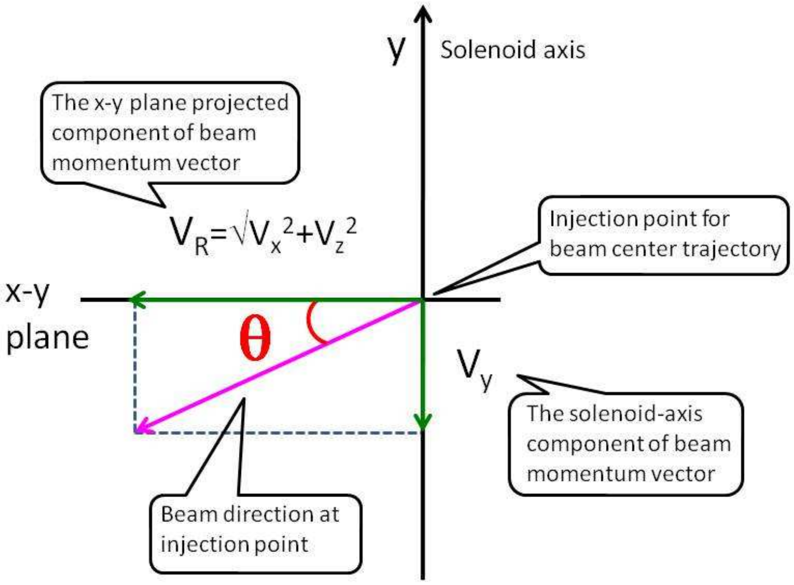

FIG. 36: A definition of θ is shown.

turn-kick by the longer pulse shape kicker would be easier.

B. Field configuration and muon trajectory

Figure 39 introduces the magnet configuration planned for the storage ring. Note that we will discuss the muon injection scheme in a conceptually designed magnetic field in this section. More practical design is in progress collaborating with a private company. The upper picture depicts a solenoidal conductor (pink), with one-eighth of the iron pole tip (green) and iron return yoke (black). The bottom picture depicts calculated muon beam injection trajectory with this magnet configuration together with one-eighth of the iron pole tip and iron return yoke.

Figure 40 displays the vertical (along the solenoid axis) and radial components of the magnetic field (B_y and B_R) *along the muon beam trajectory*, which is introduced in Fig. 39 (bottom). Blue dotted vertical line corresponds to $y = y_0 = 104.6$ cm. Initial vertical injection point for a *beam center* trajectory. Note that the magnetic field changes smoothly as the muon moves. This is an important point to find stable trajectory.

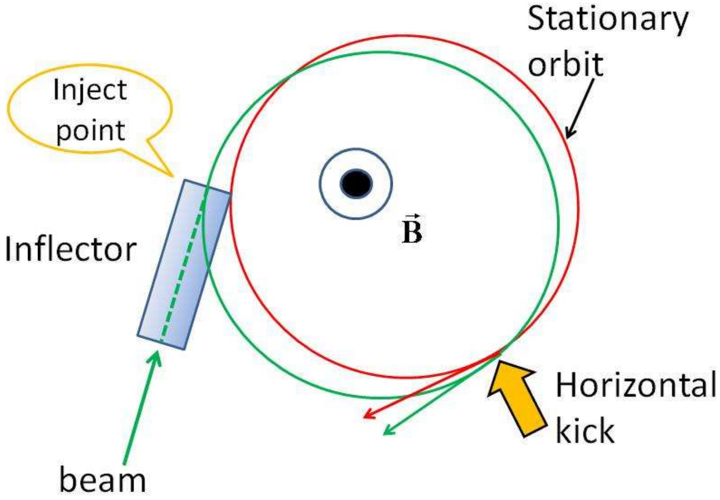

FIG. 37: Injection scheme for previous experiment (BNL $g-2$) from top view. They have inflector and horizontal kicker system.

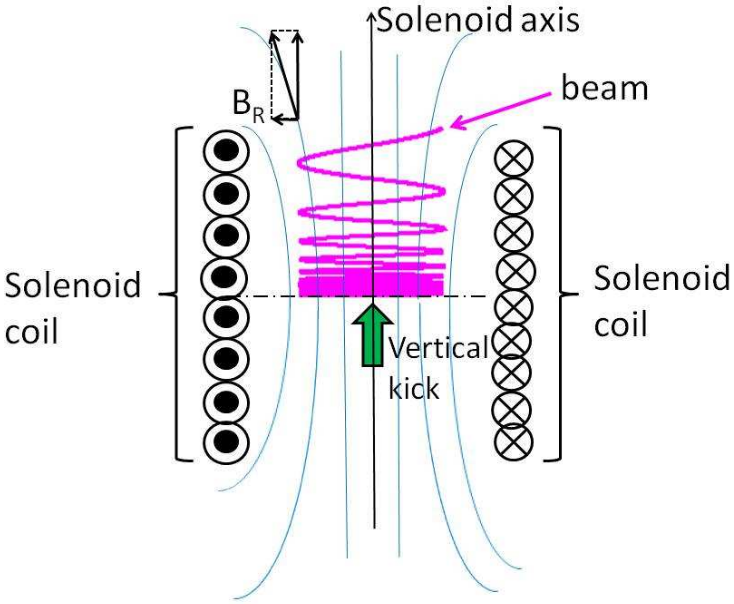

FIG. 38: Schematic representation of spiral injection for our case. A radial fringe field, shown as B_R, deflects the vertical component of the beam momentum to the horizontal component.

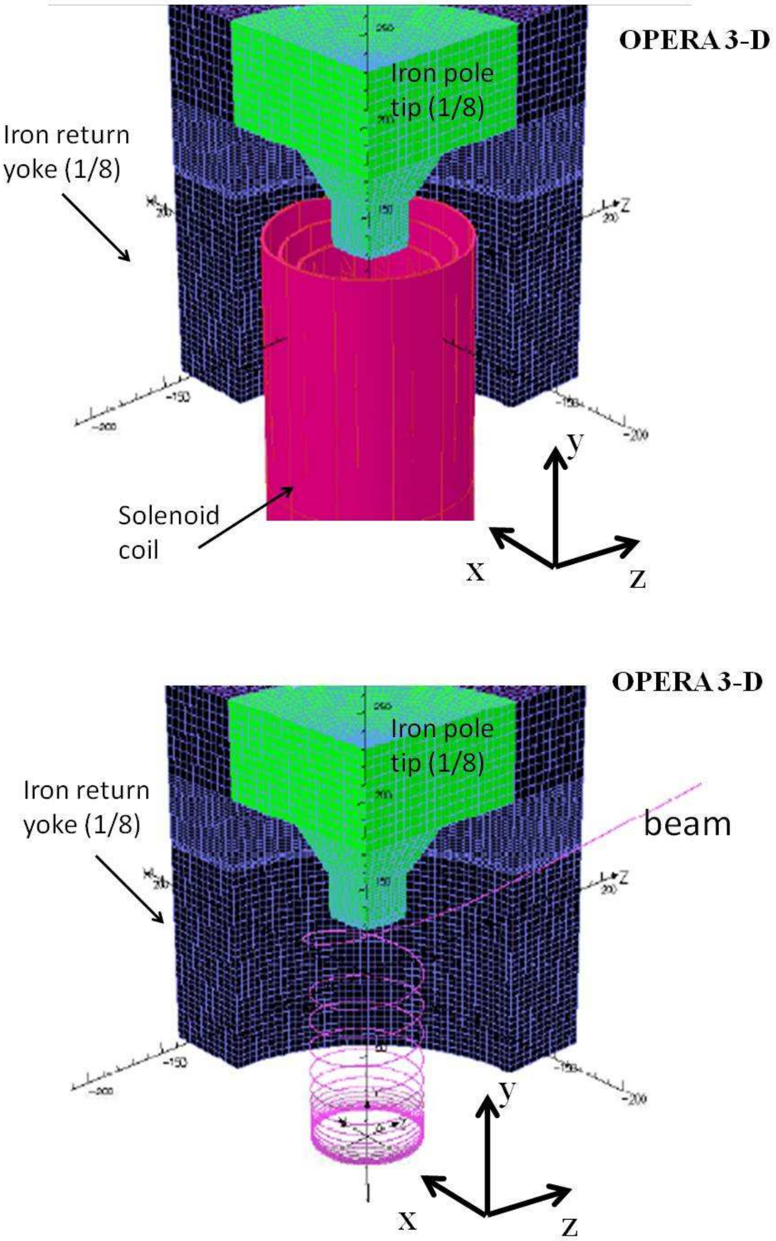

FIG. 39: Top: A conceptual illustration of the storage ring magnet: solenoid coils, one-eighth of iron pole tip and return yoke. Bottom: Calculated spiral trajectory of a single muon particle with $\gamma_\mu = 3$ by Opera.

Since the magnetic field is symmetric at a given radial position ($R = \sqrt{x^2 + z^2}$) and does not change dramatically even in the fringe field region, optical parameters of the muon beam for a stable injection can be obtained. To determine the optimal correlation between

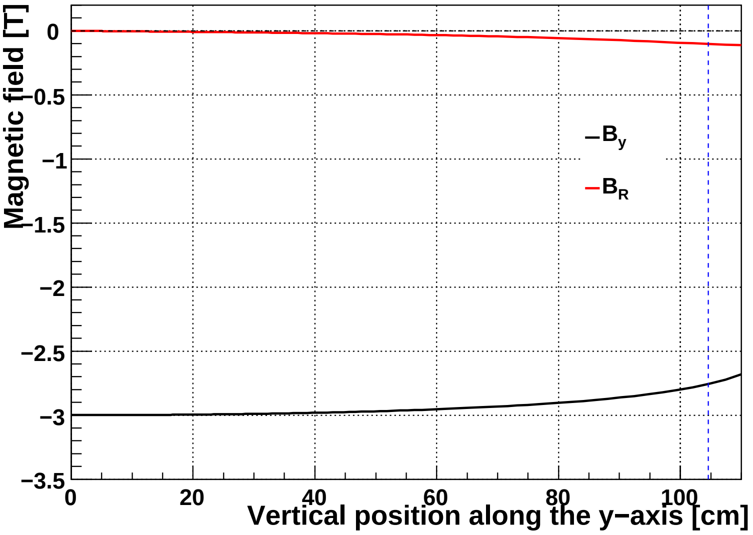

FIG. 40: Magnetic field *along the muon beam trajectory* as function of vertical axis (solenoid axis). The trajectory is introduced in Fig. 39 (bottom). Note that the magnetic field changes smoothly as the muon moves. Blue dotted vertical line corresponds to $y = y_0 = 104.6$ cm.

vertical position displacement (Δy) and duration of pitch angle ($\Delta\theta$), we calculate several thousands of beam trajectories with random distribution of Δy and $\Delta\theta$ by OPERA. We set *beam center* as a solid pink line in Fig 39 (bottom), and set a proper injection point on this trajectory : $R_0 = \sqrt{x_0^2 + z_0^2} = 34.6$ cm, $y_0 = 104.6$ cm, with a pitch angle of $\theta = 23.4°$. A definition of pitch angle θ is previously shown in Fig. 36.

Then we tried several thousands of trajectories in a proper area of $(\Delta y, \Delta\theta)$ as shown in black points in Fig. 41. Parameters for *beam center* trajectory is at $(\Delta y, \Delta\theta) = (0, 0)$. Parameters of successful injections are shown in green.

Here, ΔY and $\Delta\phi_y$ are written as:

$$\Delta y = y - y_0 \text{ in cm},$$
$$\Delta\theta = \frac{V_y - V_{y0}}{V_{y0}} \text{ in rad.} \tag{17}$$

Figure 43 displays several example trajectories shown in green points in Fig. 41, together with a *beam center* trajectory. Fringe field acts as *local focus* for a proper set of beam injection conditions as shown in Fig. 41.

More practical design as displayed in Fig. 35 is in progress collaborating with a private company.

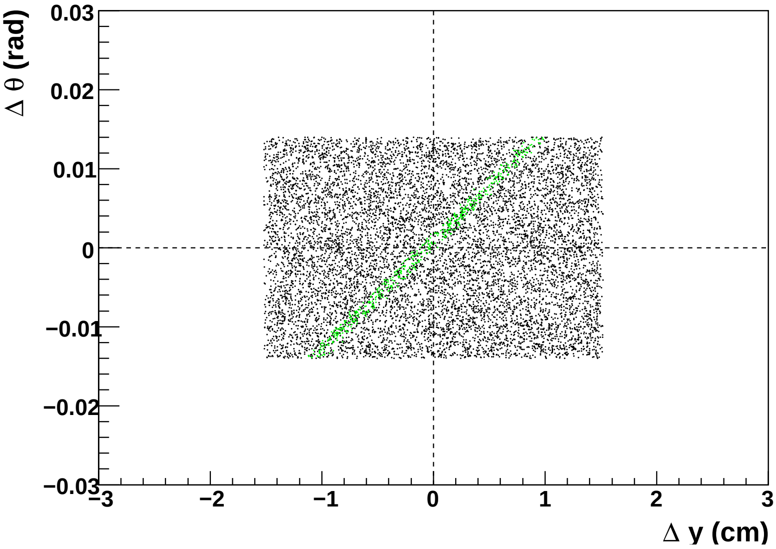

FIG. 41: Input parameters of $(\Delta y, \Delta\theta)$ with regards to initial point of *beam center* trajectory. (Parameters for *beam center* trajectory is at $(\Delta y, \Delta\theta) = (0, 0)$.) Parameters of successful injections are shown in green. Examples of successful injection and trajectory are shown in Fig. 43. Correlation between Δy and $\Delta\theta$ suggest the fringe field provides local focusing effect as discussed in Fig. 42.

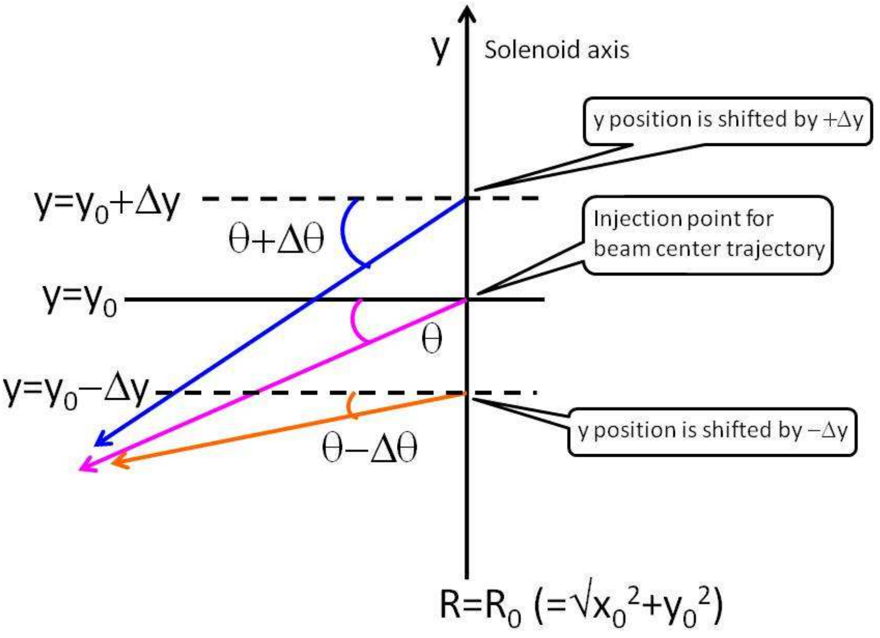

FIG. 42: A cartoon to help an intuitive understanding of a correlating between Δy and $\Delta\theta$.

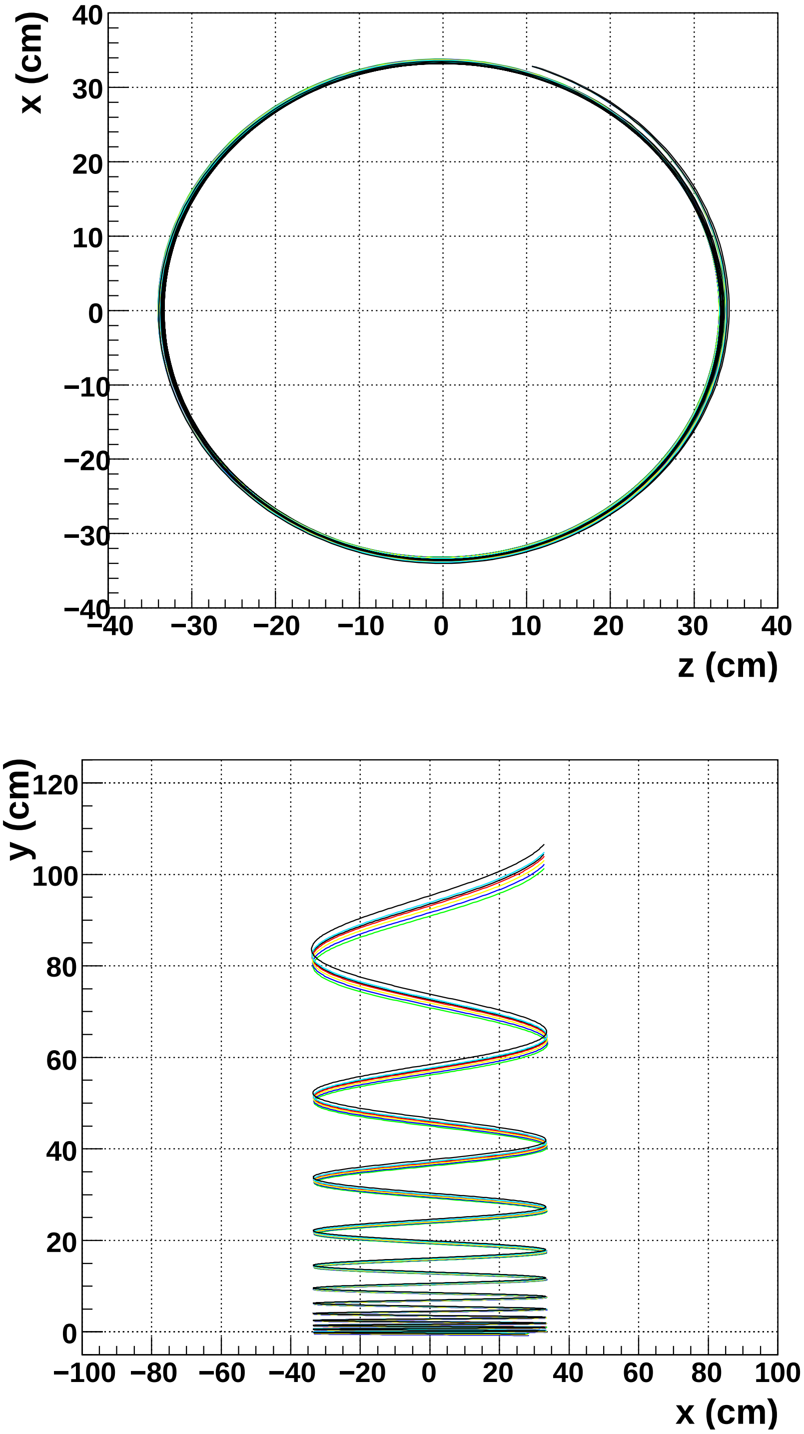

FIG. 43: Samples of possible muon beam trajectories in the acceptable acceptance for the kicker and the storage ring.

C. Kicker

The role of the kicker is to move the muon beam onto a stable orbit. In our case, the muon beam will be guided to the good field region by the solenoidal field only which includes a small radial field above the good field region, reducing the pitch angle of the incoming beam to zero degree. The pitch angle of the beam in the good field region is planned to be the order of a few mrad. Therefore the required vertical kick is a few mrad, which is acceptable strength. We plan to apply the kick for several cyclotron periods along the orbit. This allows us to apply a lower kicker voltage without strict jitter requirements, and with better stability.

Figure 44 depicts one of candidate of kicker set-up in the storage ring: Anti-Helmholtz coil system coil system, shown in red four loops. Figure 45 depicts a zoom on the cross-section of a kicker system. Pairs of coils above and below the storage region have different radii and are separated 6 cm vertically. The upper and lower coils are separated by 24 cm and do not interfere with the storage and detector volumes.

The current direction of the pair of upper coils and the pair of lower coils are the same, but the current is opposite between upper and lower coils. Such a coil system generates mainly a radial field remains around the region of $|y| < 10$ cm as shown in Fig. 45. This radial field is cylindrically symmetric in the radial direction and applies a vertical kick to the muon beam.

Figure 46 displays an example electrical circuit to drive the kicker coils. In this case, the system can apply a 3.5 mrad kick vertically with a half-sine shaped pulse with a 150 ns (20 cyclotron periods).

$$B_{kick}(t) = B_{peak} \cdot \sin(\omega t), \tag{18}$$

here,

$$\begin{aligned} B_{peak} &= 1.3 \times 10^{-4} \text{ T}, \\ \omega &= \frac{\pi}{T_{kick}}, \\ T_{kick} &= 150 \text{ ns}. \end{aligned}$$

The simulated current shape as a function of time is displayed in the lower plot in Fig. 47. During 150 ns, the vertical drift length of the muon beam is about 7 cm.

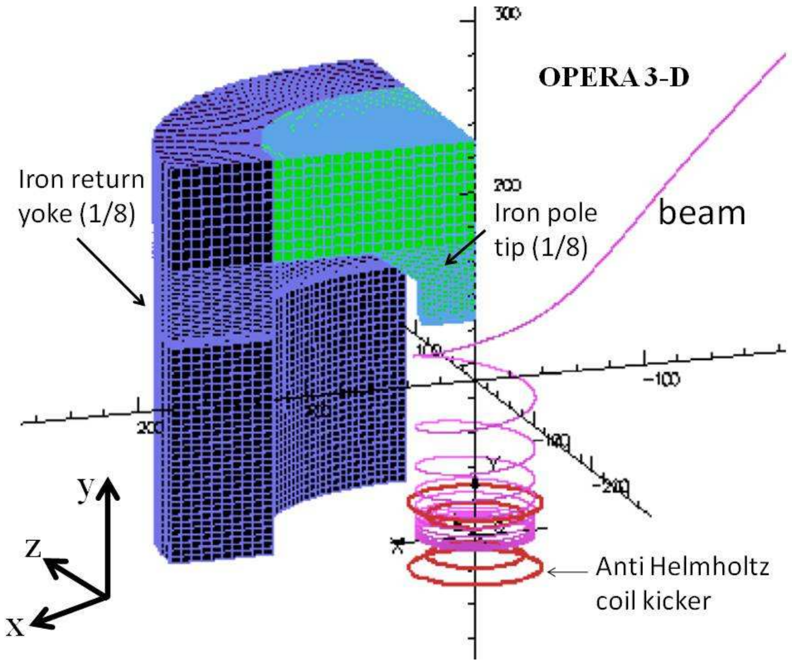

FIG. 44: A kicker system (Anti-Helmholtz coil system) is shown in red lines, in the storage ring magnet. To give an idea of its size, the expected muon beam trajectory, iron pole tip and return yoke are also shown.(Solenoid coil is not shown.)

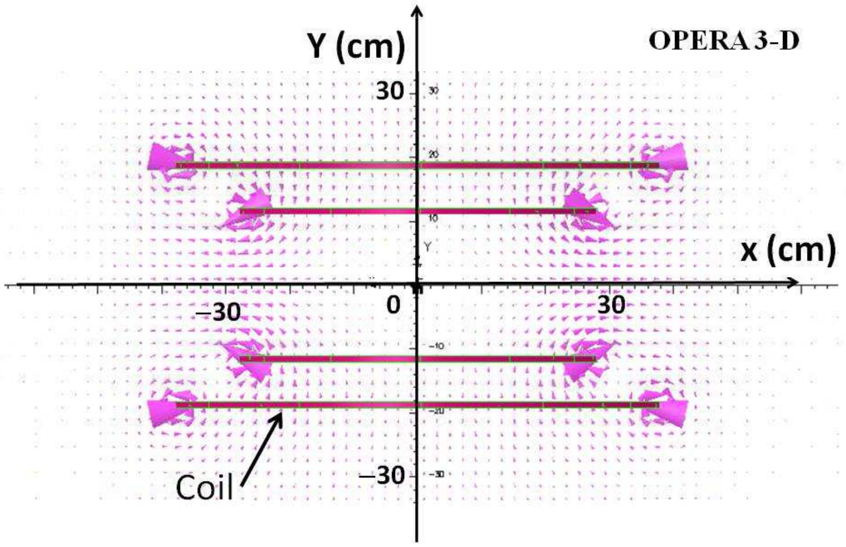

FIG. 45: Cross-section view of the kicker system (zoom up). Pink triangles depicts direction of the magnetic field.

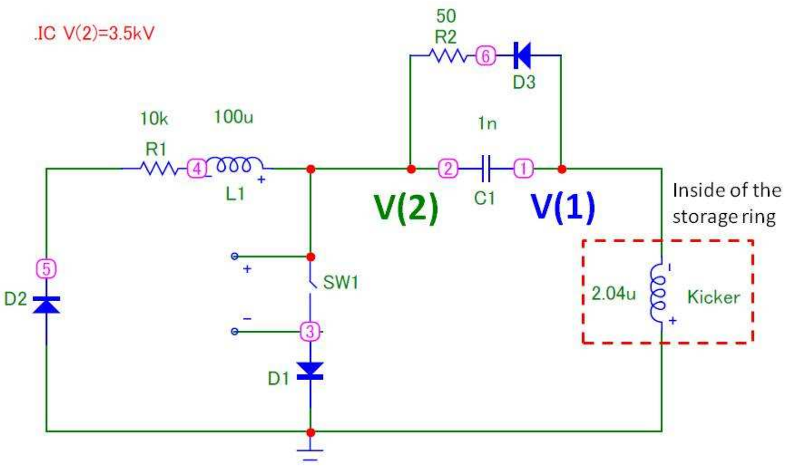

FIG. 46: Example circuit for the kicker. The airs of two ring coil system the storage ring is indicated as the red dotted box.

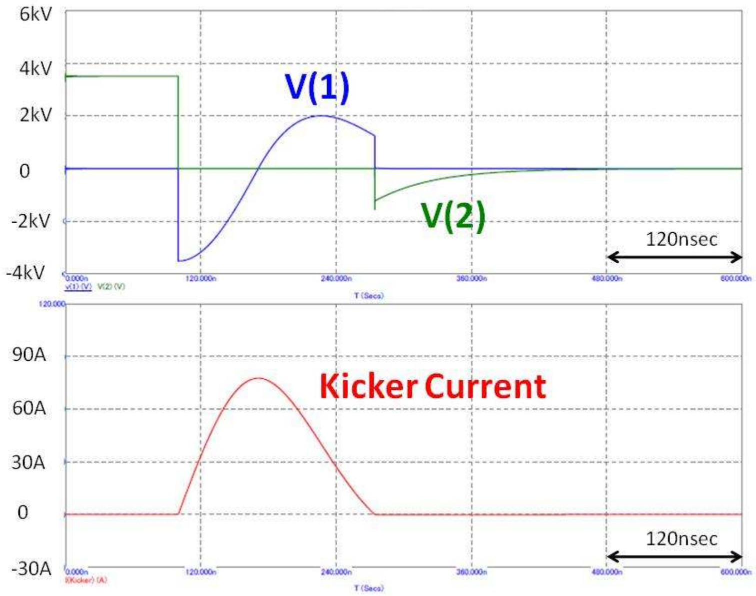

FIG. 47: Top: Voltage as function of time. V(1) and V(2) correspond pickup points in the circuit, Fig. 46. Bottom: Kicker current as function of time. Half-sin shape can be seen as introduced in Equation 18.

Major issues for kicker are the following;

- Kicker field flatness as function of radial position,
- Residual voltage in the circuit may cause the electric field in the space,
- The eddy current in the cryostat wall will be generated.

We are studying to determine the best configuration for the coils and expect to achieve sufficient field flatness. For eddy currents, this causes an *error field* and needs to be considered carefully. In the current example circuit, the residual voltage V(2) in Fig. 47 remains for $\sim$ 100 ns after the kicker-pulse. We need to estimate the magnitude of this effect on the magnetic field.

D. Possible error fields

Possible sources of error magnetic field are the following

1. Mechanical disturbances

- Static structural error

  Although the coil can be designed such that the field quality in the storage area is in the 10^{-7} field quality, the construction error can cause the error field. In order to achieve field quality of 10^{-7} the construction error must be the order of 10^{-6} m that is far beyond the achievable construction precision. The precision of 10^{-3} m is the reasonable specification for the 1 m big solenoid. The iron return yoke should have same order of the influences. This indicates that achievable field quality with the main coil is the order 10^{-4} T range. The structural error can be expressed by radial or longitudinal deformation modes that have angular spectrum of $d = k_{cm}\cos(m\phi)$ (or $k_{sm}\sin(m\phi)$) as shown Fig. 48, where k_{xm} is the deformation amplitude, and n is the mode index. Influences to the beam area from each mode differ from one more to another, generally smaller by ratio of $(a/r)^m$ where a is the radius of beam area, r is the radius of the solenoid, and m is the deformation mode index. The deformation mode and its influence to the field should be simulated to evaluate the necessary corrector scheme. Field compensation using magnetic shims may be used for the initial optimization. The magnet structure is such that the access to the coil area is limited and that correction using magnetic shim may not be the final tuning. An appropriate corrector coil scheme must be designed and implemented properly. The corrector coils may be operated by external power supplies. The current stability of the corrector should be better than 10^{-4}.

- Structural error by temperature change

  The thermal contraction ratio of iron is about 10^{-5}/K. In order to achieve 10^{-6} m accuracy shown above, the temperature must be controlled by the order of ±0.1 K. The iron yoke must be encased in the shield room with the very precise temperature control, i.e. ±0.1 K.

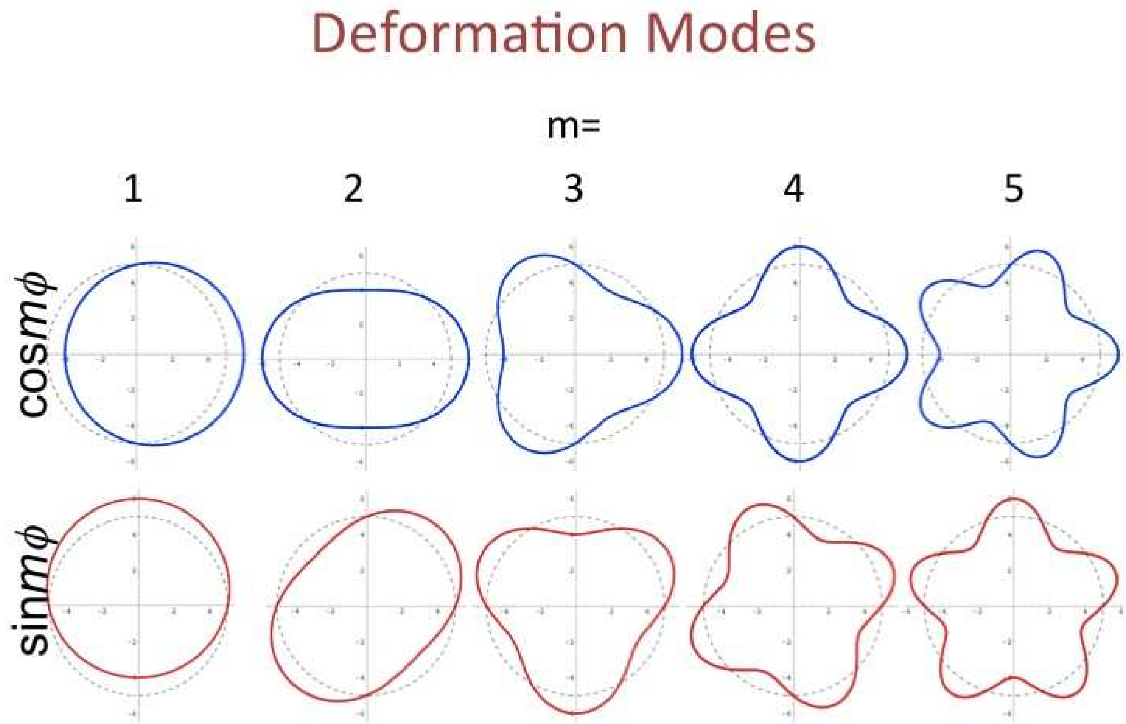

FIG. 48: The structural errors expressed by radial or longitudinal deformation modes.

- Mechanical vibration

  The mechanical vibration is also a big concern for the field error. The seismic vibration measured at KEK Tsukuba (Fig. 49) shows the value exceeding 10^{-6} m. The seismic vibration at the experiment site should be performed and proper vibration dumping system should be designed to avoid magnet system mechanical vibration.

2. *Electromagnetic disturbances*

- Magnetic materials

  Although the system maybe designed to avoid to any uncontrollable magnetic materials, some materials such as welded stainless steels maybe inevitable. One must confirm that those should not produce an error field exceeding the field range correctable by the corrector coils. The magnetic material close to the beam area may cause the error

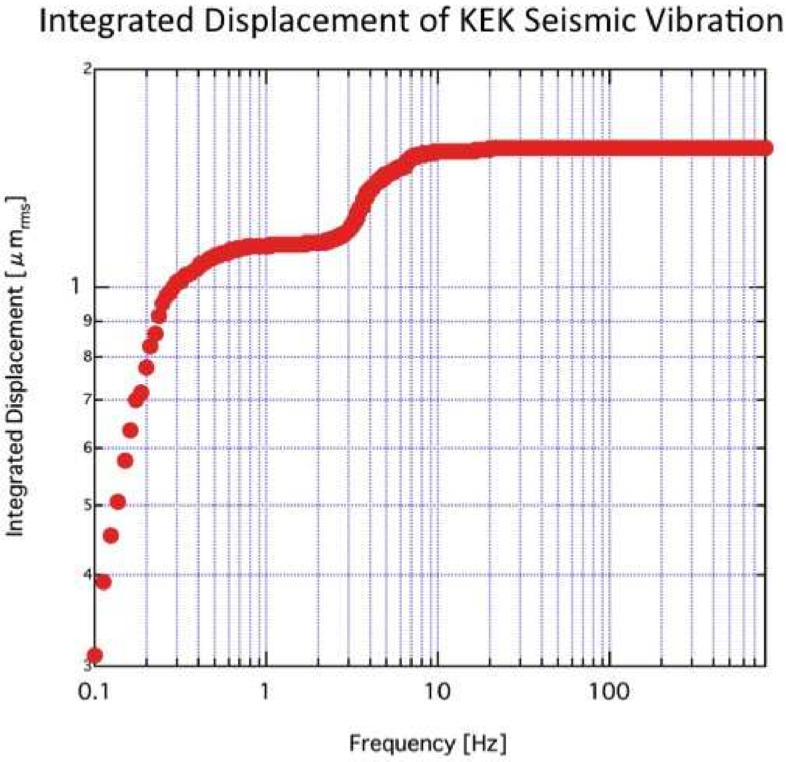

FIG. 49: The seismic vibration measured at KEK Tsukuba.

field corresponds to the error field introduced by higher order deformation index n, that may not be corrected by the corrector coils. One should design the system very carefully to avoid magnetic materials close to the beam area.

- Superconductor

a. Magnetization The magnetization of superconductor, which is an inherent property of type III superconductor, is another big concern. The average magnetization of the superconducting wire can be expressed as $M = 4/3\mu_0 J_c ak/\pi$, where M is the magnetization, μ_0 is the permeability of the vacuum, J_c is the current critical current density, which is the function of the local magnetic field and temperature, a is the diameter of superconducting filaments, and k is the volumetric ratio of superconducting filaments in the wire. In general J_c can be as large as the order 10^9 A/m^2, a is an order of 10^{-5} m, and k is about the order of 0.1. The magnetization can be estimated as an order 10^{-4} T. The influence to the beam area may be further reduced and can be corrected by corrector coils if the error is stable. The issue is that the magnetization can be changed due to the flux creep effect. The flux creep is the movement of the pinned flux vortex in the superconductor that generally introduced by statistical thermal excitation of the vortex. The effect decreases the magnetization by a logarithmic function. A sufficient idle time after magnet excitation may reduce the influences, however the idle time can be too long to achieve 10^{-7} stability with a reasonable experiment efficiency. Another way to reduce influence is to reduce temperature after magnet excitation. The procedure, however, must be done after all the field optimization is made. The magnet excitation and field optimization procedure should be well studied to achieve 10^{-7} field accuracy and stability.

b. Strand coupling current The strand coupling current is the coupling current between the superconducting filaments. The influences are generally very small and the time constants are in the range of 10–100 ms. The reasonable idle time after magnet excitation should avoid the problem.

c. Cable coupling current (if cable is used) In case the cable is used, the coupling current between the cable strands can cause a various kinds of error fields and those can be 10^{-4} T level. The coupling current also includes the various time constants that can vary from the order of 10 ms to hours. It also causes the change in local field in the coil that affects the superconductor magnetization. Those are very complicated and almost uncontrollable to achieve 10^{-7} field quality. One should avoid using a cable for the magnet coil. The coil should be wound from a wire.

d. Persistent current operation Time constants are generally very large and should not be a problem. There are some coupling with above three effects, however after a reasonable idle time after magnet excitation all the effects should be stable such that operation current change become stable.

E. Field measurement and its absolute calibration

1. Measurement methods for the experiment

There are many methods of measuring magnetic field: Hall probe, flux measurements with pick up coils, nuclear magnetic resonance (NMR), and so on. The optimal choice depends on the nature of the field to be measured; AC or DC field, gradient or absolute field, etc.

In this experiment, a superconducting solenoid having a high uniformity of the central field is adopted for the muon storage magnet. From the field measurement view point, the measurement region around the solenoid could be divided into two regions, that is, the beam injection region and the beam storage region. (We also need to measure/control the tracking region with moderate precession.)

The beam injection region is the region from the end of the injection beam line to the beam storage region around the solenoid center, and it includes a stray field region outside the solenoid. The muon beam passes through the beam injection region only one time, therefore,the tolerance of the magnetic field error is much larger than that in the beam storage region. It is enough to measure the magnetic field in the beam injection region with an accuracy of 100 ppm.

There are two field measurement methods satisfying that accuracy; the Hall probe method and the flux measurement method. Although an NMR method also meets the required accuracy, below 10 ppm, such a very high accuracy can be reached only in a stable and homogeneous field, generally 1%/s and 0.1%/cm, so it is not suitable for a field measurement in a high gradient field like a stray fringe field. Table XI summarizes the advantages and disadvantages of the Hall probe and flux measurement methods. It is necessary to consider the cryostat and support structure as well as the accuracy, further design study is required.

From the beam optics study, the beam storage region should be cylindrical shape with an inner diameter of about 280 mm, a outer diameter of 380 mm and a height of 400 mm (no interference with the kicker coils), and the region must have high field homogeneity at a ppm level locally, and be measured along the muon storage orbit (integrated) to < 0.1 ppm, with a central field of 3 T. The NMR method is the only solution for measuring with this precession.

It is not easy to measure this magnetic field at a sub-ppm level, since there are no magnets with such a high homogeneity at 3 T which can be used to fine-tune the NMR system. So, the adjustment of the NMR system at a sub-ppm level of accuracy is planned to progress in parallel with the development of the superconducting solenoid for muon storage.

TABLE XI: Summary of advantages and disadvantages of the Hall probe and flux measurement.

Method	Advantage	Disadvantage
Hall probe	Simple	Non-linear output
	Inexpensive	Sensitive to temperature
	Commercially available	Long term drift
	Fast measurement	Need to compensate Planar Hall effect
	Small probe size	
Flux measurement	Simple	Need change in flux
	Passive device	Need calibration of geometry
	Linear output	Need integrator device
	Drift-free device	

This strategy has two steps of development of the NMR measurement system. In the first step, a commercial NMR system with an accuracy of 1 ppm will be purchased for a rough evaluation of the solenoid field at the initial R&D phase. Based on the measurement results, the solenoid field would be regulated to reach a field homogeneity of 1 ppm in the beam storage region.

In the second step, an NMR system which can reach a sub-ppm level precision will be purchased, and would be fine-tuned using the solenoid in collaboration with the company making the NMR system.

In both steps, a probe positioning system made of nonmagnetic materials should be developed, which can control the probe position in the solenoid in the cylindrical coordinate system. The precision of 1 mm should be sufficient for the position control, since the size of the probe would be 5 mm in diameter. That precision could be easily achievable with commercial devices, however, materials composing the positioning system should be carefully selected. It should be placed near the solenoid so that a limited space around the solenoid could be made effective use, and the accuracy of the position control could be easily improved.

In the first step of the development of the NMR measurement system, a field distribution measurement in a 3 T solenoid is planned using an NMR system with 1 ppm accuracy. The objectives of the measurement are to fine-tune the NMR system and to build the prototype of positioning system.

Arrangements to use a 3 T solenoid are successfully progressing with the National Institute of Radiological Sciences at Chiba city. The solenoid is designed for MRI medical applications, and placed horizontally, which is different from the solenoid for the $g-2$ experiment, which will be placed vertically. However, this MRI magnet will be useful to check whether the components of the positioning system work in a high magnetic field and provide a high accuracy field measurement. Figure 50 shows the overview of the field measurement system for the horizontal solenoid. Design work is in progress.

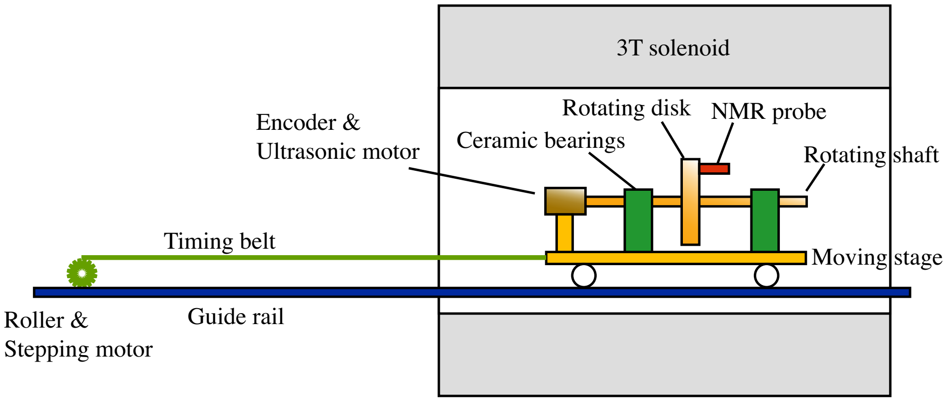

FIG. 50: Overview of the positioning system for the field distribution measurement in the MRI solenoid at NIRS.

F. Cryogenic system

A conceptual design proposal of the storage ring cryogenic system is shown in Fig. 51. The requirements to the cryogenics from the view point of good field quality of the solenoid are 1) sub-micron mechanical stability, 2) good temperature controllability and stability of superconducting coil. There are also additional requirements to the room temperature system to avoid mechanical vibration to the magnet system. The temperature controllability of room temperature iron yoke should be guarantee the temperature stability of ±0.1 K. Since the superconducting solenoid will be made from the wire and operated with a relatively low current, the system may be cooled with several cryo-coolers. The cooling of the coil, however, should be made by liquid helium to ensure the good temperature stability. The temperature control can be made with a pressure control of the helium vessel. The precise pressure control system should be implemented. The cryo-coolers are used for recondensation of helium. Number of corrector coils as well as their operation current may affect to the cryogenics heat load. They should be optimized such that the system can be achieved with cryo-coolers. Since the vibration of the system may cause the devastating effect to the field quality vibration dumpers should be carefully implemented to achieve vibration level below 0.1 micron for the solenoid system. The study now being performed for the ILCIRQ (International Linear Collider Interaction Region Quadropole magnet) aiming for the 10 nm level stability and their R&D results may be used for this system as well. Although this is not a part of cryogenics the biggest challenge for the system is the control of the iron yoke temperature. The temperature stability and uniformity of ±0.1 K is currently required with a preliminary design study. The room temperature shield room design must be performed very carefully to achieve this limit.

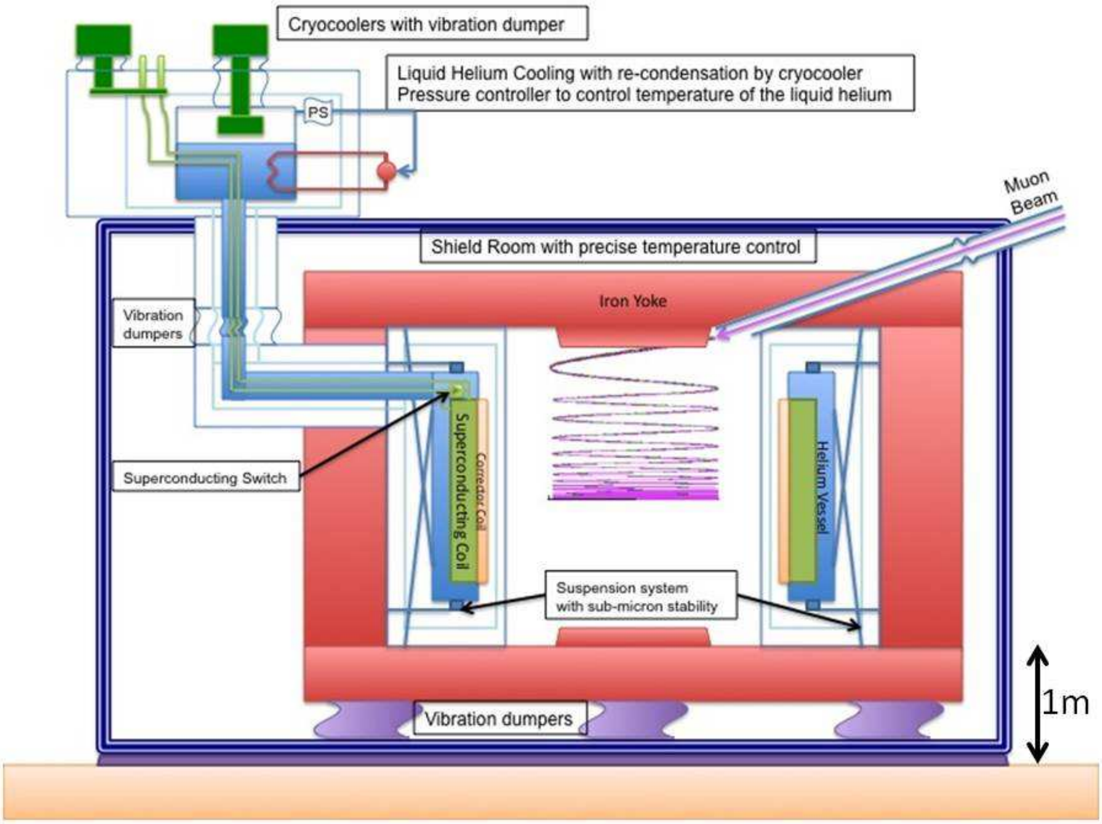

FIG. 51: A conceptual design proposal of the storage ring cryogenic system.

VII. MEASUREMENT OF ω_a

A. Spin-dependent decay from the $V{-}A$ theory

We begin this section by introducing the spin-dependent μ decay and its analyzing power. The positive muon decays into a positron, a neutrino and anti-neutrino; $\mu^+ \rightarrow e^+ + \bar{\nu_\mu} + \nu_e$. Parity non-conservation in the weak decay and helicity conservation lead to an asymmetry in the angular distribution of the decay positrons with respect to the direction of the μ-spin (θ_S). Viewing the decay in the muon rest frame, the decay e^+ has its maximum momentum and is 100% polarized when the $\bar{\nu_\mu}$ and ν_e are emitted to the opposite direction of the e^+, as shown in Fig. 52. Here, e^+ and $\bar{\nu_\mu}$ are right-handed, ν_e is left-handed. The maximum value of the positron momentum is approximately half of the mass of μ; $(p_e^*)_{max} = m_\mu/2 = 53\ \mathrm{MeV}/c$. We write for the decay electron momentum relative to its maximum,

$$\eta = \frac{p_e^*}{(p_e^*)_{max}}. \tag{19}$$

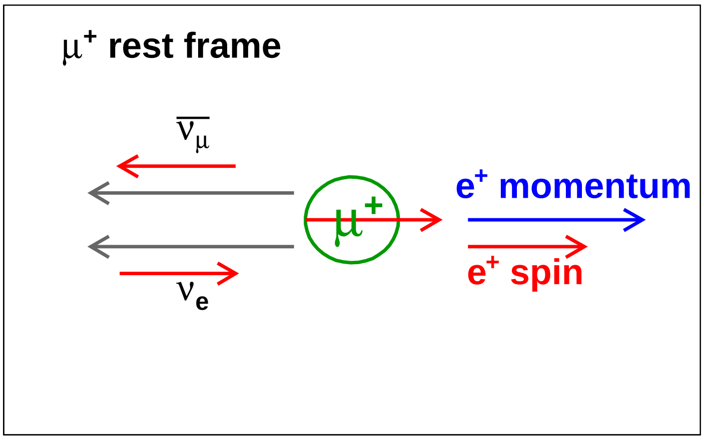

FIG. 52: Viewing the decay in the muon rest frame, the decay e^+ (right-handed) has its maximum momentum and polarization when $\bar{\nu_\mu}$ (right-handed) and ν_e (left-handed) are emitted to the opposite direction to the direction of e^+.

The probability for a positron, whose momentum range is $\eta \rightarrow \eta + d\eta$, to be emitted into a solid angle $\mathrm{d}\Omega$ at an angle θ_S is given by the $V{-}A$ theory[63, 64];

$$\begin{aligned}
\mathrm{d}\mathcal{M}(\eta,\theta_S) &= n(\eta)[1+a(\eta)P_\mu\cos\theta_S]\mathrm{d}\eta\mathrm{d}\Omega, \\
n(\eta) &= 2\eta^2(3-2\eta), \\
a(\eta) &= \frac{2\eta-1}{3-2\eta}. \qquad (20)
\end{aligned}$$

θ_S is the angle between $\vec{S}$ and $\hat{p_{e^+}}$ and P_μ is the polarization of the muon.

A two-dimensional plot of $\mathrm{d}\mathcal{M}(\eta,\theta_S)$ is displayed in the top plot in Fig. 53. $n(\eta)$ and $a(\eta)$ are displayed in the bottom plot in Fig. 53.

The decay event introduced in Fig. 52 corresponds to the right top point in Fig. 53 ($\cos\theta_S = 1$ and $\eta = 1$).

B. $g-2$ precession in the magnetic field

In the presence of a static magnetic field, $\vec{B} = (0,0,B)$, the muon moves on the plane perpendicular to $\vec{B}$. Here, we assume that both the electric field and the electric dipole moment are zero.

The cyclotron frequency $\vec{\omega}_c$ and spin frequency $\vec{\omega}_S$ are expressed as

$$\begin{aligned}
\vec{\omega}_c &= -\frac{q\vec{B}}{m_\mu\gamma_\mu}, \\
\vec{\omega}_S &= -\frac{gq\vec{B}}{2m_\mu} - (1-\gamma_\mu)\frac{q\vec{B}}{m_\mu\gamma_\mu}. \qquad (21)
\end{aligned}$$

The anomalous precession frequency $\vec{\omega}_a$ is determined from the difference:

$$\vec{\omega_a} = \vec{\omega_S} - \vec{\omega_c} = -\frac{q\vec{B}}{m_\mu}\left(\frac{g-2}{2}\right). \qquad (22)$$

For example we input $\gamma_\mu = 3$ ($p_\mu = 300$ MeV$/c$) and $\mid \vec{B} \mid = 3$ T, we obtain cyclotron period $T_c = 2\pi\omega_c = 7.41$ ns and anomalous period $2\pi\omega_a = 2111.7$ ns.

The μ-decay is described in the muon rest frame, where the μ-spin ($\vec{S_\mu}$) rotates with the frequency of $\vec{\omega}_a$

$$\vec{S_\mu} = (\cos(\omega_a t),\ \sin(\omega_a t),\ 0). \qquad (23)$$

We introduce the definition of angles in the muon rest frame. Figure 54 (left) displays the system of the muon rest frame. The direction of the μ beam is along the x-axis, the

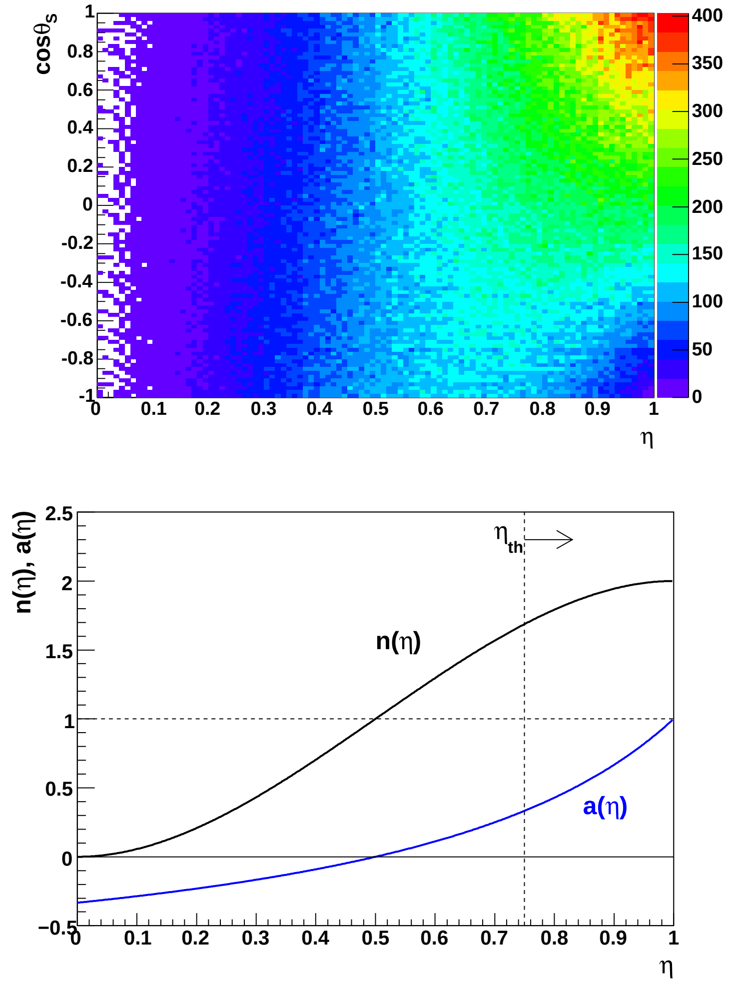

FIG. 53: Top: Probability of positron emission as a function of η and θ_S for $P_\mu = 1$. Decay positrons tend to be emitted to the muon spin direction ($\cos\theta_S \sim 1$) with their highest energy ($\eta \sim 1$). Interestingly, note that $\cos\theta_S$ distribution is flat at $\eta = 0.5$.
Bottom: Analyzing power $a(\eta)$ and event fraction $n(\eta)$ as functions of η, the positron energy fraction in the muon rest frame. η_{th} is the optimal threshold to measure the spin precession.

direction of the magnetic field is along the z-axis. The spin vector is displayed as red arrow and precesses as $\overrightarrow{S_\mu}$=($\cos(\omega_a t)$, $\sin(\omega_a t)$, 0) in the static magnetic field $\vec{B} = (0, 0, B)$.

In Fig. 54 (right), we adopt spherical polar coordinates (1, θ^*, ϕ^*) in the muon rest frame. The polar angle is θ^*. ϕ^* is zero when $\overrightarrow{p_e^*}$ is in the $x - y$ plane (the muon spin precession plane). The unit vector of the decay positron momentum is displayed as a blue arrow and is then expressed as

$$\overrightarrow{p_e^*}/|\overrightarrow{p_e^*}| = (\cos\theta^*, \sin\theta^*\cos\phi^*, \sin\theta^*\sin\phi^*). \tag{24}$$

θ_S is the angle between $\vec{S_\mu}$ and $\vec{P_e^*}/|\vec{P_e^*}|$. $\cos\theta_s$ is obtained as,

$$\begin{aligned}\cos\theta_S &= \vec{S_\mu}\cdot\frac{\vec{p_e^*}}{|\vec{p_e^*}|}\\ &= \sin\theta^*\cos\phi^*\sin(\omega_a t)+\cos\theta^*\cos(\omega_a t).\end{aligned} \tag{25}$$

Note that $\cos\theta_S$ behaves as a trigonometric function of $(\omega_a\ t)$. There are 4 types of decays we could detect; *forward*, *backward*, *left*, and *right* as displayed in Fig. 55.

Since $\vec{S_\mu}$ is rotating in the $x-y$ plane, the decay positron spectrum for any direction behaves as a trigonometric function of $(\omega_a t)$:

$$N_e(t) = N_0\cdot\exp\left(-\frac{t}{\gamma_\mu\tau}\right)\int\int n(\eta)\{1+a(\eta)P_\mu\cos\theta_S\}\mathrm{d}\eta\mathrm{d}\Omega. \tag{26}$$

Finally, the time spectra of four types of acceptance combinations for ϕ^* and $\cos\theta^*$ are listed in Table XII.

TABLE XII: $\int\cos\theta^*\mathrm{d}(\cos\theta^*)$ of several integral regions for *forward-decay.*

decay type	θ^*	ϕ^*
forward	$0\le\theta^*\le\pi/3$	$0\le\phi^*\le 2\pi$
backward	$2\pi/3\le\theta^*\le\pi$	$0\le\phi^*\le 2\pi$
left	$\pi/4\le\theta^*\le 3\pi/4$	$-\pi/3\le\phi^*\le\pi/3$
right	$\pi/4\le\theta^*\le 3\pi/4$	$2\pi/3\le\phi^*\le 4\pi/3$

In the case where we detect decay positrons which are emitted in the direction of the x-axis only, $\hat{p}_{e^+} = (1,0,0)$, θ_S is the angle between $\vec{S}$ and the x-axis (=direction of $\hat{p}_{e^+}$). Therefore, θ_S is simply written as

$$\theta_S = \omega_a t. \tag{27}$$

The time spectrum of decay positrons *in this case* is expressed as

$$N_e(t) = N_0\cdot\exp\left(-\frac{t}{\gamma_\mu\tau}\right)\int n(\eta)\{1+a(\eta)P_\mu\cos(\omega_a t)\}\mathrm{d}\eta. \tag{28}$$

In order to extract ω_a, we should detect positrons which have the highest asymmetry: $a(\eta) = 1$ at $\eta = 1$. However, we lose statistics of decay positrons if we are limited only within a narrow η-bin. We can determine an optimal threshold to measure ω_a shown as η_{th} in Fig. 53 (bottom). However, applying this threshold requires reconstructing the decay in the muon rest frame, which cannot be done due to an uncertainty in the positron momentum direction in the muon rest frame. We consider the decay, instead, in the laboratory frame.

C. Lorentz boost

The muon rest frame is rotating in the lab frame, as displayed in Fig. 56. Decay positrons in the Lab-frame are boosted as follows:

$$\begin{bmatrix} E_e \\ p_e \cos\theta \end{bmatrix} = \begin{bmatrix} \gamma_\mu & \gamma_\mu\beta_\mu \\ \gamma_\mu\beta_\mu & \gamma_\mu \end{bmatrix} \begin{bmatrix} E_e^* \\ p_e^* \cos\theta^* \end{bmatrix}, \tag{29}$$

and

$$p_e \sin\theta = p_e^* \sin\theta^*. \tag{30}$$

Here, $\vec{p_e^*} = p_e^*(\cos\theta^*, \sin\theta^*\cos\phi^*, \sin\theta^*\sin\phi^*)$ and θ^* and θ^* are in the spherical polar coordinate system in the muon rest frame. ϕ^* is an angle on the plane perpendicular to the x-axis, therefore there is no change between the frames,

$$\phi = \phi^*. \tag{31}$$

The left plot in Fig. 57 displays the decay positron energy spectrum in the muon rest frame. η is normalized by its maximum energy. The right plot displays the energy spectrum of decay positrons in the Lab frame, with a μ-beam momentum of $p_\mu = 300$ MeV/c.

Figure 58 displays the E_{lab} vs. $\cos\theta_{lab}$ scatter plot for all positrons generated by GEANT4, $P_\mu = 1$. θ_{lab} is the cone angle with respect to the X_{Lab}-axis in the rotation frame as shown in Fig. 56. The positrons are boosted towards the direction of the muon momentum ($\cos\theta_{lab} \geq 0.96$ or $\theta_{lab} \leq 0.3$ [rad]).

As we introduced, we have spin-dependent spectra by selecting events of $\eta > 0.75$ in a certain solid cone angle as in Table XII. In the next section, we will discuss energy spectra of such solid angles.

D. Energy spectra in the lab frame

Figure 59 displays energy spectra in the lab frame for *forward, backward, left* and *right-decays* as seen in the muon rest frame in Fig. 55. The thin black line is the histogram for all decays. The thick black line corresponds to $\eta > 0.75$, when η is the positron energy fraction in the muon rest frame. The pink and purple filled areas are *forward* and *backward* decays. The green and orange thick lines are *left* and *right* decays. (Table XII defines the acceptances.)

The emission angle in the muon rest frame determines whether the positrons in the lab frame are strongly boosted or not, and cause energy dependence in the lab frame, with forward decays highly boosted, with $E_{lab} > 180$ MeV.

Figure 60 shows the positron time spectra for 65 M simulated events for a set of positron energy ranges in the lab frame. This corresponds to Eq. 26. Integral interval for η and *theta** in the μ frame are related to the lab frame energy E_{lab} interval as discussed in Eq. 33. The spin precession "wiggle" is evident for $E_{lab} \geq 175$ MeV, and is also visible at low positron energy.

E. Event selection by lab-energy threshold

We can select *forward-decay* by applying a proper energy threshold in the lab frame. We do not need to know of the information in the muon rest frame. In this section, we will discuss the effective analyzing power as a function of energy threshold (E_{lab}^{th}) in the lab frame [64]. The first goal of this section is to introduce an effective analyzing power for *forward-decay* and the acceptance in the muon rest frame. We can then optimize the energy threshold, using a figure of merit, for the measurement of ω_a. we choose appropriate energy threshold.

1. *Relation between E_{lab}, η and θ^**

To transform E_{lab}^{th} in the lab frame into a boundary condition in the muon rest frame, we set the mass of the positron $m_e = 0$, $\beta_\mu = 1$ and express the energy or momentum in units of $(p_e^*)_{max}$ (i.e. $1/2m_\mu$). Equations 29 in this particular case become;

$$\begin{aligned} \frac{E_{lab}}{m_\mu/2}\cos\theta &= \eta\gamma_\mu(1+\cos\theta^*), \\ \frac{E_{lab}}{m_\mu/2}\sin\theta &= \eta\sin\theta^*, \end{aligned} \tag{32}$$

θ is the angle of the positron and μ directions in the lab frame. E_{lab} is given by

$$\frac{E_{lab}}{m_\mu/2} = \sqrt{\eta^2\sin^2\theta^* + \eta^2\gamma_\mu^2(1+\cos\theta^*)^2}. \tag{33}$$

Taking $\gamma_\mu >> 1$ and $(E_{lab}/\eta)^2 >> 1$, we obtain

$$\cos\theta^* = \frac{E_{lab}}{\eta\gamma_\mu} - 1. \tag{34}$$

From this equation, we relate E_{lab} to θ^* and η.

The upper scatter plot in Fig. 61 displays correlation between $\cos\theta^*$ and E_{lab}. These events are all generated by GEANT4. The boundary of the scatter plot corresponds to Eq. 34 at $\eta = 1$, which is shown in the black solid line in the middle and bottom plots. The blue and red dotted lines correspond to $\eta = 0.5$ and $\eta = 0.75$. The filled area in green in the middle plot is *forward-decay in the muon rest frame.* The filled area in blue, edged with pink in the bottom plot represents *forward-decay selected by* E_{lab}. These plots suggest the most of the areas of the two types of selected *forward-decays* are common.

In the next subsection, we will discuss how to find a proper energy threshold E_{lab}^{th} at given γ_μ.

2. Appropriate E_{lab}^{th} for the maximum FOM

We describe the relative number of events above an energy threshold of $E_{lab} \geq E_{lab}^{th}$ as C^{th}. From Eq. 26 integration over Ω and η:

$$C^{th} = \frac{\int n(\eta)\mathrm{d}\eta \int \mathrm{d}(\cos\theta^*) \int \mathrm{d}\phi^*}{\int \mathrm{d}\eta \int \mathrm{d}(\cos\theta^*) \int \mathrm{d}\phi^*}. \tag{35}$$

The analyzing power for $E_{lab} \geq E_{lab}^{th}$:

$$C^{th}\cdot A = \frac{\int\int\int n(\eta)a(\eta)\{\cos\theta^*\cos(\omega_a\cdot t) + \sin\theta^*\cos\phi^*\sin(\omega_a\cdot t)\}\mathrm{d}\eta\mathrm{d}(\cos\theta^*)\mathrm{d}\phi^*}{\int \mathrm{d}\eta \int \mathrm{d}(\cos\theta^*) \int \mathrm{d}\phi^*}. \tag{36}$$

The two integrals are not independent in the lab frame but are related to E_{lab} as shown in Eq. 34. By using Eq. 34, two equations become

$$\begin{aligned} C^{th} &= \left[1 - \frac{5b}{6} + \frac{b^3}{8} + \frac{b^4}{48}\right], \\ C^{th} \cdot A &= \left[\frac{b}{6} - \frac{b^3}{8} + \frac{b^4}{24}\right], \end{aligned} \tag{37}$$

$b = E^{th}_{lab}/\gamma_\mu$ and E^{th}_{lab} is unit of $m_\mu/2$. The figure of merit for the measurement of ω_a is $C^{th} \cdot A^2$. Figure 62 displays C^{th} and A and FOM $\propto$ as a function of b.

In this way, we can select an appropriate E^{th} to have the maximum FOM at any γ_μ. E^{th}_{lab} is 200 MeV for $\gamma_\mu = 3$. And we have $C^{th} = 0.13$ and $A = 0.46$. This laboratory energy threshold selects forward positron decays in the muon rest frame, and give the optimum figure of merit for measuring ω_a

F. Confirmation of GEANT4

Finally, we estimate C^{th} and A by GEANT4 applying $E^{th}_e = 200$ MeV with a condition of $\gamma_\mu = 3$ and $B = 3$ T. Event fraction in red area in Fig. 63 is 13 %. This is consistent with expected value from 62. Time spectrum generated by GEANT4 confirms A by applying fit function,

$$F(t) = F \cdot \exp(-\frac{t}{\gamma_\mu \tau}) \left[1 + A \cos(\omega_a\ t)\right], \tag{38}$$

with three free parameters of F, A and ω_a.

Extracted anomalous period $2\pi/\omega_a$ from time spectrum is 2112.1 ns, and consistent with expected value 2111.7 ns within the statistical uncertainty of the simulated events.

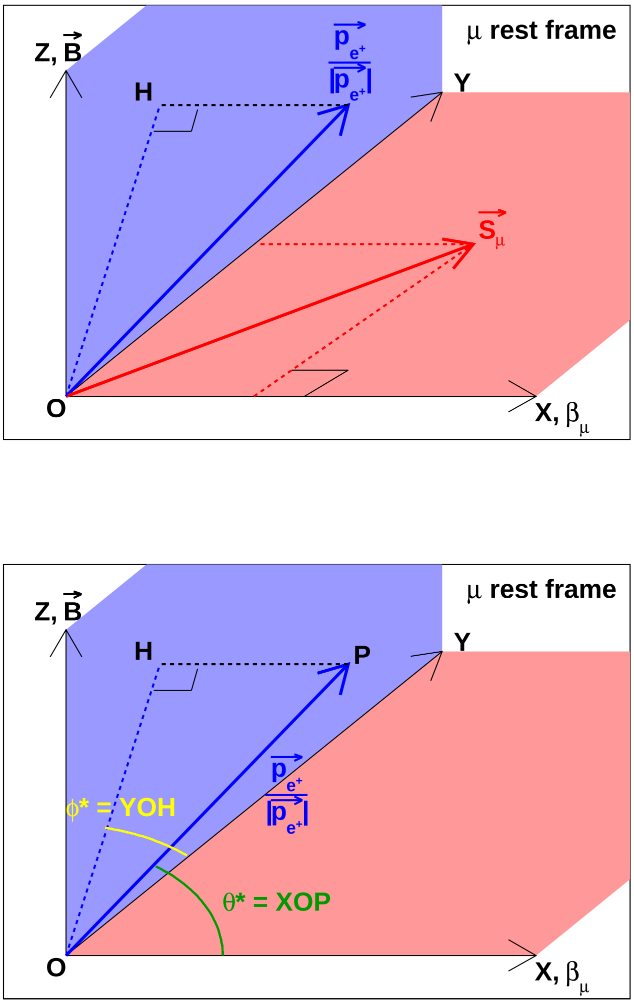

FIG. 54: Top: The direction of the the beam (along the x-axis) and the direction of the magnetic field (along the y-axis) in the muon rest frame are defined. The spin vector, displayed as a red arrow, precesses as $\vec{S}_\mu = (\cos(\omega_a \cdot t), \sin(\omega_a \cdot t), 0)$. $\vec{p}_e$ is the momentum of the positron. θ_S is the angle between $\vec{S}_\mu$ and $\vec{P}_e^*/|\vec{P}_e^*|$. Bottom: We adopt the spherical polar coordinates (1, θ^*, ϕ^*) with the polar angle θ^* and $\phi^* = 0$ on the plane of the muon spin precession (the x-y plane). The unit vector of the decay positron is $\vec{P}_e^* / \mid \vec{P}_e^* \mid =(\cos\theta^*, \sin\theta^* \cos\phi^*, \sin\theta^* \sin\phi^*)$ as displayed as a blue arrow. θ^* is the angle between the blue arrow and the x-axis. ϕ^* is the angle between $\vec{\mathrm{OH}}$ and the y-axis. Here H is the projection of the blue arrow in the $y - z$ plane.

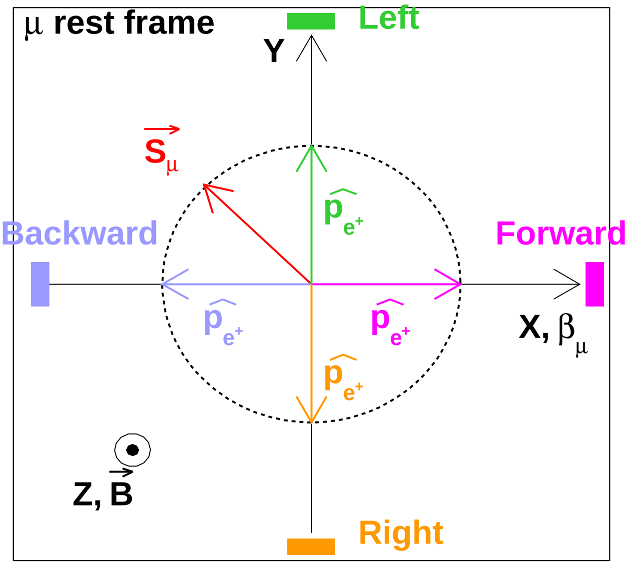

FIG. 55: Examples of *forward, backward, left* and *right-decays* are shown.

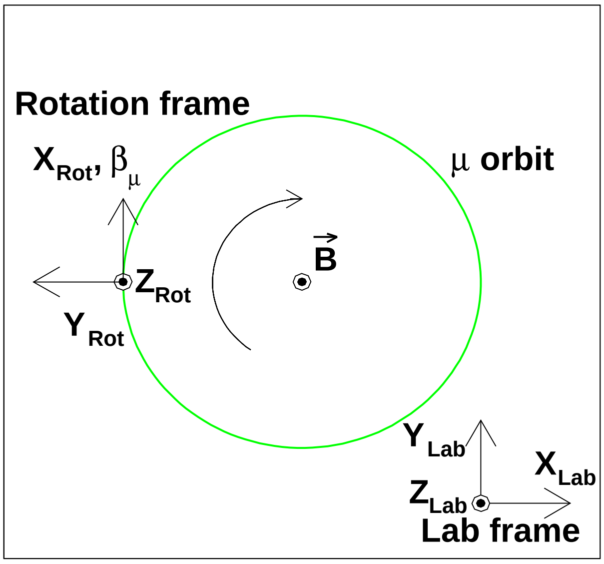

FIG. 56: This figure explains the rotation frame. X_{Lab}, Y_{Lab} and Z_{Lab} denote the lab frame. In the presence of a static magnetic field along the Z_{Lab}-axis, a μ particle with non-zero β_μ undergoes cyclotron motion in the $X_{Lab} - Y_{Lab}$ plane. The origin of the rotation coordinate system is the μ decay point. We set the X_{Rot}-axis to be the direction of the μ beam (β_μ), and the Z_{Rot}-axis is parallel to the Z_{Lab}-axis.

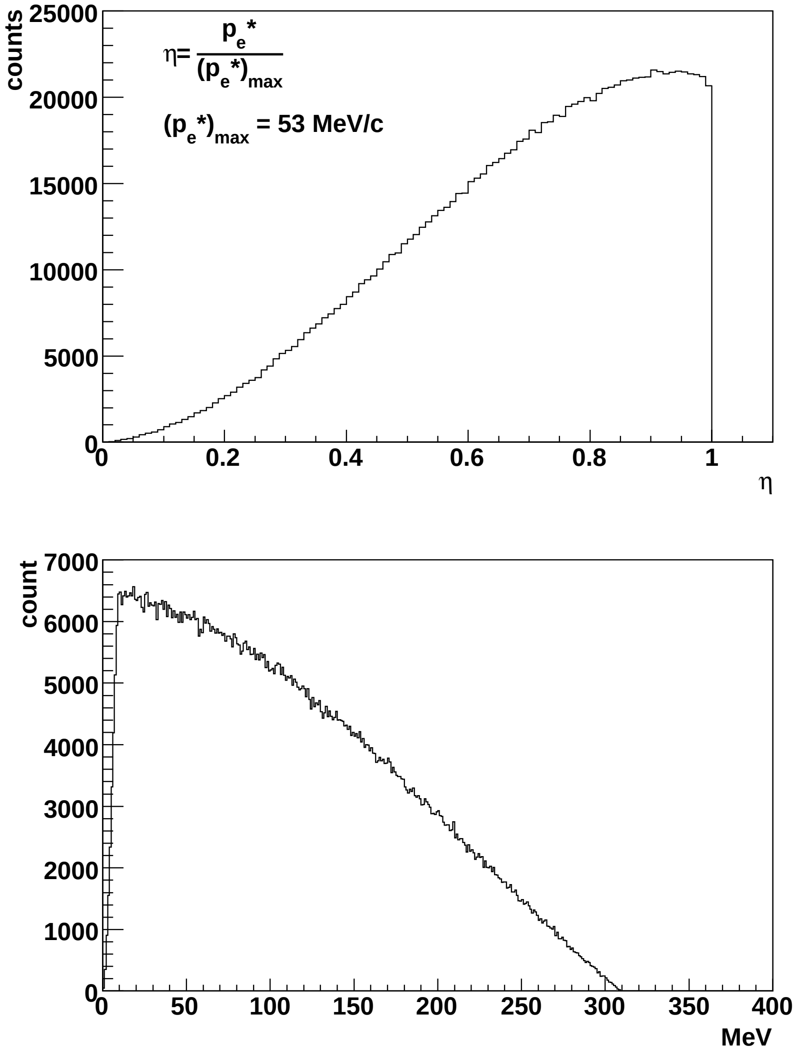

FIG. 57: Energy spectra simulation generated by GEANT4. Top: Emission energy spectrum of decay positrons in the muon rest frame, normalized by its maximum energy $(p_e^*)_{max}$. Bottom: Emission energy spectrum of decay positrons in the lab frame. We set the μ-beam momentum to 300 MeV/c for this simulation.

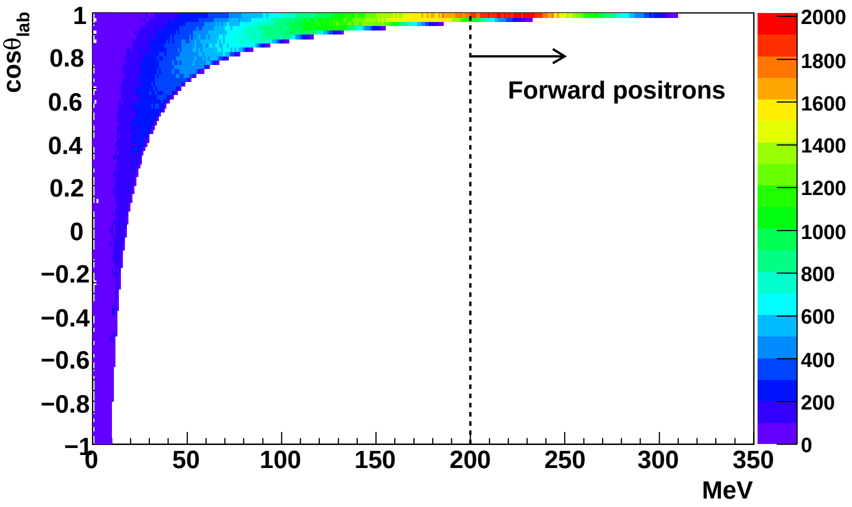

FIG. 58: E_{lab} vs. $\cos\theta_{lab}$ scatter plot for all positrons generated by GEANT4, $P_\mu = 1$. Positrons with $E_{lab} \geq 200$ MeV are emitted in the forward direction ($\theta_{lab} \leq 0.3$ [rad]) with respect to the μ direction in the muon rest frame.

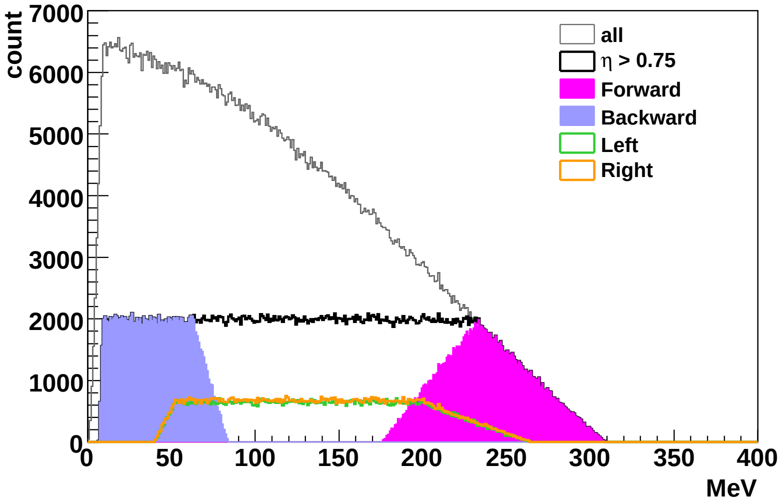

FIG. 59: Energy spectra of the decay positrons from μ ($p_\mu = 300$ MeV/c) in the lab frame. Gray line is same as right plot of Fig. 57. The thin black line is the histogram for all decays. The thick black line corresponds to $\eta > 0.75$. The pink and purple filled areas are *forward* and *backward* decays. The green and orange thick lines are *left* and *right* decays. Although we select events $\eta > 0.75$ in the muon rest frame, the emission angle affects the positron energies in the lab frame.

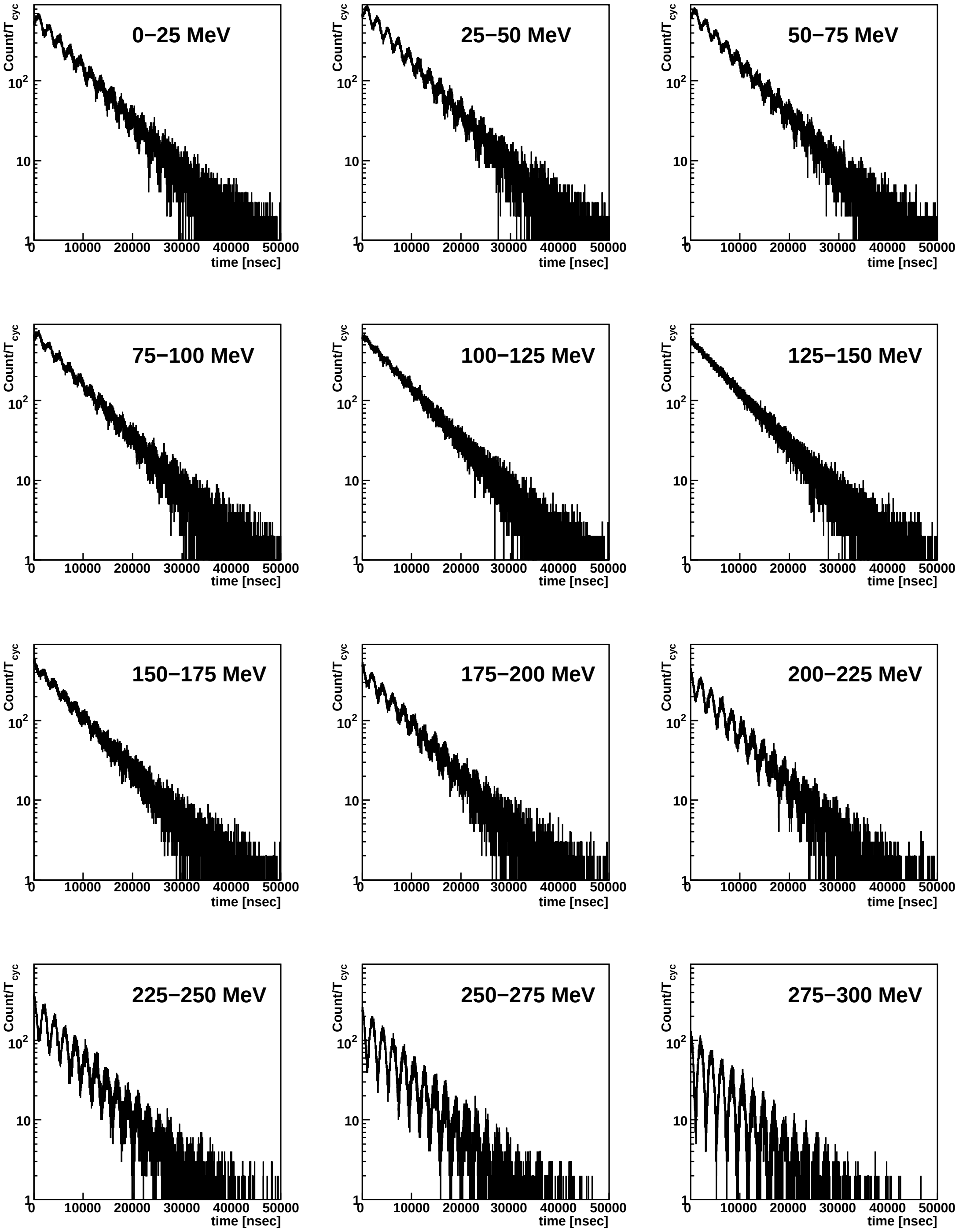

FIG. 60: Positron time spectra generated by Geant4 for 65M events for several energies, with $P_{mu} = 1$. Spectra of $E_{lab} < 100$ MeV ($E_{lab} > 175$ MeV) correspond to *backward-decay* (*forward-decay*) in the muon rest frame.

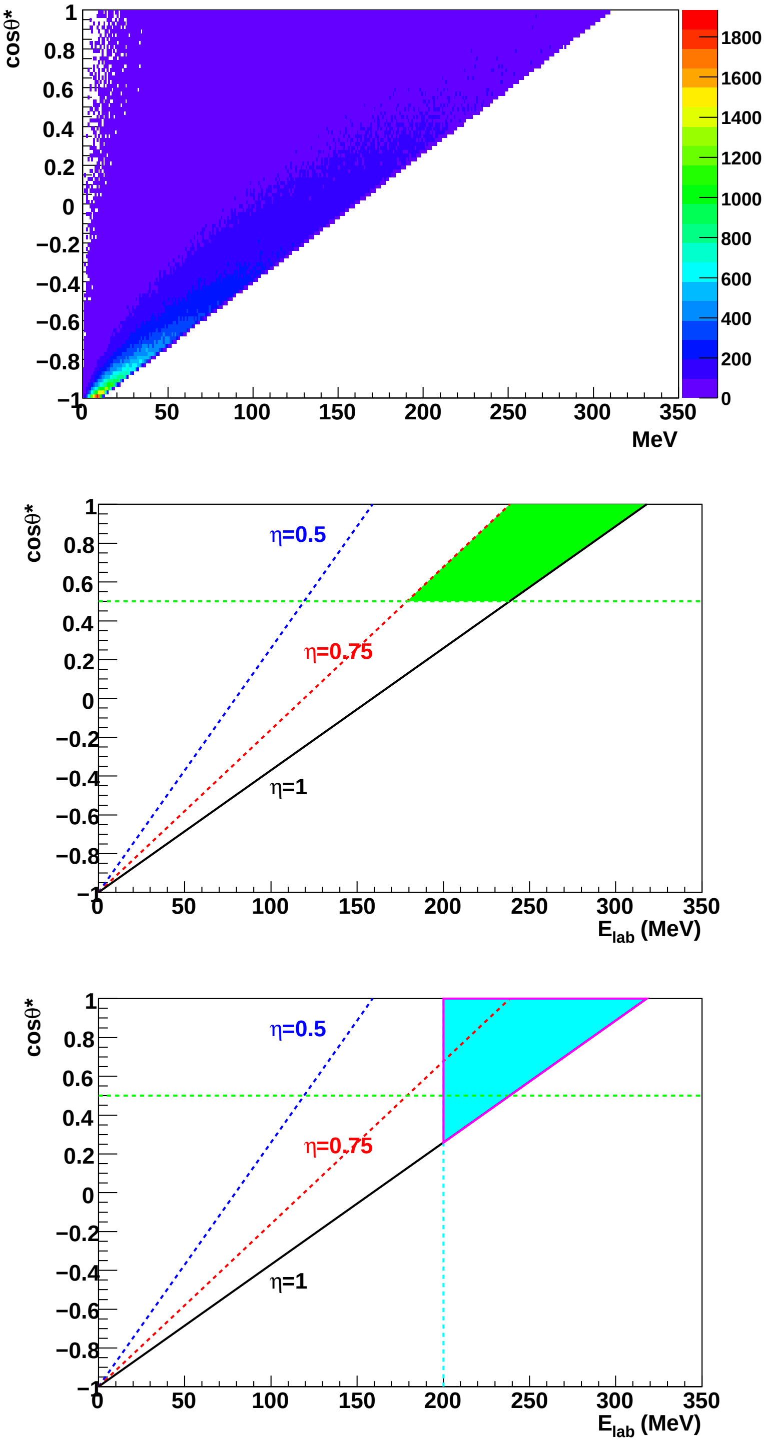

FIG. 61: Up: E_{lab} vs. $\cos\theta^{*}$ scatter for all positrons generated by GEANT4. The boundary comes from Eq. 34 at $\eta = 1$.

Middle and bottom: Correlation between $\cos\theta^{*}$ and E_{lab} introduced in Eq. 34. The black solid line corresponds to $\eta = 1$. blue and red dotted lines correspond to $\eta = 0.5$ and $\eta = 0.75$. The filled area in green (middle plot) is the selected area by *parameters in the mu rest frame*. The filled area in blue, edged with pink for is for *the lab-threshold*.

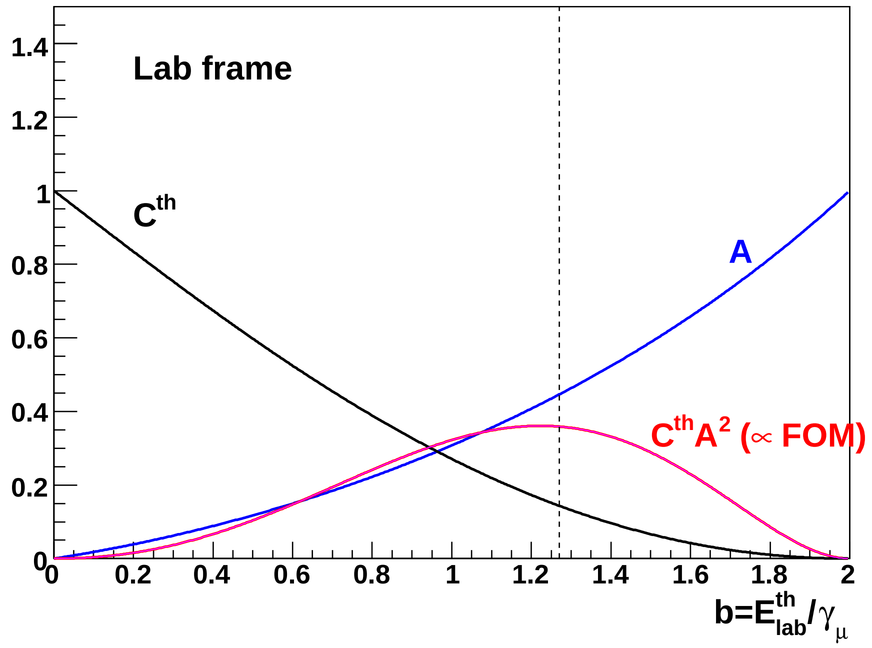

FIG. 62: At $b = 1.27$, FOM is maximum and effective analyzing power is 0.46.

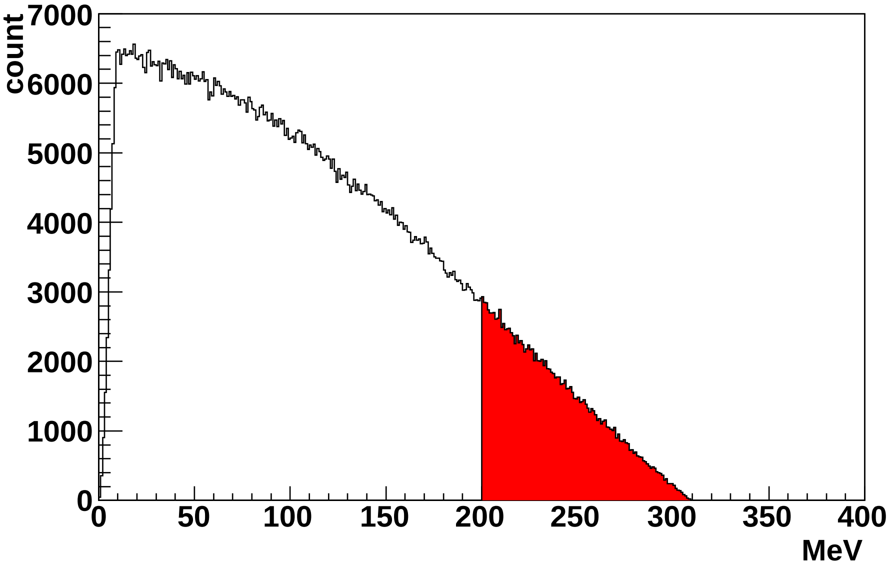

FIG. 63: Energy spectrum of decayed positrons. Above $E_e > 200$ MeV region, which is filled in red, is 13%. This is consistent with $C^{th} = 0.13$ from Fig. 62.

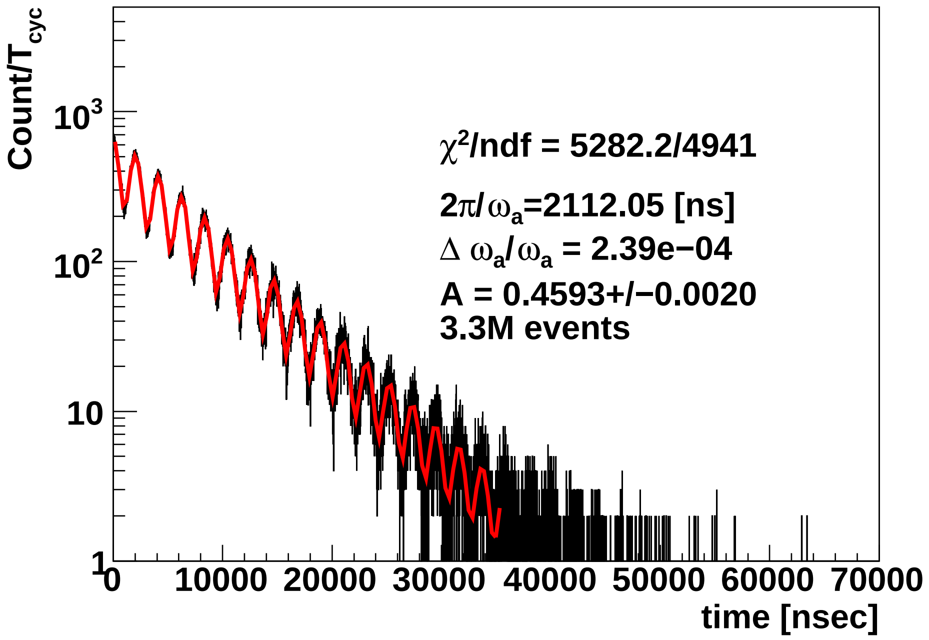

FIG. 64: Time spectrum of decayed positrons of $E_e \geq 200$ MeV. From fitting results, amplitude is 0.46. This is consistent with A in Fig. 62.

VIII. DETECTION OF DECAY POSITRON

Detectors to measure the decay positrons from the muon beam are discussed in this section.

A. Requirements

After injection into the muon storage region, the positive muons circulate in a plane parallel to the magnetic field with a radius of 33 cm. They decay into a positron and two neutrinos with a time-dilated lifetime of 6.6 μs. The anomalous muon precession period is 2.2 μs, which is about 300 times the cyclotron period (7.4 ns), i.e. the muon spin rotates 360 degrees in every 300 turns in the storage region. Because of the parity violation in the weak decay of the muon, there is a correlation between the muon spin and the direction of the positron momentum. The correlation (analyzing power) has an energy and angular dependence.

In the muon center of mass frame, the positrons tend to decay towards the direction of the muon spin at the maximum positron energy of E_{max}=52.8 MeV (the Michel edge). The analyzing power becomes smaller in the mid-energy range of $E/E_{max} \sim 0.5$, then becomes negative in the lowest energy range of $E/E_{max} \sim 0$, where the direction of the positron tends to be opposite of the the muon spin direction. This correlation allows one to measure the time dependence of the muon spin direction by detecting positrons and their energy as a function of time.

This correlation remains in the laboratory frame. From Fig. 62, it is clear that higher analysing power is obtained with the higher energy threshold, while the number of positrons decreases. The statistical uncertainty is proportional to the figure-of-merit (FOM) $C^{th}A^2$. The FOM is maximum at around E^{th} = 190 MeV. The maximum positron energy in the laboratory frame is 310 MeV. Thus the positron detector should be efficient, especially to detect positrons in the energy region above ∼190 MeV.

Due to the Lorentz boost, the positron direction is confined to a narrow cone parallel to the parent muon direction. The positrons curl into the inner part of the muon storage region where the magnetic field is as strong as that in the muon storage region (3 T). The positron momentum component parallel to the magnetic field causes it to drift vertically.

The detector system needs to large enough to accept positrons which curl to the inside of the muon storage region with a vertical drift. We have set the volume for the detector system as a tube inside the muon storage area with 40 cm in height and 27 cm in radius.

The time sequence of the $g-2$ measurement is shown in Fig. 65. The muon beam spill comes every 40 ms schyncronously with the J-PARC RF signal. The proposed rate of the muon beam is 10^6/s = 40000 muons per spill. About 10 percent of the decay positrons, 4000 positrons per spill, survive the minimum energy cut mentioned above. We anticipate that the contamination in the detector from positrons with other energies would be of the same order as the signal positrons. Therefore, about 10000 positrons enter the detector system per fill. The instantaneous rate of the whole detector system will be 10000 muons/6.6μs = 1.6 GHz at injection. This becomes 10 MHz after 33 μs. The individual detector rate would be this rate times the number of detector hits per track divided by the number of channels. The individual detectors must keep their performance (resolution, efficiency, response function) stable as a function of time in order not to introduce any undesired bias in the timing distribution which in turn will be a source of systematic uncertainty.

The detectors and their readout electronics must operate under a 3 T magnetic field. Any electric field from the detector and readout electronics should be sufficiently small so that the electric field in the muon storage region is negligible for the measurement (a few mV/m for a ppb systematic uncertainty).

We propose to use an array of radial vanes made up of silicon detectors, radially surrounded by fine-segmented timing counters with, an active absorber material (EM calorimeters) on the inner side of the tracking detectors. The conceptual layout of the detector system is shown in Fig. 66.

B. Silicon tracker

The instantaneous rate will be as high as 1.6 GHz in the detection volume. High granularity is desired to suppress systematic uncertainty from pile-up. Tracking the positrons with position sensitive detectors is beneficial in a sense that effects of pile-up can progressively be suppresesd by requiring hit-to-hit correlations in the track reconstruction. The existance of the strong magnetic field in the detection volume provides for momentum analysis.

Silicon strip detectors are considerd as the tracking detector since these detectors are compact, highly segmented, have stable gain, and do not introduce high electric field in the detection volume. The sensitive area of the silicon detector, we plan to use, is a double-sided AC-coupled rectangular silicon sensor with vertical and stereo strips with 200 μm pitch. The size of the sensor is 10 cm wide and 20 cm high. A total of 64 units of silicon strip planes will be radially placed in the detection volume to efficiently detect the circular tracks of the positrons. 32 units are used to form a set of vanes in the upper half of the detection volume, while another 32 units are for the lower half. There are 1500 strips per unit, and 96k strips in total.

At injection, there will be on average 12 tracks in the first cycrotron period (7.4 ns), and the instantaneous rate would be about 1 MHz per strip. About 1 ns timing resolution is required to disentangle overlapped positron tracks. Figure 67 shows example decay positron events for three positron energies. It can be seen that at the higher positron energy, the track path-length in the detection volume becomes longer, and thus more hits register in the tracker. On the other hand, acceptance becomes less and less at lower energies. At energies below 50 MeV, the tracker is completely insensitive to these unwanted positrons, i.e. the radius of curl up is so small that it can not be seen by any vane. Note that we are not sensitive to positrons at the highest energy (E>280 MeV) since the radius of the positron track is similar to that of muons.

C. Absorber/calorimeter

The inner tube of the detection volume with a radius of about 10 cm will be filled with heavy material to block a range of lower energy positron tracks. This is to prevent unwanted low-energy positron tracks from spiraling and continuing to keep hit the tracking detector, resulting in an increase of data volume. The absorber material and configuration will be chosen so that a calorimetoric measurement of positron energy will be possible. The calorimetric information can be used to crosscheck the calibration of the track momentum scale using a lower intensity muon beam. The track-integrated information, such as the total energy deposit and the energy-weighted position, will be useful in monitoring the muon beam intensity and position during the $g - 2$ measurement with full beam intensity. Note that the instantaneous rate of the order of a GHz at injection would not allow retrival of useful calorimeter information for individual track during the $g - 2$ measurement, with a

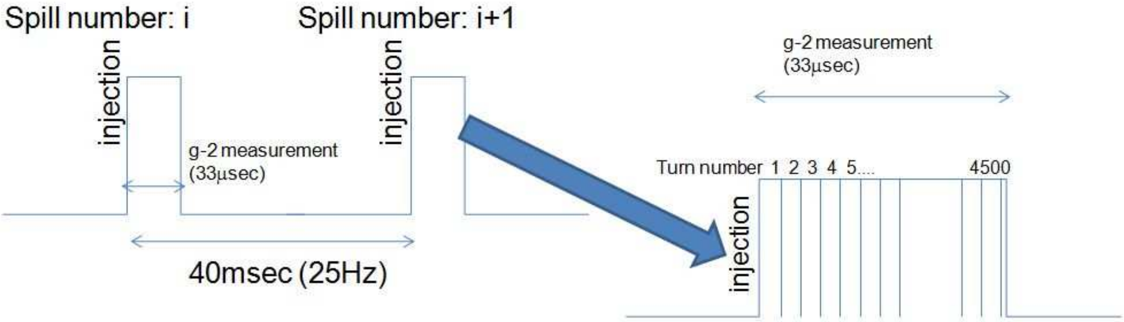

FIG. 65: Time sequence of the $g - 2$ precession measurement

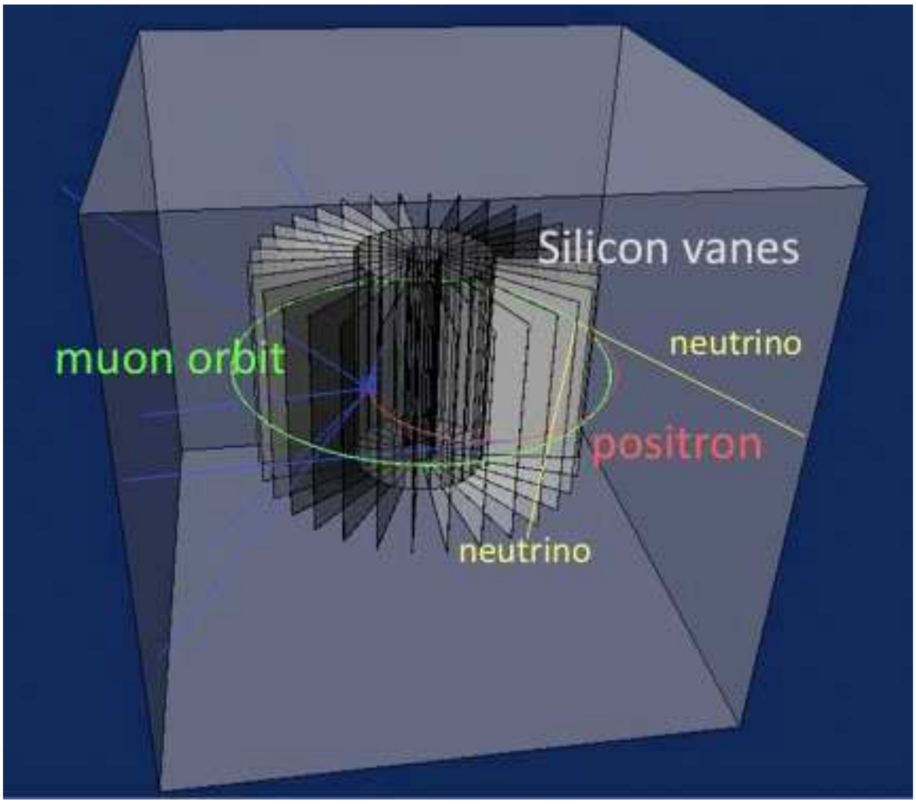

FIG. 66: Layout of the positoron detector system

foreseenable calorimeter segmentation.

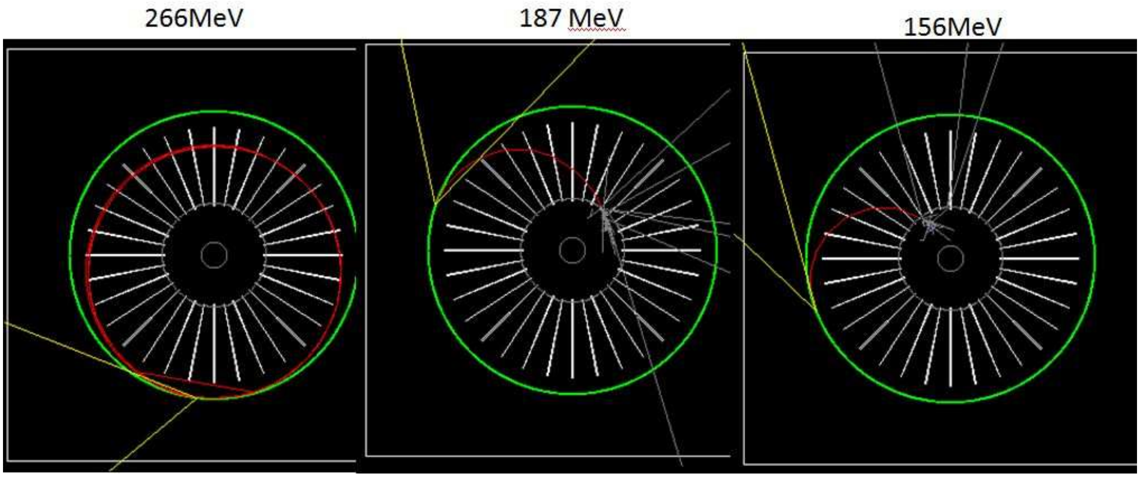

FIG. 67: Example positoron trajectries in the detector system at three different energies of positrons. The green circle is the muon beam orbit. The red trajectory is the trace of the positron track. The white tracks are photons.

IX. READOUT ELECTRONICS AND DAQ

The global timing structure of the $g-2$ measurement is shown in Fig. 65. The beam spill, which corresponds to the injection of the muon beam to the storage ring, arrives in every 40 ms (25Hz). After the beam is moved to the good field region, the detector system starts the measurement of the decay positron. The measurement will continue for five life times, i.e. 33 μs. The expected positron rate immediately after injection is 1600 MHz, and the rate reduces to 10 MHz after 33 μs. The total number of decay positrons per spill is 10k, which is estimated assuming 10 percent of the decay positrons after the energy cuts (4,000) plus 6,000 as background.

The very high instantaneous event rate requires fine granularity and timing resolution for the detectors and front-end electronics in order to reduce the probability of signal pile-up. The short duration (33 μs) of the measurement allows us to continuously take data of the signal timing and/or amplitude from the detectors and to store the data in memories on front-end electronics. The scheme can eliminate dead time and unexpected structure of timing profile, i.e. the dead time introduces a rate-dependent inefficiency in the read out which will skew the timing distribution. The long interval (40 ms) between the measurement and the subsequent spill enables us to send the data after their proper processing to a back-end DAQ system.

Figure 68 shows a conceptual block diagram of the front-end board. Signals from the tracker detectors, assuming a silicon strip detector, are processed by Amplifier Shaper Discriminator (ASD) circuits. The binary signal outputs by the ASD are then routed to Time-to-Digital Converter (TDC) circuits, where the arrival times of leading edges are stored in a buffer memory (Spill Buffer). The TDC measurement starts at receiving the “START” signal and stops at the end of the preset period, which should be shorter than the Buffer size. The resolution must be of order 1 ns and a dynamic range longer than 33 μs is required for the TDC and the buffer memory. When the measurement stops, the front-end processor circuit starts data processing. The processor reads raw data from the buffer memory and performs zero-suppression and re-formatting for the data compaction. A set of spill data fragments, which includes a fragment header and trailer, is prepared and sent to the back-end DAQ system using a set of a high speed serializer and an optical transmitter (TX) via an optical fiber. The fragment header and trailer contains Board Number Identifier

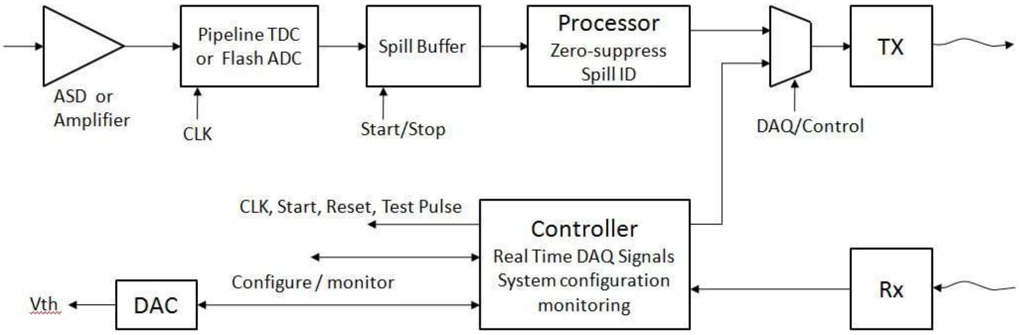

FIG. 68: Block diagram of the front-end board.

(BNID), Spill Number Identifier (SNID), status of the board, the data size, etc. and Cyclic Redundancy Check (CRC). The real time control signals, e.g. Clock, Start, Reset and Test Pulse Trigger, are provided from a set of an optical receiver and a de-serializer (RX). The bidirectional links (a set of TX and RX) are also used for system configuration, control and monitoring of a front-end board. The baud rate per the optical link will be higher than 2 Gbps. The foreseen data fragment size per spill is less than 100 kB per link, when each 100mm x 200mm double-sided silicon strip detector (1,500 channels strips) is covered by one front-end board. The ASD and the TDC will be ASIC's. Several ASIC's are on the market and have some of the desired functionality, but none could have all. We are ready to undertake a preliminary design effort. The back-end DAQ system collects the data fragments from front-end boards and builds a complete data set for each spill. The PC farm, which consists of parallel PC's, receives spill data sets via a Gigabit Ethernet network switch and does online analysis.

X. SYSTEMATIC UNCERTAINTIES

We discuss here systematic issues and estimate systematic uncertainties, comparing th the experience of the BNL E821 experiment.

The measurement consists of two separate precision measurements ; the magnetic field as seen by the stored muons, and the frequency of the muon spin precession, as observed in the high energy decay positrons.

For the measurement of B, the field, the main issues are to monitor the field in the storage ring, vacuum, to map the field frequency, and to calibrate these probes with great precision. The uncertainties, in these steps are greatly improved if the field is more uniform. The expectation is for a 1 ppm locally flat field for the solenoid storage ring in this experiment vs. ± 50 ppm local variation for E821. Therefore, most issues for B should be significantly improved for this experiment.

For the measurement of the spin precession frequency, this experiment will use high granularity tracking to overcome much higher instantaneous intensity than E821. All systematic uncertainties for ω_a derive from differences in detection early in the measurement time compared to late. The high granularity in this experiment leads to a concern that the detector elements may not see the same proportion of positrons early to late. We must estimate this uncertainty. Handling of pileup is crucial. this experiment will have the advantage of no significant flash in in the detectors at injection, which was due to incoming pion along with the muon for E821. Several systematic uncertainty issues for E821 were related to the flash – detector had to be turned off or down at injection, thresholds had to be set higher accounting for the flash.

There are many differences of the proposed measurement and E821:

- The storage ring magnet for this experiment will be much smaller diameter than E821, and is expected to have a much more locally uniform field.
- The 1.5 T field will be used in this experiment.
- The instantaneous rate in the positron detection in this experiment will be over 100× greater than for E821, before consideration of detector granularity.
- This experiment will primarily use tracking to measure the positrons, while E821 use calorimeters.

- The granularity of the detectors will be 96k channels/ 6 hits/ track = 16k, while the granularity for E821 was 24.
- The detector will be in the storage ring vacuum, while the E821 calorimeters were outside the vacuum, separated by a scalloped vacuum chamber wall.
- The detectors will be much closer to the muon decay point and reconstruction to the decay point using the timed location of the narrow muon bunch may be possible.

The development of the design and its systematic uncertainties will be an ongoing process throughout the design, measurement, and analysis stages. As it was for E821. At this time we have used the published systematic uncertainty tables from E821 as a starting point to develop table for this experiment. These follow, with estimates for J-PARC where possible at this time, and with remarks.

TABLE XIII: Systematic uncertainties for ω_a are listed for the E821 experiment Run 01 (R01) and for this experiment.

Source of uncertainty	E821-R01 (ppm)	J-PARC (ppm)	Remarks for this experiment
Pileup	0.08	<0.05(goal)	start with 133x pileup E821, detector design requires reducing the pileup contribution to below 0.05 ppm. Uncertainty in ω_a for E821 comes from not identifying two positrons in calorimeter and assigning the time according to the wrong energy (the time of the muon decay vs. the time of the positron at the calorimeter). When a positron energy contributing to pileup was below threshold, it was not sampled and the correction approach used in E821 has this uncertainty for the amount of pileup observed. For this experiment, the time of the positron track will be much closer to the time of the muon decay, so that this uncertainty should be less for the same level of pileup. Also, pileup in this experiment for the tracking would result in reduced efficiency and probably would not affect the time.
AGS background	< 0.1	0.0	there is no stored beam in this experiment during data-taking, so no background of this type
Lost muons	0.09	<<0.09	there will be no material near the stored beam in this experiment; question of resonance loss needs to be studied. Much reduced emittance in this experiment should reduce resonance loss. Also, if we use a very small focusing field, should avoid losses entirely

TABLE XIII: (continued)

Source of uncertainty	E821-R01 (ppm)	J-PARC (ppm)	Remarks for this experiment
Timing shifts	< 0.1	<<0.1	This came from the photomultiplier response to turning the PMs on after the flash of pions entering the ring with the muons, in E821. For this experiment, there will be no pions, no flash, and the detector will not be turned off between fills. Should be much smaller in this experiment.
E-field, pitch	<0.1	<<0.1	Very small pitch correction (tiny transverse divergence), no E-field correction if a small magnetic focusing field is used.
Fitting/binning	<0.1	<<0.1	Fewer $g-2$ cycles per lifetime in this experiment–need to discuss this. For E821 this is an inclusive category for unaccounted for fitting issues and how this might pull the frequency
Coherent Betatron Oscillation	0.07	0.00	not present in this experiment for small (or no) focusing field (for focusing with n=3×10^{-5}, $f_{CBO} = 490$ us, 74 muon lifetimes)
Gain changes	0.12	<<0.1?	Tracking efficiency vs. rate issue is being studied. Possible bias on curvature vs. time in store, also being studied. For E821 the gain changes were from turning off the photomultiplier tubes during the flash from injection. There will be no flash in this experiment, and the detector will not be shut down between fills.
Others	–	–	Any other categories for this experiment are being searched for.
Total (ω_a)	0.21	0.07 (goal)	

TABLE XIV: Systematic uncertainties for B.

Source of errors	E821-R01 (ppm)	J-PARC (ppm)	Remarks for this experiment
Absolute calibration of standard probe	0.05	0.05	Issue is how spherical is the absolute probe–same issue for this experiment
Calibration of trolley probes (field measurement on the muon trajectory)	0.09	<0.09	Much better field uniformity expected for this experiment, so that transferring calibration from absolute probe to trolley probes should have less uncertainty from position errors.
Trolley measurement B_0	0.05	<0.05	Much better field uniformity in this experiment
Interpolation using fixed probes	0.07	<0.07	Should be smaller in this experiment due to expected uniformity and stability of smaller magnet
Uncertainty from muon distribution	0.03	<0.03	Should be small with tracking and bunched beam
Inflector fringe field uncertainty	0.00	0.00	no inflector
Others[a]	0.10	–	Need to consider these, and others?
Higher multipoles (should be negligible for solenoid for this experiment)			
Trolley temperature			
Trolley power supply voltage response			
Eddy currents from kicker			
Total systematic error on ω_p	0.17	<0.07(goal)	

[a]

XI. ELECTRIC DIPOLE MOMENT

Just as the anomalous magnetic moment of the muon, a_μ has been measured for more than half a century, the electric dipole moment of the muon, d_μ has also been searched for many years. While a_μ serves as a solid test ground for the Standard Model of the particle physics, non-zero d_μ value immediately means CP violation in the lepton sector. It is parametrized as

$$\vec{d_\mu} = \eta \frac{e\hbar}{2m_\mu} \vec{s}. \tag{39}$$

In the presence of the static field $\vec{B}$ and $\vec{E}$, the Hamiltonian of the system can be written as

$$\mathcal{H} = -\vec{\mu}_\mu \cdot \vec{B} - \vec{d_\mu} \cdot \vec{E}. \tag{40}$$

Equation 40 gives a definition of d_μ. The second term, $-\vec{d_\mu} \cdot \vec{E}$ is odd under P and T transformations. Therefore nonzero value of the d_μ violates T, and also CP, if CPT theorem holds.

The most recent measurement of d_μ (as well as a_μ), E821[5] at Brookhaven National Laboratory (BNL), has constrained d_μ down to $\leq 1.9 \times 10^{-19}\mathrm{e \cdot cm}$. The d_μ limit is, however, still required to be improved.

In the presence of the electric dipole moment, the static magnetic field $\vec{B}$ and static electric field $\vec{E}$, the EDM rotation $\vec{\omega}_\eta$ is given as an additional rotation to the muon spin precession:

$$\vec{\omega}_{all} = \vec{\omega}_a + \vec{\omega}_\eta = -\frac{e}{m_\mu}\left[a_\mu \vec{B} - \left(a_\mu - \frac{1}{\gamma^2 - 1}\right)\frac{\vec{\beta} \times \vec{E}}{c}\right] + \frac{e}{m_\mu}\left[\frac{\eta}{2}\left(\vec{\beta} \times \vec{B} + \frac{\vec{E}}{c}\right)\right]. \tag{41}$$

Eliminating the terms proportional to the electric field, Eq. 41 simplifies as

$$\vec{\omega}_{all} = \vec{\omega}_a + \vec{\omega}_\eta = -\frac{e}{m_\mu}\left[a_\mu \vec{B} - \frac{\eta}{2}\left(\vec{\beta} \times \vec{B}\right)\right]. \tag{42}$$

Since the rotation axises due to a_μ and d_μ are orthogonal to each other, separation of these signal should be possible. Based on this fact, E821 group measure d_μ without changing experimental configuration with moderate precision.

Instead of setting the spin direction along the muon momentum direction, we can rotate the muon spin axis from the momentum direction to parallel to the magnetic field; spin up (or anti-parallel; spin down), such that the precession measurement depends only on the d_μ.

In this case, the time evolution dependence of the positron yield is written as:

$$N_e(t) = N_0 \cdot \exp\left(-\frac{t}{\gamma_\mu \tau}\right) \{1 + AP_\mu \sin(\omega_\eta\ t) \cdot \cos(\omega_a\ t)\}. \tag{43}$$

Because ω_η is much smaller than ω_a, $AP_\mu \sin(\omega_\eta\ t)$ term can be treated as an *effective amplitude*, and should grow as a function of time, if ω_η is *not* precisely zero. This means that the observation of the spin precession is a direct measurement of the *non-zero* d_μ. The upper plot in Fig. 69 displays the time dependence of positron yield for $d_\mu = 10^{-19}\mathrm{e} \cdot \mathrm{cm}$ with the muon spin up. The statistics is set as the half that of the $g-2$ experiment to reach the 0.1 ppm for a_μ. If we have another half statistics with the muon spin down, we can take asymmetry of these two time spectra. The lower plot in Fig. 69 displays asymmetry as a function of time spin up and down. Figure 70 displays the same but $d_\mu = 10^{-22}\mathrm{e} \cdot \mathrm{cm}$ case.

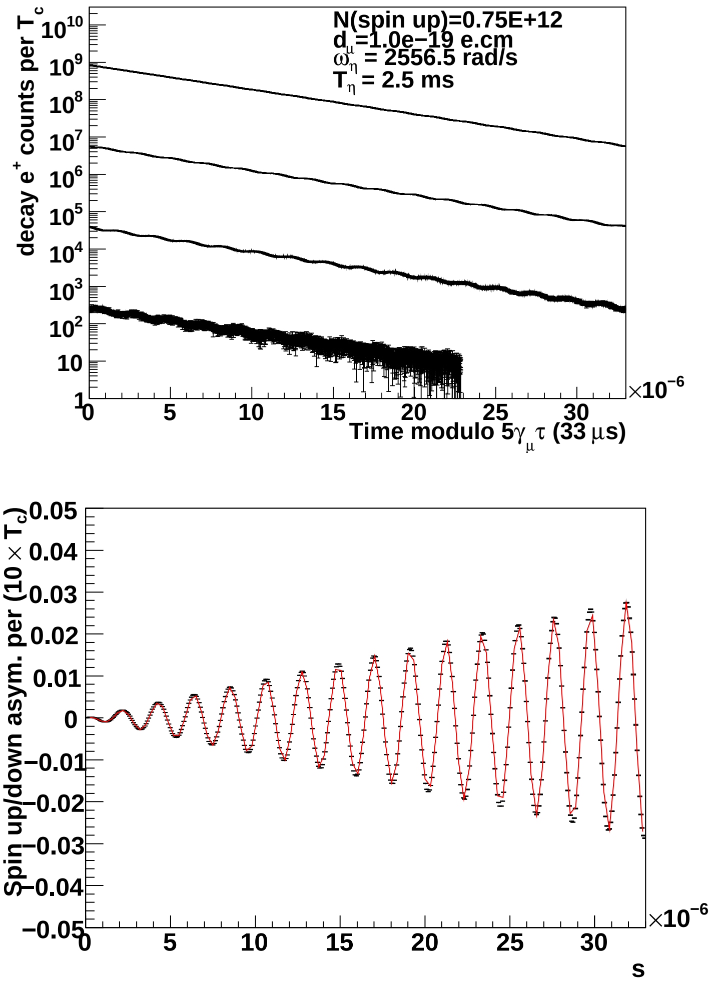

FIG. 69: Top: Time spectrum of positron of $d_\mu = 10^{-19}\mathrm{e}\cdot\mathrm{cm}$ for $P_\mu = 1$ (Initial spin direction is parallel to the magnetic field).
Bottom: Asymmetry of positron yield as a function of time for spin up and spin down for 5 lifetimes. Red solid line is fitted line with an expected function (reduced chi-square value is 1.1). Envelope behaves as $AP_\mu \sin(\omega_\eta\ t)$.

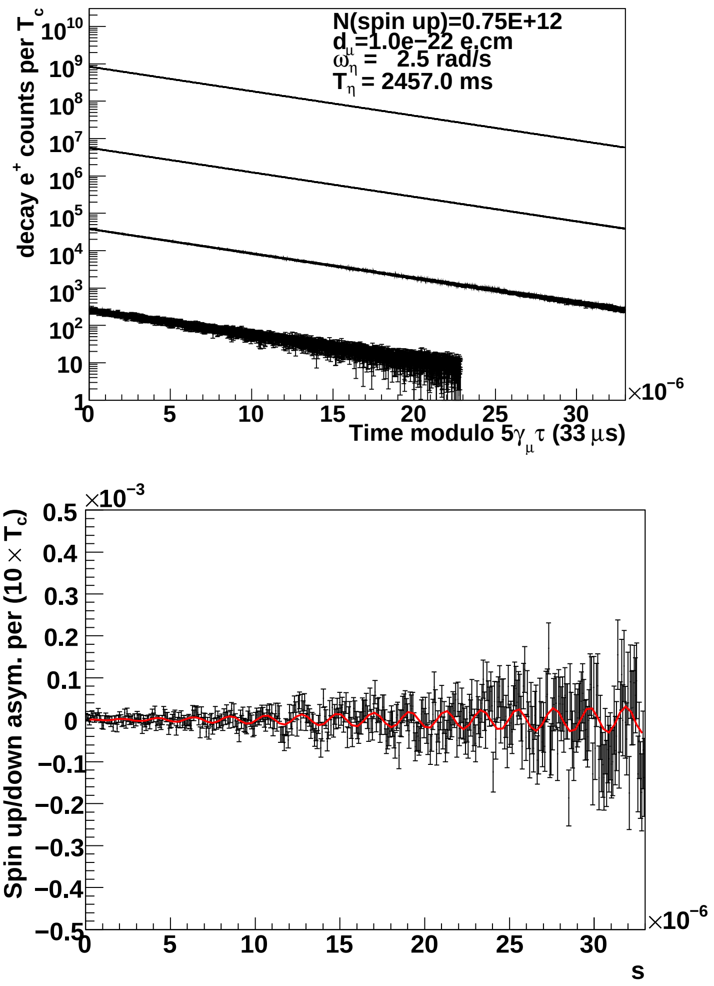

FIG. 70: Top: Time spectrum of positron of $d_\mu = 10^{-22}\mathrm{e}\cdot\mathrm{cm}$ for $P_\mu = 1$ (Initial spin direction is parallel to the magnetic field).

Bottom: Asymmetry of positron yield as a function of time for spin up and spin down for 5 lifetimes. Red solid line is fitted line with an expected function (reduced chi-square value is 1.1).

XII. SCHEDULE AND COST

We intend to start the experiment in 2014 as shown in Fig. 71. There are four major areas of activities: the ultra-cold muon Source, the ultra-cold muon beam, the ultra-precision field, and the detector system. Especially the development of the muon source represents a major challenge. We plan to perform a test experiment at TRIUMF to optimize the muonium production target in 2010. In parallel, we plan a test experiment at Rutherford with a newly developed high-power laser system.

The Muon LINAC can be constructed in two years, and be commissioned together with the source.

We have started a conceptual design of the ultra-precision field employing technology developed for MRI. We expect to have an engineering drawing in a year so that construction would start in about one year. The measurement scheme with NMR probes is being developed at this time. A test of this technique at 1.5 T is planned, followed by a test in a 3 T magnet at National Institute of Radiological Science (NIRS). A reasonably long commissioning time is allocated for the magnet, since it would be one of the most time-consuming process to shim the magnet to sub-ppm level.

The physics production run should be divided into a few phases at least; the first step would be to reach similar precision to the E821, then further improvements would follow.

A cost estimate is given in Table XV. This is very preliminary without engineering designs, but we will give the basis for each number.

- **Surface muon transport**

  The surface muons produced at the production target will be transported to experimental hall for muonium production. The first capture solenoid should be made radiation resistive. Therefore, the cost estimate is based on the current conceptual design which requires 960 m of minerally insulated coil (MIC). The super conducting curved solenoid is assumed for further transport line to maximize the transport efficiency. In addition, the area should be shielded very carefully. Detailed cost estimate requires more detailed facility design, which is the next step.

- **Laser Ionization of Mu**

  The laser for this experiment is being prepared at RIKEN.

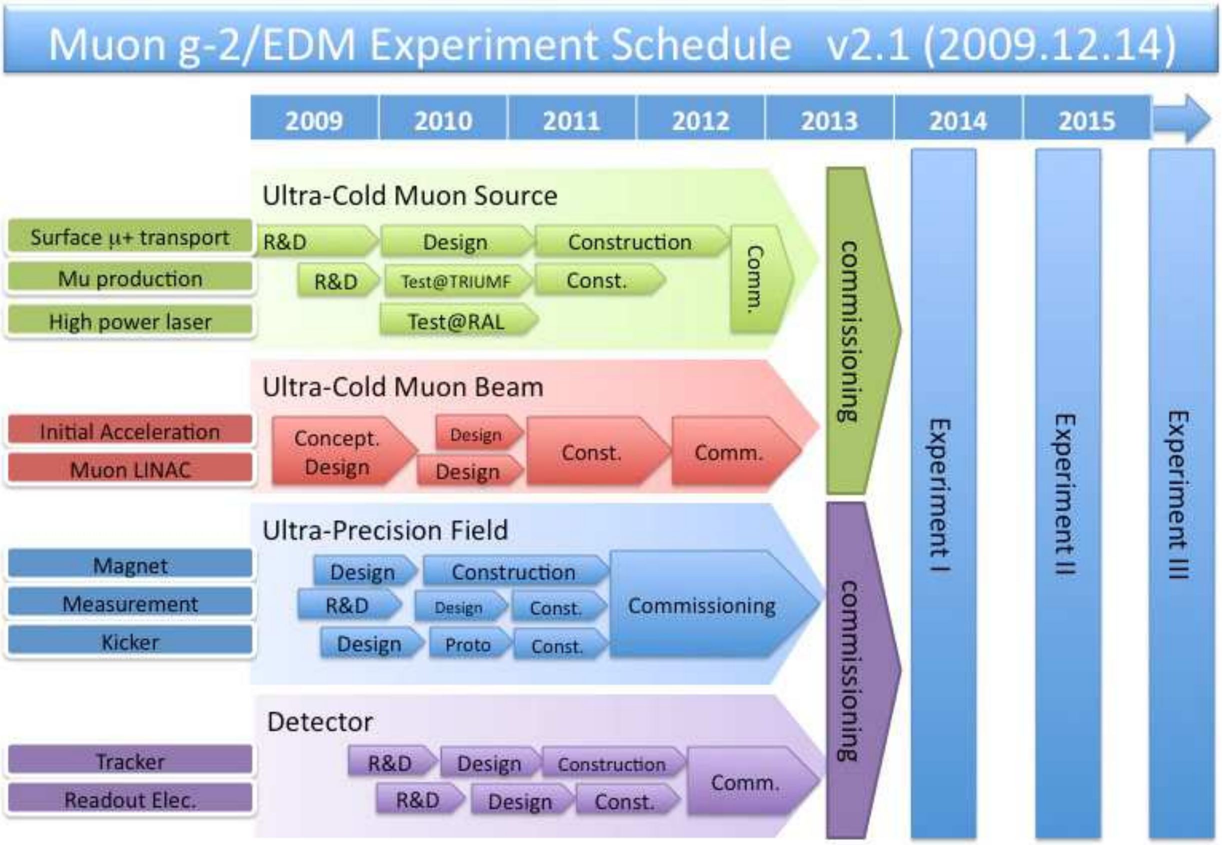

FIG. 71: Preliminary schedule of the efforts towards the experiment.

- **Muon LINAC**

  The current design assumes significant overlap in design with the existing J-PARC LINAC. This approach is expected to reduce the cost of the LINAC.

- **Ultra-precision magnet and monitor**

  The current design of the magnet resulted in the stored energy of ~30 MJ. We are working on the reduction of the energy. A major cost driver for the magnet would be person-power to achieve the required precision. Since the magnet is the heart of the experiment, we will work out the details with the in-house experts. Consequently, the cost would be minimized.

- **Detector**

  We currently assume silicon detector for the tracking detector for muon decays. It would be followed by the absorber/calorimeter.

TABLE XV: Preliminary estimate of the cost of this experiment.

Item		Cost (Oku-yen)
Surface Muon Transport		Facility
Ultra-Cold Muon Source		
	High-power Laser System	3.0
	Initial Acceleration System	0.5
Muon LINAC		15
Ultra-precision Magnet		
	Solenoid	10
	Field Monitor	1
Detector System		
	Silicon Tracker	1.5
	Readout Electronics	0.5
TOTAL		32 + Facility

XIII. SUMMARY

We propose to measure the anomalous magnetic moment of the positive muon a_μ down to the level of 0.1 ppm with a novel technique utilizing an *ultra-cold muon beam* accelerated to 320 MeV and a 66 cm diameter precision magnetic storage ring without focusing field. The beam will be also useful in measuring the electric dipole moment beyond current precision.

The proposed measurement will provide a rigorous test of the Standard Model of particle physics as demonstrated by previous experiments. Our measurement will be complimentary to the previous measurement which was done at 3.1 GeV, the "magic" energy approach with a 14 m diameter storage ring. This proposed experiment will have very different systematics from the previous experiment.

There are many challenges in realizing the experiment. Those include

- increasing the surface muon flux,
- optimizing the muonium target,
- realizing the high-power Lyman-α laser,
- developing the scheme to maximize the muon polarization,
- finishing the actual design of the re-acceleration system,
- monitoring the very low intensity muon beam,
- realizing the ultra-precision magnetic field with *zero* electric field, and
- developing the high-rate tracking detctor system.

Although we have touched the most of the areas mentioned above, and we have developed the time-line of these R&D activities, we are almost sure that we will have new challenges on the way to realizing the experiment. It is the nature of this kind of precision physics, which requires continuing efforts.

We conclude this proposal by requesting the lab's deep involvement into this new experiment, which has full of new challenges!

[1] T.Kinoshita and M.Nio, Phys. Rev. D73, 013003 (2006); T.Aoyama et al, Phys. Rev. Lett. 99, 110406 (2007); T.Kinoshita and M.Nio, Phys. Rev. D70, 113001 (2004); T.Kinoshita, Nucl. Phys. B144, 206 (2005) (Proc. Supp.); T.Kinoshita and M.Nio, Phys. Rev. D73, 053007 (2006); A.L. Kataev, arXiv:hep-ph/0602098; M. Passera, J. Phys. G31, 75 (2005).

[2] K. Hagiwara, R. Liao, A.D. Martin, D. Nomura, and T. Teubner, Preliminary results shown at Inernational Workshop, *Phipsi09*.

[3] A. Czarnecki, W. J. Marciano, and A. Vainshtein, Phys.Rev.**D67** (2003) 073006. Erratum-ibid.**D73** (2006) 119901.

[4] J. Prades, E. de Rafael, and A. Vainshtein, e-Print: arXiv:0901.0306 [hep-ph]

[5] G.W. Bennett *et al.* Muon G-2 Collaboration, Phys. Rev. **D73** (2006) 072003.

[6] Proposal submitted to Fermilab; *The New (g - 2) Experiment: A Proposal to Measure the Muon Anomalous Magnetic Moment to ±0.14 ppm Precision*, New $(g-2)$ Collaboration. Contactpersons: D. Hertzog, and B. Roberts.

[7] R. Lafaye, T. Plehn, M. Raunch and D. Zerwas, arXiv:0709.3985 [hep-ph].

[8] M. Alexander, S. Kreiss, R. Lafaye, T. Plehn, M. Rauch, and D. Zerwas, Chapter 9 in M. M. Nojiri et al., arXiv:0802.3672 [hep-ph].

[9] Hertzog, Miller, de Rafael, Roberts and Stöckinger, hep-ph/0705.4617v1.

[10] J. Hisano and K. Tobe, Phys.Lett.**B510** (2001) 197-204.

[11] J.P. Archambault, A. Czarnecki, and M. Pospelov. Phys. Rev. **D70** (2004) 073006.

[12] S. Eidelman and F. Jegerlehner, Z. Phys. C **67** (1995) 585.

[13] S. Eidelman, Proceedings of ICHEP-06, World Scientific, Vol.1, p.547, 2006.

[14] K. Hagiwara *et al.*, Phys. Lett. B **649** (2007) 173.

[15] F. Jegerlehner, Nucl. Phys. Proc. Suppl. **181-182** (2008) 26.

[16] M. Davier *et al.*, Eur. Phys. J. C **27** (2003) 497.

[17] M. Davier *et al.*, Eur. Phys. J. C **31** (2003) 503.

[18] R.R. Akhmetshin *et al.*, Phys. Lett. B **648** (2007) 28.

[19] M.N.Achasov *et al.*, JETP **103** (2006) 380.

[20] S. Binner, H.J. Kühn, K. Melnikov, Phys. Lett. B **459** (1999) 279.

[21] M. Benayoun *et al.*, Mod. Phys. Lett. A **14** (1999) 2605.

[22] F. Ambrosino *et al.*, Phys. Lett. B **670** (2009) 285.

[23] B. Aubert *et al.*, arXiv:0908.3589.

[24] F.V. Ignatov, Nucl. Phys. Proc. Suppl. **181-182** (2008) 101.

[25] B.Aubert *et al.*, Phys. Rev. D **77** (2008) 092002.

[26] K. Hagiwara *et al.*, Phys. Rev. D **69** (2004) 093003.

[27] F. Jegerlehner and A. Nyffeler, Phys. Rept. **477** (2009) 1.

[28] J.F. Troconiz and F.J. Yndurain, Phys. Rev. D **71** (2005) 073008.

[29] Yu.M. Bystritsky *et al.*, JETP Lett. **83** (2006) 51.

[30] M. Fujikawa *et al.*, Phys. Rev. D **78**, 072006 (2008).

[31] M. Benayoun *et al.*, Eur. Phys. J. C **55** (2008) 199.

[32] M. Davier *et al.*, arXiv:0906.5443.

[33] M. Davier *et al.*, arXiv:0908.4300.

[34] S.I. Eidelman and S.I. Serednyakov, Nucl. Phys. Proc. Suppl. **131** (2004) 19.

[35] A.E. Dorokhov, Nucl. Phys. A **790** (2007) 481.

[36] T. Blum and S. Chowdhury, Nucl. Phys. Proc. Suppl. **189** (2009) 251.

[37] D. Stöckinger, Nucl. Phys. Proc. Suppl. **181-182** (2008) 32.

[38] S. Nagamiya, T. Nagae, Y. Ooyama, Y. Miyake, H. Takano, J.R. Helliwell, J.C. Peng, Energy Review 19, 12(1999) 4-23

[39] G.Heidenreich, P. Baumann, A. Geissler, A. Strinning and W. Wagner, PSI Scientific Report VI (1998) 16

[40] N. Kawamura, S. Makimura, P. Strasser, A. Koda, H. Fujimori, K. Nishiyama, Y. Miyake, and MLF Muon Section, Nucl. Instr. and Meth. in Phys. Res. A 600(2009) 114-116

[41] S. Makimura, Y. Miyake, N. Kawamura, P. Strasser, A. Koda, K. Shimomura, H. Fujimori, K. Nishiyama, M. Kato, K. Nakahara, R. Kadono, Y. Kobayashi, J. Sagawa, T. Nakamura, M. Kaneko, H. Ozaki, H. Okamura, T. Suzuki, K. Fujimoto, K. Kira, Nucl. Instr. and Meth. in Phys. Res. A:600 (2009) 146-149

[42] P. A. Piroue and A. J. S. Smith, Phys. Rev. 148 (1966) 1315.

[43] HARP Collaboration, Eur.Phys.J.C53 (2008) 177-204.

[44] A.P. Mills Jr.et al., Phys. Rev. Lett. 56, 1463 (1986)

[45] K. Nagamine, et al., Phys. Rev. Lett., 74, 4811 (1995)

[46] P. Bakule, et al., Nucl. Instrum. Meth. B., 266, 335 (2008)

[47] G.A. Beer, et al. Phys. Rev. Lett., 57, 671 (1986)

[48] A. C. Janissen et al., Phys. Rev. A 42 (1990) 161.

[49] K. A. Woodle et al., Z. Phys. D 9 (1988) 59.

[50] R. F. Kiefl et al.,Hyp. Int. 6 (1979) 185.

[51] G. M. Marshall et al., Phys. lett. 65A (1978) 351.

[52] T. Ogawa, Y. Urata, S. Wada, K. Onodera, H. Machida, H. Sagae, M. Higuchi and K. Kodaira, Opt. Lett. 28, (1994) 2333

[53] W. Liu et al., Phys. Rev. Lett., 82 (1999), 711

[54] V. W. Hughes, C. S. Wu, "Muon Physics volume III", Academic press, New York (1975).

[55] T. M. Kojima, D. Tomono et al., JPSJ 76, 093501 (2007)

[56] Y. Yamazaki ed., "Accelerator Technical DesignReport for J-PARC", KEK-Report2002-13.

[57] T. Kageyama, et. al., "Development of Annular Coupled Structure", Procs. of LINAC'94, Tsukuba, 1994, p. 248 (1994).

[58] K. R. Crandall et. al.,"RFQ design codes", LA-UR-96-1836.

[59] T. Kato, "Proposal of a separated-type proton drift tube linac for a medium-energy structure", KEK Report 92-10 (1992).

[60] K. R. Crandall, D. P. Rusthoi, "TRACE-3D Documentation", Los Alamos National Laboratory Report, LA-UR-97-886, 1997.

[61] J. Qiang, R. D. Ryne, S. Habib, V. Decyk, J. Comput. Phys. 163, p. 434 (2000).

[62] Masao Nakamura, Japan Journal of Applied Physics, Vol.7, No.3, March, 1968.

[63] E. J. Konopinski,Annu. Rev. Nucl. Sci. 1959.9: 99-158.

[64] F. Combley and E. Picasso, Physics Report (Section C of Physics Letters)